DISS. ETH No. 26839

# Linear Feedback Cooling of a Levitated Nanoparticle in Free Space

A thesis submitted to attain the degree of

Doctor of Sciences of ETH Zurich

(Dr. sc. ETH Zurich)

presented by

Felix Tebbenjohanns

MSc EEIT, ETH Zurich

born on 19.06.1991

citizen of Germany

accepted on the recommendation of

Prof. Dr. Lukas Novotny, examiner

Prof. Dr. Yiwen Chu, co-examiner

Dr. Nikolai Kiesel, co-examiner

2020

# Abstract

About a decade ago, optically levitated nanoparticles have been proposed for macroscopic tests of quantum mechanics. For such tests, the thermal motion of the particle's center of mass is required to be close to its ground state of energy. Ever since these proposals, research groups around the world try to achieve ground-state cooling of optically levitated glass particles.

In this dissertation, we cool the center-of-mass motion of a nanoparticle in an optical trap. Based on the position measurement of the particle, we apply a damping force in proportion to the particle's speed, which leads to a cooling effect. We find that the cooling performance of our cold damping scheme is limited by the measurement imprecision. We analyze our detection principle theoretically and find an ideal detection scheme whose imprecision is at the fundamental noise level dictated by quantum mechanics. Such a Heisenberg-limited detection would, in principle, allow for ground-state feedback cooling. With these insights applied to our experiment, we cool the motion of our particle to an average of four quanta. Moreover, we resolve an asymmetry between the Stokes and anti-Stokes scattered light from the particle. This quantum effect allows us to calibrate the system to the ground state energy.

Our work advances the research field of levitated optomechanics toward quantum control and therefore toward macroscopic tests of quantum mechanics.

# Zusammenfassung

Vor rund zehn Jahren wurde vorgeschlagen, die Gesetze der Quantenmechanik an makroskopischen Objekten mittels in Laserstrahlen schwebenden Nanopartikeln zu testen. Seitdem versuchen Forschungsgruppen weltweit, die thermische Partikelbewegung von solch schwebenden Glaspartikeln bis nah an ihren Quantengrundzustand zu kühlen.

In dieser Dissertation kühlen wir die Schwerpunktsbewegung eines Nanopartikels in seiner optischen Falle. Basierend auf einer Positionsmessung legen wir eine dämpfende Kraft in Proportion zur Partikelgeschwindigkeit an, was zu einer Kühlung der Bewegung führt. Wir beobachten, dass diese Kühltechnik durch unsere Messungenauigkeit limitiert ist. Wir untersuchen unsere optische Detektion theoretisch und finden ein ideales Messverfahren, dessen Ungenauigkeit durch die fundamentalen Nullpunktfluktuationen der Quantenphysik gegeben ist. Solch eine Heisenberg-limitierte Messung würde es uns prinzipiell ermöglichen, das Partikel in seinen Grundzustand zu kühlen. Mit dieser Einsicht angewandt auf unser Experiment kühlen wir die Partikelbewegung zu vier Energiequanten. Damit können wir die sogenannte Seitenbandasymmetrie zwischen Stokes und Anti-Stokes Streuung auflösen. Dieser Quanteneffekt ermöglicht es uns, das System gegen die Grundzustandsenergie zu kalibrieren.

Unsere Arbeit bringt das Forschungsfeld der schwebenden Optomechanik einen Schritt näher in Richtung makroskopischer Tests der Quantentheorie.

# Foreword

The work in this dissertation results from a great team effort. Here, I summarize the contributions, which I received from other people. The original experimental setup was built by Vijay Jain. I adapted the vacuum chamber, the laser system, and the electronic data-acquisition system for this work. Vijay also suggested to measure the sideband asymmetry and conducted initial experiments in this direction. Martin Frimmer originally suggested to use the Coulomb force acting on the particle's charge to apply a linear feedback. I had the invaluable chance to discuss every essential step in this dissertation with Martin, he phrased large parts of the papers that we wrote together, and he drew Figs. 3.1, 3.2, 3.3, 4.1, and D.1. Andrei Militaru suggested to use the specific type of filter in chapter 2 and looked over all the theoretical work. The calculations and discussion in Appendix B have been proposed and initiated by Jan Gieseler. Dominik Windey recommended the strategy we used to align the backscattering detector. He also installed and configured the frequency generators for our heterodyne detection scheme in chapter 4. René Reimann has been another invaluable discussion partner, without whose experimental tips and tricks, this work would not have been possible. The continuous discussion with my supervisor Lukas Novotny and my colleagues Patrick Back, Eric Bonvin, Rozenn Diehl, Erik Hebestreit, Fons van der Laan, Maria Luisa Mattana, and Alfonso Nardi generated a framework that made this work possible.

This research was supported by ERC-QMES (Grant No. 338763), the NCCR-QSIT program (Grant No. 51NF40-160591), and SNF (Grant No. 200021L-169319/1).

# Contents

# 1

# Introduction

The interaction of light and matter is at the heart of a host of precision measurements, ranging from the detection of gravitational waves to the definition of the international unit system [1, 2]. What makes light fields our probe of choice is the availability of detectors and laser sources that operate at the fundamental noise limit dictated by the laws of quantum mechanics. Recognizing the potential of the laser to investigate fundamental physical processes, the scientific community started to explore the possibilities of mechanical manipulation of matter using the forces of light in optical traps [3–6]. These forces, more specifically their fluctuations, can be interpreted as the inevitable consequence of the measurement process resulting from light-matter interaction [7]. Thus, optical forces and measurement precision are linked according to the Heisenberg uncertainty principle. The investigation of these measurement backaction effects has generated the field of optomechanics, which has developed experimental platforms that allow both measurement and control of mechanical motion at the quantum limit using light fields [8–12].

One of the many optomechanical systems are dielectric particles levitated in optical traps [13–20]. These levitated systems complement traditional

mechanically tethered structures, in applications ranging from precision measurements [21–24] to the investigation and control of quantum states of massive objects [25]. For both levitated and mechanically clamped oscillators, investigation of unexplored physics, such as the experimental testing of collapse models [26], requires cooling the oscillator's motion to its quantum ground state as a prerequisite. This feat has been achieved for cryogenically precooled mechanically clamped systems using autonomous cavity cooling [27–29]. Cavity cooling is also a promising cooling technique for levitated systems [30–35]. With the recent first report on cavity-based ground-state cooling [36], the field is on the brink of developing quantum control over the optically levitated particle.

In parallel to cavity-based cooling techniques, the field of levitated optomechanics has experienced a fast development of active-feedback cooling. Here, the levitated particle's position is measured in real time and fed back to the system using an electronic filter. The filter is tuned such that energy is removed from the motion, leading to a cooling effect. Two versions of these so-called cold-damping techniques exist, namely linear feedback [15, 37, 38] and parametric feedback [18, 39, 40]. The forerunner in cooling the optical levitated particle's oscillation was in a single-beam optical trap and relied on parametric feedback [41]. In this thesis, we analyze both theoretically and experimentally the alternative, linear feedback cooling.

Our particle is a sub-wavelength sized dielectric sphere of fused silica in close vicinity to the tight focus of a laser beam. In addition to gravity, the particle is subject to both a *gradient force* pointing to the laser focus and a *scattering force* pointing along the beam [42]. For a sufficiently strong focus, the gradient force overcomes both the scattering force and the gravitational force such that the particle can be stably trapped. The particle oscillates around the equilibrium trap position in a harmonic motion along all three spatial directions. For sufficiently small oscillation amplitudes, the three motions are independent of each other and are nondegenerate in frequency. Details on this can be found in PhD theses [43–45] and especially [46], which refers the exact setup upon which this thesis is based.

This thesis is structured as follows. After this introduction, in chapter 2, we focus on linear feedback cooling the motion along one spatial direction. Our

feedback method applies a damping force in proportion to the particle's speed. We find a model for the motional energy under feedback in agreement with the measured data. We show that for an optimal set of feedback parameters, the cooling is more efficient than what has been shown with parametric feedback.

Moreover, we understand that the minimal energy is given by the *imprecision-backaction product*. This quantity can be understood as the product of the position measurement error $\delta x$ and the momentum fluctuations $\delta p$ exerted on the particle by the environment. Heisenberg's uncertainty relation imposes a lower bound for this product with $\delta x \delta p \geq \hbar/2$, where $\hbar$ is the reduced Planck constant. This relation is satisfied with equality if both $\delta x$ and $\delta p$ are only due to laser fluctuations at the fundamental quantum level. However, at this stage of our experiment, neither $\delta x$ nor $\delta p$ are at their fundamental limit, and in fact the product $\delta x \delta p$ is a factor of 30 above the optimum.

In chapter 3 we analyze the theoretical limitations of the detection imprecision $\delta x$. We find that in a backscattering setup it can be reduced to within a factor of two from the fundamental limit. Combined with an ultra-high vacuum, which minimizes $\delta p$, and the feedback described before, this would allow for ground-state cooling.

With this insight applied to our experiment, we observe a feedback-cooled oscillation energy of about four quanta in chapter 4, which puts ground-state cooling firmly within reach experimentally. Furthermore, we observe the *sideband asymmetry* between Stokes- and anti-Stokes scattering associated with the particle's oscillation, an effect which is understood as a consequence of the existence of the ground state of motion. Of more practical relevance for future experiments, this effect allows us to calibrate the motional energy against a quantum of energy $\hbar\Omega$, where $\Omega$ is the particle's oscillation frequency.

In chapter 5 we present a framework to describe our cavity-free system theoretically as complementary to the standard (cavity-)optomechanics framework. Finally in chapter 6, the conclusion, we summarize the thesis and give an outlook toward creating macroscopic superposition states with an optically trapped nanoparticle.

This introduction is partly based on the article F. Tebbenjohanns, M. Frimmer, A. Militaru, V. Jain, and L. Novotny, Phys. Rev. Lett. **122**, 223601 (2019).

# 2

# Linear feedback cooling

This chapter is based on the article F. Tebbenjohanns, M. Frimmer, A. Militaru, V. Jain, and L. Novotny, Phys. Rev. Lett. **122**, 223601 (2019).

*We implement a cold-damping scheme to cool one mode of the center-of-mass motion of an optically levitated nanoparticle in ultrahigh vacuum ($10^{-8}$ mbar) from room temperature to a record-low temperature of* $100\,\mu$K. *The measured temperature dependence on the feedback gain and thermal decoherence rate is in agreement with a parameter-free model. For the first time, we determine the imprecision-backaction product for a levitated optomechanical system and discuss the resulting implications for ground-state cooling of an optically levitated nanoparticle.*

## 2.1 Introduction

In this chapter we implement an active feedback cooling technique to cool one mode of the particle's center-of-mass motion with the ultimate goal of transferring it into the quantum regime, where the motional energy is comparable to the ground-state energy. Despite the remarkable development of cavity-based

cooling techniques [30–32, 34], the most successful cooling method in levitated optomechanics to date has been *cold damping* using parametric feedback in a single-beam optical dipole trap [18, 39]. In this measurement-based cooling technique, the measured position record is frequency doubled and fed back to the trap beam. This endeavor has led to mean occupation numbers of the center-of-mass motion below a hundred phonons [41]. In contrast, in the realm of mechanically tethered oscillators and trapped ions, a different active feedback cooling method has been developed [47–51]. This linear feedback technique applies a direct force to the oscillator in proportion to its speed, effectively leading to an increased damping rate [52]. Cold damping based on linear feedback has recently been used to bring a cryogenically precooled, cavity-coupled membrane to its quantum ground state of motion [29]. Given the success of linear feedback in the context of cooling mechanically tethered oscillators, it is a tantalizing prospect to adapt the technique to optically levitated nanoparticles in single-beam dipole traps.

In this chapter we cool the center-of-mass motion of an optically levitated nanoparticle along one axis to a temperature of $100\,\mu\mathrm{K}$ using linear feedback. To this end, we exploit the Coulomb force acting on the net electric charge carried by the particle [37, 53, 54]. We investigate the cooling performance as a function of gas pressure and feedback gain to explore the limitations of the method. Our system operates a factor of one thousand from the Heisenberg limit of the imprecision-backaction product and provides a platform for studying ground-state cooling of optically levitated oscillators.

## 2.2 Experimental setup

Our experimental setup is shown in Fig. 2.1. We optically trap a silica nanoparticle (diameter 136 nm) in a linearly polarized laser beam (wavelength 1064 nm, focal power 130 mW), focused by a microscope objective ($0.85\,\mathrm{NA}$) to a diffraction-limited spot. The resulting oscillation frequencies of the particle's center of mass are $\Omega_z = 2\pi \times 45$ kHz, $\Omega_x = 2\pi \times 125$ kHz, and $\Omega_y = 2\pi \times 146$ kHz, where $z$ denotes the direction along the optical axis, while $x$ ($y$) is the coordinate in the focal plane along (orthogonal to) the axis of polarization. We collect the forward scattered light with a lens and guide it to a standard

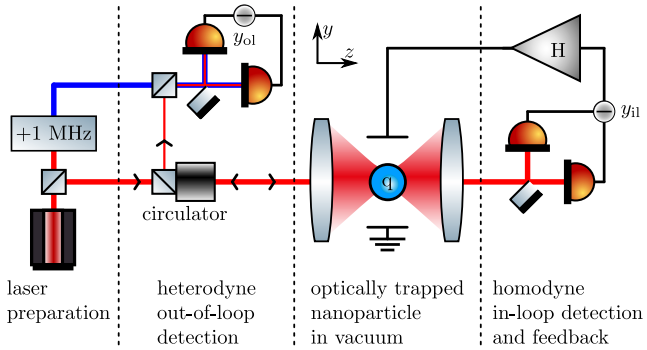


**Figure 2.1:** A silica nanoparticle (nominal diameter 136 nm) carrying a finite net charge $q$ is optically trapped in vacuum using a laser beam (wavelength 1064 nm) focused by an objective. To measure the $y$ motion of the particle, the backscattered light is rerouted by a free-space circulator and mixed with a local oscillator (frequency shifted by 1 MHz relative to the trap laser) to a balanced split detection scheme, yielding the out-of-loop signal $y_{\mathrm{ol}}$. The forward scattered light is detected in another balanced split detection scheme and yields the in-loop signal $y_{\mathrm{il}}$, which is processed by a linear, digital filter $H$. The resulting feedback signal is applied as a voltage to a capacitor enclosing the trapped particle.

homodyne detection system for the particle's motion along all three axes, which we call the in-loop detector (only shown for the $y$ axis in Fig. 2.1) [18]. Throughout this chapter, the particle's motion along the $x$ and $z$ directions is cooled using parametric feedback to temperatures below 1 K, rendering non-linearities of the trapping potential irrelevant [41, 55]. From here on, we solely focus on the motion of the particle along the $y$ axis. We exert a Coulomb force on the net charge carried by the optically trapped nanoparticle by applying a voltage to a pair of electrodes enclosing the trap [53]. To cool the particle's motion, this voltage is a feedback signal derived from the measurement signal $y_{\mathrm{il}}$ acquired from the forward scattered light. Our linear feedback filter with transfer function $H(\Omega)$ consists of a series of digital, second-order biquad filters, which essentially mimics a derivative filter, such that the feedback signal is proportional to the particle's velocity. More specifically, we use a band-pass filter whose center-frequency is set to above the particle's oscillation frequency $\Omega_y$, such that the transfer function at $\Omega_y$ increases linearly with frequency while preserving a flat phase response [29]. Note that after performing these

experiments, we found out that a simple time-delay of the signal in combination with two notch filters suffices for feedback cooling. For more details see App. C. Finally, we measure the out-of-loop signal $y_{\mathrm{ol}}$ with a heterodyne detection system for the backscattered light, using a local oscillator which is frequency shifted by $1\,\mathrm{MHz}$ from the trapping light. We calibrate our detectors in the mildly underdamped regime at a pressure of $10\,\mathrm{mbar}$ using the equipartition theorem in the absence of feedback cooling [56]. All data presented in this chapter has been taken with the same particle.

## 2.3 Cooling performance

We now investigate the performance of our feedback cooling scheme at a pressure of $1.4 \times 10^{-8}\,\mathrm{mbar}$. In Fig. 2.2(a) we show the single-sided power spectral density (PSD) $\tilde{S}_{yy}^{\mathrm{ol}}$ of the out-of-loop signal for different feedback

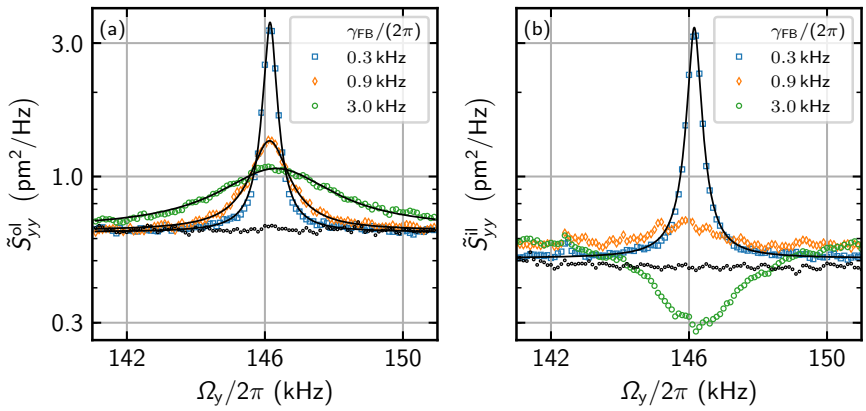


**Figure 2.2:** (a) Single-sided power spectral densities $\tilde{S}_{yy}^{\mathrm{ol}}$ of the motion of the nanoparticle measured by the out-of-loop detector for different feedback damping rates $\gamma_{\mathrm{FB}}$. The solid lines are Lorentzian fits to the data. The black datapoints denote the measured shot-noise level $\tilde{S}_{\mathrm{imp}}^{\mathrm{ol}}$ on the out-of-loop detector. (b) Power spectral densities $\tilde{S}_{yy}^{\mathrm{il}}$ measured by the in-loop detector for the same settings as in (a). Photon shot-noise $\tilde{S}_{\mathrm{imp}}^{\mathrm{il}}$ is shown as black datapoints. In contrast to (a), for large feedback gain ($\gamma_{\mathrm{FB}} = 2\pi \times 3.0\,\mathrm{kHz}$) we observe noise squashing, *i.e.*, the measured signal drops below the noise floor.

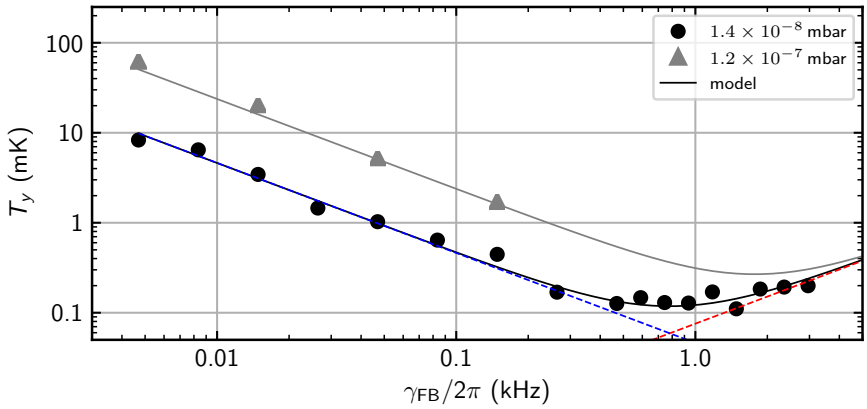


**Figure 2.3:** Mode temperature $T_y$ derived from the out-of-loop signal $y_{ol}$ as a function of feedback gain $\gamma_{FB}$. The black circles denote the measured values at a pressure of $1.4 \times 10^{-8}$ mbar. At a damping rate of $\gamma_{FB} = 2\pi \times 1$ kHz, we observe a minimum temperature of 100 µK. The solid black line is a parameter-free calculation according to Eq. (2.3). The blue (red) dashed line denotes the contribution of the first (second) term in Eq. (2.3). The grey triangles and line show measured and calculated mode temperatures at a higher pressure of $1.2 \times 10^{-7}$ mbar.

gains, which we express as damping rates $\gamma_{FB}$. We extract the damping rate $\gamma_{FB}$ from ring-down measurements as detailed further below. The measured signal $\tilde{S}_{yy}^{ol}$ corresponds to a Lorentzian function added to a spectrally flat noise floor due to the photon shot noise on our detector. The spectral width of the Lorentzian is a measure for the total damping rate arising from feedback cooling and residual gas damping. The latter is largely negligible under feedback at the low gas pressures of our experiments. As expected, as we increase the feedback gain, the Lorentzian broadens in width due to the induced feedback damping. The area under the Lorentzian, on the other hand, is a measure for the energy (*i.e.*, temperature) of the particle's oscillation mode. Thus, from the PSD of the out-of-loop signal $\tilde{S}_{yy}^{ol}$, we extract the energy $k_B T_y$ in the $y$ mode of the levitated particle. For comparison, we show the PSD of the measured in-loop signal $\tilde{S}_{yy}^{il}$ in Fig. 2.2(b) at the same gain values as in Fig. 2.2(a). For large feedback gain, we observe that $\tilde{S}_{yy}^{il}$ drops below the shot noise level. This effect, termed *noise squashing*, arises from correlations between the particle's position

and the measurement noise that is fed back by the control loop [48, 49].

In Fig. 2.3, we plot the measured mode temperature $T_y$ as a function of feedback damping rate $\gamma_{\mathrm{FB}}$ at a pressure of $1.4 \times 10^{-8}\,\mathrm{mbar}$ as black circles. At small feedback gains, we observe a decrease in oscillator temperature with increasing feedback gain. However, there exists an optimal feedback gain of about $1\,\mathrm{kHz}$. For gain values larger than the optimum, the oscillator temperature increases with increasing feedback gain. We additionally show measurements performed at a higher pressure of $1.2 \times 10^{-7}\,\mathrm{mbar}$ (grey triangles), where the increased gas damping rate leads to a larger mode temperature as compared to the low-pressure data.

## 2.4 Analysis

To understand our results, let us analyze our system from a theoretical perspective [48, 57]. The Fourier transform $\hat{y}(\Omega)$ of the time-dependent particle position $y(t)$ follows the equation of motion*

$$\left[\Omega_y^2 - \Omega^2 - \mathrm{i}\gamma\Omega - H(\Omega)\right]\hat{y} = \frac{\hat{f}_{\mathrm{fluct}}}{m} + H(\Omega)\hat{y}_{\mathrm{imp}}, \tag{2.1}$$

where $\Omega_y$ is the $y$ mode's eigenfrequency, $m$ the particle's mass, and $\hat{y}_{\mathrm{imp}}$ is the measurement shot noise on the in-loop detector, which measures $\hat{y}_{\mathrm{il}} = \hat{y} + \hat{y}_{\mathrm{imp}}$. The damping rate $\gamma$ arises from the interaction with residual gas molecules. The term $\hat{f}_{\mathrm{fluct}}$ describes the fluctuating force generated by the interaction with the gas and from radiation pressure shot noise. Via the fluctuation dissipation theorem, $\hat{f}_{\mathrm{fluct}}$ is inextricably linked to $\gamma$ [59]. Within the bandwidth of interest, the transfer function of our feedback circuit is well described by a derivative filter $H(\Omega) = \mathrm{i}\gamma_{\mathrm{FB}}\Omega$. The feedback damping rate $\gamma_{\mathrm{FB}}$ can be set by adjusting the feedback gain and incorporates the exact geometry of the capacitor electrodes as well as the number of charges carried by the levitated particle. Importantly, the feedback transfer function $H(\Omega)$ appears twice in Eq. (2.1), which results from the fact that the input to the feedback circuit $\hat{y}_{\mathrm{il}}$ is the sum of the true position $\hat{y}$ and the measurement shot noise $\hat{y}_{\mathrm{imp}}$. From Eq. (2.1), we

*Note, that in order to use a consistent definition of the Fourier transform within this thesis, the sign of $\Omega$ is flipped compared to our publication [58].

obtain the two-sided PSD on the out-of-loop detector

$$S_{yy}^{\mathrm{ol}}(\Omega) = \frac{S_{ff}/m^2 + \gamma_{\mathrm{FB}}^2 \Omega^2 S_{\mathrm{imp}}^{\mathrm{il}}}{\left(\Omega_y^2 - \Omega^2\right)^2 + \left(\gamma + \gamma_{\mathrm{FB}}\right)^2 \Omega^2} + S_{\mathrm{imp}}^{\mathrm{ol}}, \tag{2.2}$$

where $S_{ff}$ denotes the PSD of the fluctuating force $\hat{f}_{\mathrm{fluct}}$, and $S_{\mathrm{imp}}^{\mathrm{il}}$ ($S_{\mathrm{imp}}^{\mathrm{ol}}$) are the PSDs of the in-loop (out-of-loop) detector noise. Integrating the first term of Eq. (2.2), which corresponds to the PSD of the true position $y$, in the limit $\gamma_{\mathrm{FB}} \gg \gamma$ yields the variance*

$$\left\langle y^2 \right\rangle = \frac{\pi S_{ff}}{m^2 \gamma_{FB} \Omega_y^2} + \pi \gamma_{FB} S_{\mathrm{imp}}^{\mathrm{il}}, \tag{2.3}$$

which is a direct measure for the temperature $T_y = m\Omega_y^2 \left\langle y^2 \right\rangle / k_B$ of the oscillator mode†. The first term contributing to the expression in Eq. (2.3) scales with the inverse of the feedback cooling rate $\gamma_{\mathrm{FB}}$. This term resembles the desired action of the feedback, which is to reduce the impact of the heating term given by the fluctuating force $S_{ff}$. Importantly, the second term is proportional to the feedback damping rate, which multiplies with the measurement noise $S_{\mathrm{imp}}^{\mathrm{il}}$. This term resembles the undesired but inevitable effect of the control loop heating the particle by feeding back measurement noise. Accordingly, our model predicts the existence of an optimum feedback cooling rate, where the mode temperature reaches its minimum value $T_{\mathrm{min}} = 2\pi\Omega_y \sqrt{S_{ff} S_{\mathrm{imp}}^{\mathrm{il}}}/k_B$, a behavior that we observe in our measurements in Fig. 2.3.

For a quantitative comparison of measurement and theory, we have to determine all parameters entering Eq. (2.3). We extract the in-loop measurement noise $S_{\mathrm{imp}}^{\mathrm{il}}$ from the PSD shown in Fig. 2.2(b). To obtain the feedback damping rate $\gamma_{\mathrm{FB}}$, we perform ring-down measurements. To this end, we toggle the feedback gain back and forth between $\gamma_{\mathrm{FB}}$ for 30 µs and a much lower feedback gain $\gamma_{\mathrm{FB}}^{\mathrm{low}} = \gamma_{\mathrm{FB}}/300$ for 50 µs. As shown in Fig. 2.4, we measure the mode

*For a formal integration of the Lorentzian function in Eq. (2.2), see App. A.5.

†Here, we assumed the equipartition theorem, according to which the kinetic and potential energy are equal on average. Although in general this is not true under feedback [29, 60, 61], in our case it holds because the feedback damping rate $\gamma_{\mathrm{FB}}$ is much smaller than eigenfrequency $\Omega_y$. We analyze this effect, which we were not aware of at the time of publishing this work, in App. B.

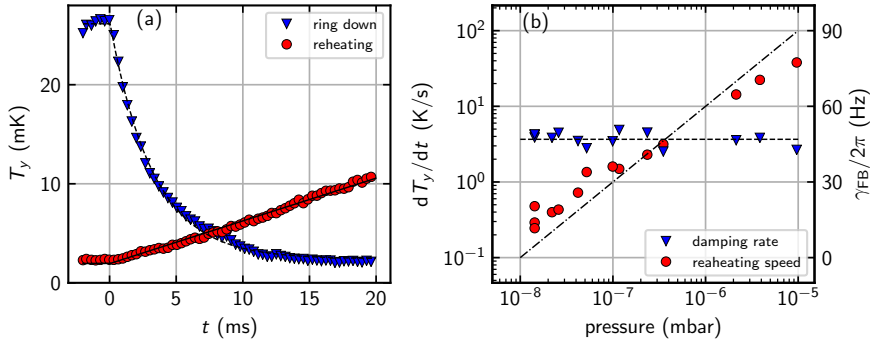


**Figure 2.4:** (a) Ring-down and reheating experiment. For the ring-down experiment, we start with the oscillation mode at an elevated temperature, reached by reducing the feedback gain. At time $t = 0$, we switch the feedback damping rate to $\gamma_{\mathrm{FB}}$ and measure the decay of the mode temperature $T_y(t)$ (blue triangles). We fit $T_y$ with a single exponential decay (black dashed line) and extract the decay constant, which yields $\gamma_{\mathrm{FB}} = 2\pi \times 47$ Hz. For the reheating experiment, we turn off the feedback-cooling at time $t = 0$ and measure the increasing mode temperature $T_y(t)$ (red circles). A linear fit (dash-dotted line) to the data yields the reheating speed $\mathrm{d}T_y/\mathrm{d}t = \gamma T_{\mathrm{bath}}$. (b) Feedback damping rate $\gamma_{\mathrm{FB}}$ (blue triangles) and reheating speed $\mathrm{d}T_y/\mathrm{d}t$ (red circles) as a function of pressure. The feedback damping rate is independent of pressure and solely determined by the gain of the feedback circuit. Within our pressure range the reheating follows a linear trend (indicated as the dash-dotted line).

temperature as a function of time after the gain was switched from $\gamma_{\mathrm{FB}}^{\mathrm{low}}$ to $\gamma_{\mathrm{FB}}$ at time $t = 0$. The blue triangles in Fig. 2.4(a) are the ensemble average over 100 such decay curves. We observe an exponential decay of the temperature and extract its time constant, which equals $\gamma_{\mathrm{FB}}$. When the feedback gain is switched from $\gamma_{\mathrm{FB}}$ to $\gamma_{\mathrm{FB}}^{\mathrm{low}}$ at time $t = 0$, we observe the mode temperature increasing linearly in time [red circles in Fig 2.4(a), averaged over 100 reheating experiments]. Since the observed time is much shorter than the inverse damping rate $\gamma$, we expect the temperature to increase as $T(t) = \gamma T_{\mathrm{bath}}\, t$. Together with the fluctuation dissipation theorem $S_{ff} = m\gamma k_B T_{\mathrm{bath}}/\pi$, the measured slope of the reheating curve therefore provides us with a direct measurement of the first term in Eq. (2.3) [59]. Equipped with the experimentally determined values for $\gamma_{\mathrm{FB}}$, $S_{\mathrm{imp}}^{\mathrm{il}}$, and $S_{ff}$, we calculate the mode temperature as a function of feedback gain according to Eq. (2.3) and display it as the solid black line

in Fig. 2.3. The dashed lines show the two separate contributions from the bath (blue) and measurement noise (red) to Eq. (2.3). Our model describes our experimental findings very well. We stress that there is no free parameter or fit involved.

Finally, we investigate the reheating speed and the ring-down rate $\gamma_{\mathrm{FB}}$ as a function of pressure. The results are displayed in Fig. 2.4(b). We find that the ring-down rates (blue triangles) do not depend on pressure. This observation confirms that the damping rate under feedback is indeed fully dominated by and therefore equivalent to the feedback induced damping rate $\gamma_{\mathrm{FB}}$. The red circles in Fig. 2.4(b) show the measured reheating speeds $\mathrm{d}T_y/\mathrm{d}t$ as a function of pressure, which follow the expected linear behavior (dash-dotted line).

## 2.5 Discussion

Let us discuss the current limitations and future prospects of our linear feedback cooling approach for levitated optomechanics. To this end, we return to Eq. (2.3), whose two contributions are related by the imprecision-backaction product $(4\pi)^2 S_{ff} S_{\mathrm{imp}}^{\mathrm{il}} = \hbar^2/\eta$, with the measurement efficiency $\eta \leq 1$ [59]. Using $\bar{n} = k_B T_y/(\hbar\Omega_y) - 1/2$, we find that the effective occupation number $\bar{n}$ assumes a minimum at the optimal feedback gain, which solely depends on $\eta$ as $\bar{n}_{\mathrm{min}} = (1/\sqrt{\eta} - 1)/2$ [29]. At the Heisenberg limit of unit efficiency $\eta = 1$, when the fluctuating force $S_{ff}$ driving the system under investigation is purely due to measurement backaction, and the imprecision noise $S_{\mathrm{imp}}^{\mathrm{il}}$ is minimized by optimally detecting all photons scattered by the levitated particle, the particle's motion could, in principle, be brought to its quantum ground state $n_{\mathrm{min}} = 0$. In our case, at the lowest investigated pressure of $1.4 \times 10^{-8}\,\mathrm{mbar}$, we extract a total efficiency of $\eta = 9 \times 10^{-4}$ and hence an occupation number of about 16. Our measurements in Fig. 2.4(b) suggest that we can further reduce $S_{ff}$ by moving to even lower pressures, before entering the regime where reheating is fully dominated by photon recoil [41]. The factor $S_{\mathrm{imp}}^{\mathrm{il}}$ in our case is limited by the finite collection and detection efficiency. The latter is restricted by the non-ideal mode overlap between the scattered dipole field and the Gaussian trapping beam on the detector. In chapter 3 we analyze the theoretical detection efficiency of our split detection scheme and show that it is limited to about $0.1$

even in the absence of loss. We furthermore show that we can reach a much higher detection efficiency in a backscattering setup making cold damping to the ground state feasible.

## 2.6 Conclusion

In conclusion, we have demonstrated feedback induced damping of the center-of-mass motion of an optically levitated nanoparticle from room temperature to 100 µK, corresponding to less than 20 phonons. We have determined the optimal feedback-damping rate for our system, in agreement with a parameter-free model. Together with photonic techniques under development [34, 62], our results put ground-state cooling of optically levitated nanoparticles firmly within reach. Besides setting a new temperature benchmark, we believe that our feedback control scheme will serve as a model system for the levitated optomechanics community. Putting this work into context, our approach is complementary to parametric feedback cooling, the method of choice to control charge-neutral optically levitated particles to date. While our system relies on the levitated object carrying finite net charge, we note that one could use the radiation-pressure force of another laser beam to achieve the same feedback on charge-neutral particles [15]. While the linear feedback cooling scheme outperforms parametric feedback in cooling power, in practice the parametric scheme is simpler to set up since it only relies on an amplitude modulation of the trap beam. So far, we have not implemented 3D cooling with linear feedback but instead relied on the parametric feedback to stabilize the trap in all three axes. Importantly, this work provides the direct connection between established, mechanically tethered optomechanical technologies and optically levitated oscillators [29, 48, 49]. By mapping our optically levitated system onto the standard model of a cold-damped oscillator, for the first time, we have determined the imprecision-backaction product for a levitated optomechanical system. Accordingly, this work generates the opportunity to leverage the insights gained with mechanically clamped systems to drive levitated optomechanics forward.
During the time of publishing this work, we became aware of a partly overlapping work [63].

# 3

# Optimal position detection

This chapter is based on the article F. Tebbenjohanns, M. Frimmer, and L. Novotny, Phys. Rev. A **100**, 043821 (2019).

*We theoretically analyze the problem of detecting the position of a classical dipolar scatterer in a strongly focused optical field. We suggest an optimal measurement scheme and show that it resolves the scatterer's position in three dimensions at the Heisenberg limit of the imprecision-backaction product. We apply our formalism to levitated-optomechanics experiments and show that backscattering detection provides sufficient information to feedback cool the particle's motion along the optical axis to a phonon occupancy below unity under realistic experimental conditions.*

## 3.1 Introduction

In this chapter we analyze the position detection process of an optically levitated particle. Let us start by revisiting the detection process in clamped optomechanical platforms, where the position of high-quality mechanically tethered

oscillators is read out optically. The limits of this measurement process have been understood since the early theoretical works in the context of designing interferometer-based gravitational-wave detectors [7, 64, 65]. In the canonical optomechanical setup, the position of a mirror reflecting a beam of light is encoded into the field's phase and is read out interferometrically [66]. At the same time, the radiation-pressure fluctuations of the probe light influence the mechanical motion of the mirror. Accordingly, the measurement of the mirror's position inevitably entails a perturbation of its momentum [11, 67, 68]. In the limit of perfect detection efficiency, and in the absence of dephasing mechanisms besides radiation pressure shot noise, the product of the measurement imprecision and the measurement backaction satisfies the Heisenberg relation with equality [59] (see also Ch. 2). In recent years, harnessing enhancement effects provided by optical cavities, the optomechanics community has pushed the position detection of mechanically clamped oscillators to operate essentially at the Heisenberg limit [29].

In chapter 2 we showed cooling of the center-of-mass motion of an optically levitated nanoparticle to a population of a dozen phonons using active feedback cooling. The system operated three orders of magnitude from the Heisenberg limit of maximum measurement efficiency [58]. At this stage, pushing optically levitated systems into the quantum regime relies on improving the detection efficiency for the position of a dipolar scatterer in a focused light field [69, 70]. To this end, remarkable progress has been made in recent years to couple optically levitated nanoparticles to optical resonators [30–34], in efforts inspired by the atomic physics community [71–74]. Interestingly, while sophisticated detection systems using optical cavities are under development, the question of the reachable position-detection efficiency for a dipolar scatterer in a single-beam optical trap has remained unanswered.

In this chapter we theoretically analyze the problem of how to optimally measure the position of an isotropic dipolar scatterer in a focused light field. We derive a scheme to detect the motion of a nanoparticle optically trapped in a focused light field which operates strictly at the Heisenberg limit of optimal detection efficiency. Furthermore, we analyze the efficiencies of detection schemes currently employed by the optical-levitation community. Our results show that a simple backscattering configuration provides a detection

efficiency for the oscillation mode along the optical axis of more than 60% of the Heisenberg limit. Accordingly, active feedback cooling of a levitated nanoparticle's center-of-mass motion to a phonon occupancy below unity is feasible in a single-beam optical trap.

## 3.2 Ideal measurement scheme

We consider a laser beam, linearly polarized along the $x$ direction and propagating along the optical $z$ axis, which is strongly focused, as shown in Fig. 3.1. The focus defines the origin of the coordinate system. We furthermore assume an isotropic dipolar scatterer with polarizability $\alpha$ located at position $\mathbf{r}_0 = (x_0, y_0, z_0)$. The distance $|\mathbf{r}_0|$ of the scatterer to the focus is much less than a wavelength. At the scatterer position, the electric field reads

$$\mathbf{E}_{\text{foc}}(\mathbf{r}_0) = E_0 \mathbf{n}_x \exp(\mathrm{i}Akz_0), \tag{3.1}$$

which resembles a plane wave traveling in the positive $z$ direction (see Appendix D.1 for a derivation of the focal field). Here, $\mathbf{n}_x$ is the unit vector along $x$, $E_0$ is the field amplitude at the focus, and $k$ is the wavenumber. The

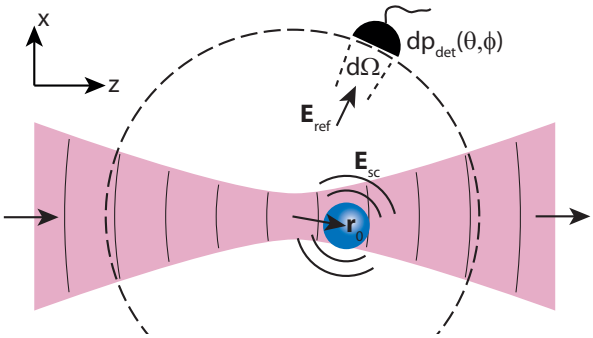


**Figure 3.1:** Sketch of the ideal measurement scheme. An isotropic dipolar scatterer is located at position $\mathbf{r}_0$ relative to the origin, which coincides with the focal point of a beam of light traveling from left to right. An array of detectors (only one is depicted for clarity, each covering a solid angle $\mathrm{d}\Omega$) is covering a sphere centered on the origin with radius much larger than the wavelength. A reference field $\mathbf{E}_{\text{ref}}$ is added at the detector for homodyne detection of the scattered field $\mathbf{E}_{\text{sc}}$.

geometric factor $0.64 < A \leq 1$ is a result of the Gouy phase shift in a focused beam and increases the effective wavelength close to the focus. We derive an analytical expression for $A$ in a strongly focused field in Appendix D.1. In a mildly focused field, described as a Gaussian beam with Rayleigh range $z_R$, we find $A = 1 - (kz_R)^{-1}$ [42, 70].

The dipolar scatterer acquires the dipole moment $\mathbf{p} = \alpha \mathbf{E}_{\text{foc}}(\mathbf{r}_0)$, and radiates the scattered field $\mathbf{E}_{\text{sc}}(\mathbf{r})$. At an observation point $\mathbf{r}$ much farther from the scatterer than a wavelength, we can write the scattered field in the Fraunhofer approximation as [42]

$$\mathbf{E}_{\text{sc}}(\mathbf{r}) = \mathbf{E}_{\text{dip}}(\mathbf{r}) \exp\left[-\mathrm{i}k \cdot (\mathbf{r_0} \cdot \mathbf{n}_r - Az_0)\right], \tag{3.2}$$

where $\mathbf{n}_r$ is the unit vector in the radial direction and $\mathbf{E}_{\text{dip}}(\mathbf{r})$ is the far field generated at the observation point $\mathbf{r}$ by an $x$ oriented dipole located at the origin. Importantly, the scatterer's position $\mathbf{r}_0$ is contained in the phase of the scattered field, which consists of two terms. The first term $-k\mathbf{r}_0 \cdot \mathbf{n}_r$ describes the phase generated by the displacement of the dipole relative to the origin. The second term $Akz_0$ stems from the fact that the dipole is driven by a traveling wave which acquires a phase shift during propagation. In the following, we use a spherical coordinate system, where the angle $\theta$ denotes the polar angle relative to the $z$ axis, and $\phi$ denotes the azimuthal angle relative to $x$. Furthermore, we introduce the differential power $\mathrm{d}p_{\text{dip}}$ scattered by an $x$ polarized dipole into the solid angle $\mathrm{d}\Omega = \sin(\theta)\mathrm{d}\theta\mathrm{d}\phi$:

$$\mathrm{d}p_{\text{dip}} = \frac{3}{8\pi} P_{\text{dip}} \left[1 - \sin(\theta)^2 \cos(\phi)^2\right] \, \mathrm{d}\Omega, \tag{3.3}$$

with the total scattered power $P_{\text{dip}}$.

### 3.2.1 Measurement backaction

In this subsection we analyze the measurement backaction arising from the interaction of the scatterer with the electromagnetic field. This backaction takes the form of a recoil force, which can be interpreted as an inevitable consequence of the fact that the scattered field contains information about the scatterer's position. The measurement-backaction force along a certain direction $(x, y, z)$

can be quantified by its power spectral density. Along the transverse directions $x$ and $y$, the spectral densities of this measurement backaction read [41, 75]

$$S_{\mathrm{ba}}^{x} = \frac{1}{5}\frac{\hbar k}{2\pi c}P_{\mathrm{dip}}, \tag{3.4a}$$

$$S_{\mathrm{ba}}^{y} = \frac{2}{5}\frac{\hbar k}{2\pi c}P_{\mathrm{dip}}. \tag{3.4b}$$

Note that along the $x$ and $y$ axes the result for the measurement backaction for a (passive) dipole scattering a power $P_{\mathrm{dip}}$ equals the result for an active dipolar source radiating the same power. In contrast to an active source, however, the fluctuating force acting on a scatterer along the $z$ axis has two contributions. First, there is the contribution that equals $S_{\mathrm{ba}}^{y}$, which arises both for a passive scatterer and an active dipolar source. However, for a passive scatterer, a second term arises, which stems from the fluctuations of the radiation pressure along the propagation direction of the beam. In close vicinity of the focus, for a lossless dipolar scatterer, this radiation pressure force reads $F_{\mathrm{rp}}^{z} = AP_{\mathrm{dip}}/c$ [42]. Summing both contributions, we find the total measurement backaction along the $z$ axis

$$S_{\mathrm{ba}}^{z} = \left(\frac{2}{5} + A^{2}\right)\frac{\hbar k}{2\pi c}P_{\mathrm{dip}}. \tag{3.4c}$$

We provide a derivation of Eqs. (3.4) in Appendix D.2 and note that our results agree with a full quantum calculation [76].

### 3.2.2 Measurement imprecision

Having dealt with the measurement backaction, we now turn to the measurement imprecision associated with locating a point scatterer in a focused light field. Since the scatterer's position $\mathbf{r}_0$ is encoded solely in the phase of the scattered light according to Eq. (3.2), we make use of a homodyne measurement, where we superpose the scattered light at the detector position $\mathbf{r}$ with a strong local oscillator field. Note that we do *not* use the trapping field as a reference field here (as is done in typical experimental schemes discussed in Sec. 3.3), which is always possible by introducing a sufficiently strong additional reference. For

optimal interference, we choose the (local) polarization of the reference to equal that of the scattered light. Thus, we construct an *ideal* reference field

$$\mathbf{E}_{\text{ref}}(\mathbf{r}) = -\mathrm{i}\gamma\mathbf{E}_{\text{dip}}(\mathbf{r}) \tag{3.5}$$

with $\gamma \gg 1$ (such that the reference field is much stronger than the scattered field) and let it interfere with the dipole's scattered light such that the field at position $\mathbf{r}$ is $\mathbf{E}_{\text{ref}}(\mathbf{r}) + \mathbf{E}_{\text{sc}}(\mathbf{r})$. For small displacements $\mathbf{r}_0$, a detector positioned at $\mathbf{r}$ covering the differential solid angle $\mathrm{d}\Omega$ measures the power

$$\mathrm{d}p_{\text{det}}(\theta,\phi) = \left[\gamma^2 + 2\gamma k\left(\mathbf{r}_0 \cdot \mathbf{n}_r - Az_0\right)\right]\ \mathrm{d}p_{\text{dip}}, \tag{3.6}$$

where we have retained only the term linear in the scattered field (which is much weaker than the reference field) and assumed $|k\mathbf{r}_0| \ll 1$. The first term of Eq. (3.6) accounts for the power of the reference and the second term accounts for the interference between reference and scattered fields. Being linear in $\mathbf{r}_0$, the interference term represents a measure of position. Assuming shot noise as the dominating noise source, the power spectral density of the imprecision noise associated with a differential detector under direction $(\theta,\phi)$ is (see Appendix D.3 for detailed derivation)

$$s^x_{\text{imp}}(\theta,\phi) = \frac{\hbar c}{8\pi k\sin(\theta)^2\cos(\phi)^2\ \mathrm{d}p_{\text{dip}}}, \tag{3.7a}$$

$$s^y_{\text{imp}}(\theta,\phi) = \frac{\hbar c}{8\pi k\sin(\theta)^2\sin(\phi)^2\ \mathrm{d}p_{\text{dip}}}, \tag{3.7b}$$

$$s^z_{\text{imp}}(\theta,\phi) = \frac{\hbar c}{8\pi k[\cos(\theta) - A]^2\ \mathrm{d}p_{\text{dip}}}. \tag{3.7c}$$

Next, we fill up the entire sphere surrounding the scatterer with differential detectors. Importantly, Eqs. (3.7) show that the measurement imprecision depends on the position $(\theta,\phi)$ of the differential detector and is not uniformly distributed. Accordingly, to minimize the total imprecision, we need to weight each measurement by its inverse imprecision before averaging [77]. To obtain the total imprecision, we exploit the fact that its inverse $1/S_{\text{imp}}$ is given by the integral over the inverse imprecisions $1/[s_{\text{imp}}(\theta,\phi)]$ contributed by the differential detectors, such that we find (the calculation is detailed in

Appendix D.3)

$$S^x_{\text{imp}} = 5\frac{\hbar c}{8\pi k}\frac{1}{P_{\text{dip}}}, \tag{3.8a}$$

$$S^y_{\text{imp}} = \frac{5}{2}\frac{\hbar c}{8\pi k}\frac{1}{P_{\text{dip}}}, \tag{3.8b}$$

$$S^z_{\text{imp}} = \frac{1}{\frac{2}{5}+A^2}\frac{\hbar c}{8\pi k}\frac{1}{P_{\text{dip}}}. \tag{3.8c}$$

### 3.2.3 Discussion of the ideal measurement scheme

By comparing Eqs. (3.8) with Eqs. (3.4), we find that the imprecision-backaction product $S^j_{\text{imp}}S^j_{\text{ba}} = [\hbar/(4\pi)]^2$ fulfills the Heisenberg uncertainty relation with equality for all three axes $j \in \{x, y, z\}$ [59]. Accordingly, our measurement scheme decodes the scatterer's position in an optimal way along all three axes simultaneously. It is instructive to consider the angular dependence of the contributions to the measurement imprecision in Eqs. (3.7). To this end, we inspect their (normalized) inverse $\mathcal{I}_j(\theta,\phi) = S^j_{\text{imp}}/s^j_{\text{imp}}(\theta,\phi)$. This quantity resembles the angular information density about the scatterer's position along the axis $j$. As an example, let us consider motion along the $x$ axis, shown in Fig. 3.2(a). We plot $\mathcal{I}_x(\theta,\phi)$ such that its value is encoded as the radial distance of the contour to the origin. We observe that the information content $\mathcal{I}_x$ vanishes in the plane $x = 0$. This means that a detector located anywhere in this plane cannot extract any information about the scatterer's position along $x$. This observation makes sense, since any displacement along $x$ (to linear order) has no influence on the phase of the field scattered in the plane $x = 0$. Furthermore, also a detector located on the (positive or negative) $x$ axis cannot infer any information about the motion along $x$. This observation might be surprising at first sight, since the phase shift of the scattered signal along this direction should be most sensitive to the scatterer's position along $x$. However, a linearly polarized dipole radiates no far field along its axis and the measurement signal vanishes along the $x$ axis. In Fig. 3.2(b), we show a cross section of $\mathcal{I}_x$ in a plane containing the $x$ axis (which is an axis of symmetry for $\mathcal{I}_x$). We have cross-hatched the region where the signal $\mathrm{d}p_{\text{det}}(\theta,\phi)$ is

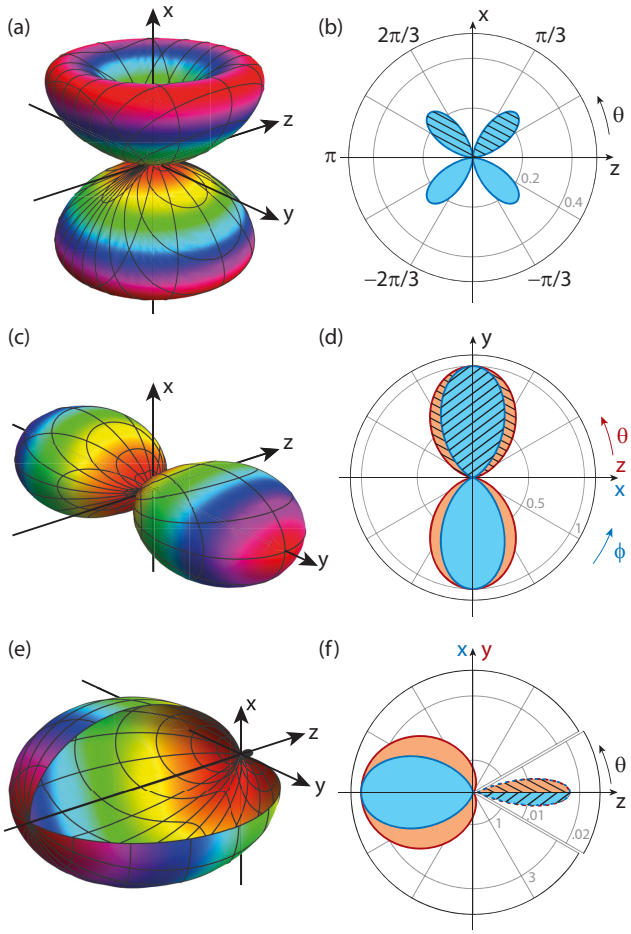


**Figure 3.2:** Information radiation patterns. (a) Contour plot of the information radiated into a unit solid angle. We plot the quantity $\mathcal{I}_x(\theta, \phi)$ as the radial distance of the contour to the origin. (b) Cross section through $\mathcal{I}_x$ in the plane $xz$. The cross-hatched region indicates where a displacement $x_0 > 0$ gives rise to a positive detector signal $\mathrm{d}p_{\mathrm{det}}(\theta, \phi)$. (c) Contour plot of $\mathcal{I}_y$. (d) Cross sections of $\mathcal{I}_y$ in the plane $xy$ (blue, inner area) and $yz$ (red, outer area). (e) Contour plot of $\mathcal{I}_z$. Note that the information is mostly radiated in the negative $z$ direction. (f) Cross sections of $\mathcal{I}_z$ in the $xz$ plane (blue, inner area) and in the $yz$ plane (red, outer area). Note the different radial scale in the range $-\pi/6 \leq \theta \leq \pi/6$. $A$ was fixed to $\cos(\pi/6) = 0.866$.

positive for a positive displacement $x_0$ of the scatterer, which is the case in the half space $x > 0$. In Fig. 3.2(c), we show $\mathcal{I}_y(\theta, \phi)$. We see that most information about the scatterer's position along $y$ is radiated along the $y$ axis. This observation makes sense, since both the radiation pattern of the dipolar scatterer and the dependence of the phase of the scattered field on the position along the $y$ axis reach a maximum along that direction. In Fig. 3.2(d), we show a cross section of $\mathcal{I}_y$ in the $yz$ plane (red, outer area) and in the $xy$ plane (blue, inner area). The signal $\mathrm{d}p_{\mathrm{det}}(\theta, \phi)$ is positive for positive $y_0$ in the half space $y > 0$.

The quantity $\mathcal{I}_z(\theta, \phi)$ shown in Fig. 3.2(c) is particularly interesting. In contrast to $\mathcal{I}_x$ ($\mathcal{I}_y$), which bears a symmetry relative to the plane $x = 0$ ($y = 0$), $\mathcal{I}_z$ has no symmetry relative to $z = 0$. This symmetry is broken by the propagating nature of the beam illuminating the scatterer. It turns out that more than 90% of the entire information about the position along the $z$ axis is contained in the field scattered in the backward direction (half space $z < 0$). This observation can be intuitively understood in the limiting case of a plane wave illuminating the scatterer ($A = 1$). In this case, the phase of the field scattered in the forward direction on the optical axis is independent of the scatterer's position along the $z$ axis.

Let us recap at this point the essential features of the optimal measurement scheme discussed thus far. The first feature is the optimal reference field in Eq. (3.5). This position-dependent field has to locally match the polarization of the field radiated by the scatterer. Second, the optimal reference field has to be phase shifted by $\pi/2$ relative to the scattered field. Finally, the differential detector signal collected on a detector under the direction $(\theta, \phi)$ has to be appropriately weighted according to its inverse imprecision noise as given by Eqs. (3.7) to obtain the optimal measurement of the scatterer's position. The total measurement imprecision of this scheme, given by Eqs. (3.8), multiplies with the measurement backaction given by Eqs. (3.4) to fulfill the Heisenberg uncertainty relation with equality in each direction $(x, y, z)$.

## 3.3 Realistic detection system

Thus far, we have analyzed the problem of detecting the position of a dipolar scatterer and described an ideal measurement scheme that allows for a Heisenberg-limited measurement of the scatterer's position in three dimensions. Two experimental difficulties make our ideal measurement scheme impractical. First, it is challenging to generate a reference field, the phase and polarization of which match those of a dipolar field, as required by Eq. (3.5). Reference fields typically available in a laboratory setting are Gaussian beams with uniform polarization. Second, this ideal measurement scheme requires a distribution of infinitesimal detectors spanning the full $4\pi$ of solid angle, where the signal from each detector is individually weighted according to its imprecision. In contrast, in practice one typically uses a simple four-quadrant detector [69].

### 3.3.1 Forward detection

In this section we consider the performance of the most commonly used detection system in optical trapping experiments, which relies on a standard (four-quadrant) split detection scheme in the forward direction [69]. The situation under consideration is sketched in Fig. 3.3. A first lens (termed the 'trapping lens') focuses an $x$ polarized plane wave (corresponding to a strongly overfilled objective) such that the focal point coincides with the origin. The optical axis is along $z$, and a second lens (termed the 'collection lens')

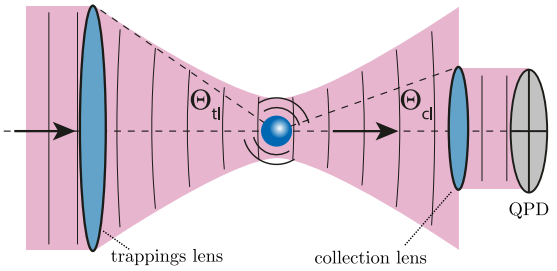


**Figure 3.3:** Laboratory detection system. A trapping lens with numerical aperture $\mathrm{NA}_{\mathrm{tl}} = \sin(\Theta_{\mathrm{tl}})$ focuses an $x$ polarized plane wave. On the opposite side, the fields are collimated by a collection lens with numerical aperture $\mathrm{NA}_{\mathrm{cl}} = \sin(\Theta_{\mathrm{cl}})$. A particle close to the focal point scatters the focused field.

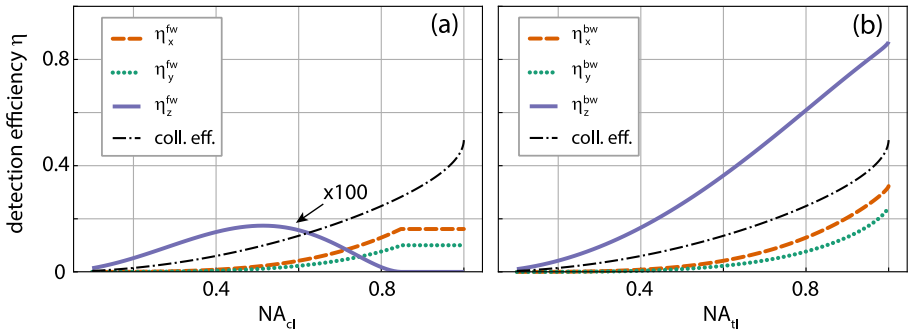


**Figure 3.4:** (a) Detection efficiency $\eta^{\mathrm{fw}}$ in the forward detection for a trapping lens with $\mathrm{NA_{tl}} = 0.85$. We plot the detection efficiencies for motion in the focal plane $\eta_x^{\mathrm{fw}}$ (red dashed), $\eta_y^{\mathrm{fw}}$ (green dotted) as a function of $\mathrm{NA_{cl}}$. The detection efficiency along the optical axis $\eta_z^{\mathrm{fw}}$ (blue solid), multiplied by factor 100, vanishes when $\mathrm{NA_{tl}} = \mathrm{NA_{cl}}$. In the range $\mathrm{NA_{cl}} > \mathrm{NA_{tl}}$, the detection efficiencies stay constant, since no reference field is available in that range. We also plot the fraction of the scattered power which is collected by the optics (black dash-dotted). (b) Detection efficiency $\eta^{\mathrm{bw}}$ in the backward detection. In the transverse directions, $\eta^{\mathrm{bw}}$ is identical to the case of forward detection shown in (a). However, most information about the motion along $z$ is encoded in the backscattered field, such that $\eta_z^{\mathrm{bw}}$ (blue solid) reaches values exceeding 0.6 for realistic trapping lenses with $\mathrm{NA_{tl}} > 0.8$.

recollimates the trapping beam. A dipolar scatterer is located close to the origin and generates the scattered field $\mathbf{E}_{\mathrm{sc}}(\mathbf{r})$ given by Eq. (3.2). For detection in the forward direction, the reference field Eq. (3.5) has to be replaced by the field of the trapping beam arriving on the detector.

As detailed in Appendix D.4, and in analogy to Sec. 3.2.2, we calculate the measurement imprecision $S_{\mathrm{imp}}^{j,\mathrm{fw}}$ of this forward detection scheme for all three axes $j \in \{x, y, z\}$. In order to compare our results for forward detection with the ideal case discussed in Sec. 3.2.2, we define the detection efficiency $\eta_j^{\mathrm{fw}} = S_{\mathrm{imp}}^{j}/S_{\mathrm{imp}}^{j,\mathrm{fw}}$ for the axis $j$ as the ratio of the result for forward scattering $S_{\mathrm{imp}}^{j,\mathrm{fw}}$ and the measurement imprecision at the Heisenberg limit given by Eqs. (3.8). Thus, the detection efficiency is a measure for how close to the Heisenberg limit a detection system operates. Note that absorption losses or a limited quantum efficiency of the detector further decrease the detection efficiency.

In Fig. 3.4(a), we plot the detection efficiencies $\eta_x^{\mathrm{fw}}$ (red dashed), $\eta_y^{\mathrm{fw}}$ (green dotted), and $\eta_z^{\mathrm{fw}}$ (blue solid) in forward scattering as a function of the numerical

aperture of the collection lens $\mathrm{NA}_{\mathrm{cl}}$ for a numerical aperture of the trapping lens $\mathrm{NA}_{\mathrm{tl}} = 0.85$. As expected, a larger $\mathrm{NA}_{\mathrm{cl}}$ generally leads to higher detection efficiency for all three axes. However, the detection efficiency for the $z$ axis $\eta_z^{\mathrm{fw}}$ shows a remarkable feature. It turns out that $\eta_z^{\mathrm{fw}}$ vanishes for a symmetric setup, *i.e.*, when the numerical aperture of the trapping lens equals that of the collection lens. We discuss this feature quantitatively in Appendix D.4. It can be understood qualitatively by close inspection of Fig. 3.2(f) from the discussion of the ideal measurement scheme. As indicated by the cross-hatched regions in the polar plot, the signal changes sign in the half space $z > 0$. In the specific case of a symmetric setup ($\mathrm{NA}_{\mathrm{tl}} = \mathrm{NA}_{\mathrm{cl}}$), the integration over $\theta$ is truncated such that the result strictly vanishes.

Let us apply our insights to realistic experimental conditions. For typical values of $\mathrm{NA}_{\mathrm{cl}} = 0.7$, the detection efficiency of the transverse modes in the forward direction is around $\eta_x^{\mathrm{fw}} \sim \eta_y^{\mathrm{fw}} \sim 0.1$, while for the longitudinal mode it is about two orders of magnitude smaller ($\eta_z^{\mathrm{fw}} \sim 0.001$).

### 3.3.2 Backward detection

We now turn to detection in the backward direction. Here, the backscattered light is collected by the trapping objective and then interfered with an external reference field [39]. In contrast to forward scattering, where the reference beam is naturally phase locked with the right phase shift (due to the common-path arrangement together with the Gouy phase shift), backward scattering is technically more involved, since the phase shift of the reference beam relative to the scattering signal has to be actively stabilized to a value of $\pi/2$. To compare with forward scattering, we consider a reference field that has the same spatial distribution as the trapping beam (a truncated plane wave).

In Appendix D.4.2 we derive expressions for the detection efficiencies $\eta_j^{\mathrm{bw}}$ in the backward direction, which are plotted in Fig. 3.4(b) as a function of the numerical aperture of the trapping lens $\mathrm{NA}_{\mathrm{tl}}$. We find that the detection efficiencies for motion in $x$ and $y$ directions are the same for forward and backward detection, *i.e.*, $\eta_x^{\mathrm{bw}} = \eta_x^{\mathrm{fw}}$ and $\eta_y^{\mathrm{bw}} = \eta_y^{\mathrm{fw}}$. This result is expected, since the information about motion along $x$ and $y$ is radiated symmetrically in the forward and in the backward direction [compare Figs. 3.2(a,c)]. On the other

hand, for motion along the $z$ direction, we find that the detection efficiency is much higher in the backward direction than in the forward direction. This result can be anticipated from the distribution of radiated information content shown in Figs. 3.2(e,f). For a typical value of the numerical aperture of the trapping lens $\mathrm{NA}_{\mathrm{tl}} = 0.8$, we find the efficiency to be as high as $\eta_z^{\mathrm{bw}} = 0.6$.

### 3.3.3 Discussion of real-world measurement schemes

Let us recap the most important insights gained from our analysis. Clearly, forward and backward detection using quadrant detectors fall short of reaching the Heisenberg limit of maximum detection efficiency $\eta = 1$, where the imprecision-backaction product has its minimum. Several factors contribute to this imperfection. First, the numerical aperture collecting the light scattered by the dipole is finite and, as a result, part of the information about the dipole's position is not collected. We plot the fraction of collected power as a function of numerical aperture in Fig. 3.4 as the black dash-dotted lines. Importantly, not every collected photon carries the same amount of information. For example, motion along the $z$ axis is predominantly encoded in the field scattered in the backward direction, allowing for a large detection efficiency for the $z$ motion in backscattering. Another factor limiting the detection efficiency is the imperfect overlap of the reference field (with homogeneous polarization) with the field scattered by the dipole (the polarization of which varies spatially). Finally, an ideal detection system must not only collect the measurement signal across the full solid angle surrounding the scatterer, but must also weight the individual contributions according to their information content as given by the measurement imprecision. Clearly, a quadrant detector offers very limited capability to perform this weighting procedure. Consider, for example, detection of the $y$ motion. It is clear from Fig. 3.2 that practically no information is contained in the signal striking the detector close to the $z$ axis. Nevertheless, a standard detector will sum the shot-noise contribution generated in this region by the reference field and add it to the output signal. A possible alternative to a spatially resolving detector would be a reference field with an appropriately shaped spatial intensity distribution. Such a field distribution could, for example, be generated using a spatial light modulator.

In this chapter we solely consider a dipolar scatterer much smaller than the wavelength. For particles comparable to or even larger than the wavelength [14, 15, 23, 24], one in general needs to solve the full scattering problem in order to calculate the far field and its phase dependence on the object's position. Following an analysis analogous to the one described here, one can then find both the total measurement backaction as well as an ideal local-oscillator field allowing for detection at the Heisenberg limit.

Finally, let us consider the repercussions of our findings for active feedback cooling of a levitated nanoparticle's motion. Considering the finite transmissivity of optical components, the finite quantum efficiency of photodetectors, and our finding that the detection efficiency for the motion along the optical axis in backward scattering can reach $\eta_z^{\mathrm{bw}} \sim 0.8$, we conclude that a total efficiency of 0.35 appears well within reach. Adding the fact that at sufficiently low pressures the reheating of a levitated particle is dominated by measurement backaction [41], active feedback by means of cold damping [58, 63] should be able to cool a levitated nanoparticle in a free-space configuration with only a single laser beam to mean phonon occupation numbers as low as $n = (1/\sqrt{\eta} - 1)/2 = 0.35$ along the optical axis, and thus to the quantum ground state of motion.

## 3.4 Conclusions

We have theoretically analyzed the problem of determining the position of a dipolar scatterer in a focused field. We have proposed an ideal detection scheme locating the scatterer in three dimensions at the Heisenberg limit of the imprecision-backaction product. Furthermore, we have analyzed configurations commonly used in experiments and derived their measurement efficiencies. We have found that for realistic experimental setups, the detection efficiencies for motion transverse to the optical axis are limited to $\eta_{x,y} \sim 0.1$. On the other hand, our analysis shows that the motion along the optical axis is most efficiently detected in backscattering, where the detection efficiency of the longitudinal motion can be as high as 80%, such that ground-state cooling of a levitated particle in a single beam optical trap should be feasible.

# 4

# Motional sideband asymmetry

This chapter is based on the article F. Tebbenjohanns, M. Frimmer, V. Jain, D. Windey, and L. Novotny, Phys. Rev. Lett. **124**, 013603 (2020).

*The hallmark of quantum physics is Planck's constant $h$, whose finite value entails the quantization that gave the theory its name. The finite value of $h$ gives rise to inevitable zero-point fluctuations even at vanishing temperature. The zero-point fluctuation of mechanical motion becomes smaller with growing mass of an object, making it challenging to observe at macroscopic scales. Here, we transition a dielectric particle with a diameter of* $136\,\mathrm{nm}$ *from the classical realm to the regime where its zero-point motion emerges as a sizable contribution to its energy. To this end, we optically trap the particle at ambient temperature in ultrahigh vacuum and apply active feedback cooling to its center-of-mass motion. We measure an asymmetry between the Stokes and anti-Stokes sidebands of photons scattered by the levitated particle, which is a signature of the particle's quantum ground state of motion.*

## 4.1 Introduction

A paradigm of quantum mechanics is a mass bound in a harmonic potential with angular oscillation frequency $\Omega$. According to quantum theory, the state of the mass can be described as a superposition of energy eigenstates. These states are enumerated by the quantum (or occupation) number $n$ with respective energies $E_n = \hbar\Omega(n+1/2)$, where $\hbar = h/(2\pi)$ is the reduced Planck constant [78–80]. For a harmonic oscillator coupled to a thermal bath at temperature $T$, the mean occupation number is given by

$$\bar{n} = \left[\exp\left(\frac{\hbar\Omega}{k_B T}\right) - 1\right]^{-1}, \tag{4.1}$$

known as the Bose-Einstein distribution (with $k_B$ the Boltzmann constant) [59]. For thermal energies large compared to the energy quantum ($k_B T \gg \hbar\Omega$), the mean energy of the harmonic oscillator is $\bar{E} = k_B T$ in agreement with classical statistical mechanics, and $\hbar$ makes no appearance. However, for zero temperature, the oscillator retains the zero-point energy $E_0 = \hbar\Omega/2$, whose existence can be interpreted as a result of the finite value of Planck's constant.

A particularly striking experiment to demonstrate the existence of the quantum ground state of an oscillator is Raman scattering, where light at the angular frequency $\omega$ is scattered into a Stokes sideband at $\omega - \Omega$ and an anti-Stokes sideband at $\omega + \Omega$. Stokes scattering is an inelastic process raising the population of the mechanical oscillator by a single quantum of energy (termed phonon), while anti-Stokes scattering corresponds to lowering the oscillator's population by one quantum. Importantly, anti-Stokes scattering is impossible by an oscillator in its quantum ground state. As a result, the powers in the anti-Stokes and Stokes sidebands differ. In the limit of $\Omega \ll \omega$, their ratio is given by

$$\frac{\bar{n}}{\bar{n}+1} = \exp\left(-\frac{\hbar\Omega}{k_B T}\right) \tag{4.2}$$

and can serve as a temperature measurement calibrated relative to the quantum of energy of the system $\hbar\Omega$ [59]. In molecular systems, the oscillator frequency $\Omega$ can be sufficiently high to make the Raman-sideband asymmetry a feature of quantum mechanics routinely exploited even at room temperature [81–

83]. Furthermore, pioneering experiments using laser-cooling techniques have investigated atoms and atom clouds in their motional ground states in optical traps [84–86].

During the last decades, quantum mechanics has been tested on increasingly massive objects [87]. In particular, macroscopic mechanical oscillators are now being used for optical measurements operating at the limits set by quantum theory [7, 88, 89]. Together with the remarkable progress in measurement precision, optical techniques have been developed to not only sense but also control mechanical motion at the quantum level [90–94]. Using the forces of light, nano- and micro-mechanical oscillators have been cooled to their quantum ground states in schemes relying both on autonomous [27, 28] and active-feedback mechanisms [29]. Thus far, besides requiring cryogenic precooling, all experiments demonstrating optical quantum control of mesoscopic mechanical oscillators rely on coupling the mechanical degree of freedom to an optical resonator to boost the light-matter interaction strength [12, 95].

Here, we transition a mesoscopic mechanical oscillator from the classical to the quantum domain without the need for cryogenic cooling nor requiring coupling to an optical cavity. The oscillator is a dielectric sphere with a diameter of $136\,\mathrm{nm}$, levitated in ultrahigh vacuum in a single-beam optical dipole trap [13, 16, 18, 25, 41]. We use measurement-based linear-feedback cooling (as described in Ch. 2) to reduce the effective temperature of the particle's center-of-mass motion from room temperature by seven orders of magnitude to observe the emergence of the Raman-sideband asymmetry in the light scattered by the particle. Sideband thermometry yields a phonon occupation number of $\bar{n} = 4$.

## 4.2 Experimental setup

Our experimental setup is shown in Fig. 4.1. We focus a linearly polarized laser beam (wavelength $1064\,\mathrm{nm}$, focal power $130\,\mathrm{mW}$) with a microscope objective ($0.85\,\mathrm{NA}$) in vacuum ($7.5 \times 10^{-9}\,\mathrm{mbar}$) to generate an optical dipole trap for a silica nanoparticle (diameter $136\,\mathrm{nm}$). The oscillation frequencies of the particle's center of mass are $\Omega_z = 2\pi \times 50\,\mathrm{kHz}$, $\Omega_x = 2\pi \times 130\,\mathrm{kHz}$, and $\Omega_y = 2\pi \times 150\,\mathrm{kHz}$, where $z$ denotes the direction along the optical axis

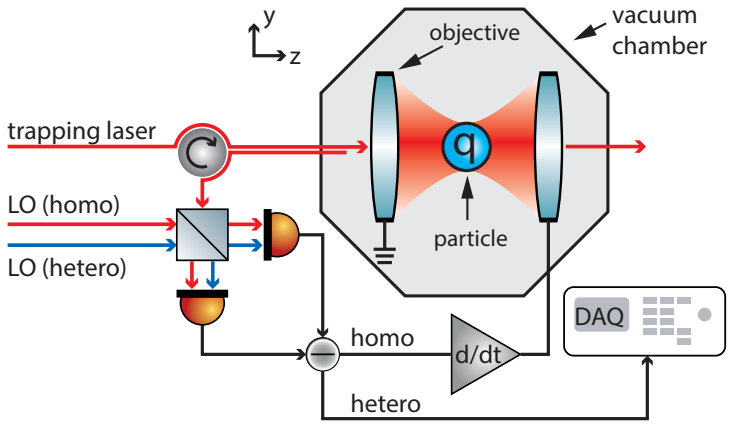


**Figure 4.1:** Experimental setup. A silica nanoparticle carrying a finite net charge $q$ is optically trapped in vacuum using a laser beam focused by an objective. To measure the $z$ motion of the particle, the backscattered light is rerouted by a free-space circulator and mixed with two local oscillators (LO) for simultaneous homodyne (homo) and heterodyne (hetero) detection. The time derivative of the homodyne signal is applied to a capacitor consisting of the holders for the trapping objective and the collection lens, and enclosing the particle for cold damping. The heterodyne signal is recorded for sideband thermometry.

and $x$ ($y$) denotes the coordinate in the focal plane along (orthogonal to) the axis of polarization. By means of parametric feedback, we cool the particle motion along the $x$ and $y$ directions to temperatures below $1\,\mathrm{K}$ to eliminate nonlinear cross-coupling between the translational degrees of freedom [41]. In the following, we focus on the particle's motion along the optical $z$ axis.

To profit from a maximized measurement efficiency as explained in chapter 3, we detect the motion of the particle along the $z$ axis using the light scattered back into the trapping objective [96]. The backscattered light is sent through a Faraday rotator and detected in a balanced detection scheme. Here, we mix the signal beam with both a homodyne and a heterodyne (shifted by $\pm 1\,\mathrm{MHz}$) reference beam. We refer to the homodyne backscattering measurement as the in-loop signal, since we use it to derive a feedback signal proportional to the particle's velocity $\dot{z}$ along the optical axis [58]. This feedback signal is applied as a voltage to a capacitor enclosing the trapped particle. The particle carries a finite net charge, such that the feedback signal

directly translates into the Coulomb force $F_{\mathrm{fb}} = -m\gamma_{\mathrm{fb}}\dot{z}$ acting on the particle, with feedback gain $\gamma_{\mathrm{fb}}$ and mass $m$. The heterodyne signal measured in backscattering is used for an out-of-loop measurement of the particle motion. It provides a simultaneous measurement of the Stokes and anti-Stokes sidebands and therefore allows for sideband thermometry [92].

For more details of the experimental setup and the limits of our feedback scheme, we refer to appendices C and B, respectively.

## 4.3 Results

In Fig. 4.2, we show the heterodyne sidebands generated by the motion of the particle along the $z$ axis. A feedback gain of $\gamma_{\mathrm{fb}} = 2\pi \times 4\,\mathrm{kHz}$ is used and the local-oscillator frequency is shifted by $-1\,\mathrm{MHz}$ relative to the trap laser. Each sideband has the shape of a Lorentzian function on top of an approximately constant noise floor. We observe that the left sideband at a

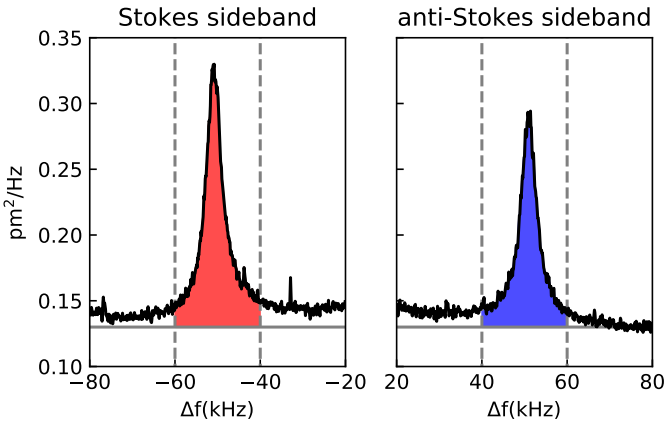


**Figure 4.2:** Motional sideband asymmetry. The figure shows single-sided power spectral densities $\tilde{S}_{zz}^{\mathrm{het}}(f)$ obtained by the heterodyne out-of-loop measurement. The frequency difference $\Delta f$ is measured relative to the (absolute) local-oscillator frequency shift of $1\,\mathrm{MHz}$. Spectra are taken simultaneously under linear feedback cooling with $\gamma_{\mathrm{fb}} = 2\pi \times 4\,\mathrm{kHz}$. We observe an asymmetry in the power contained in the two sidebands. The gray solid lines indicate the noise floor (limited by technical laser noise). The vertical dashed lines indicate the integration range. The calibration of the signal to absolute units follows the procedure outlined in Ref. [56].

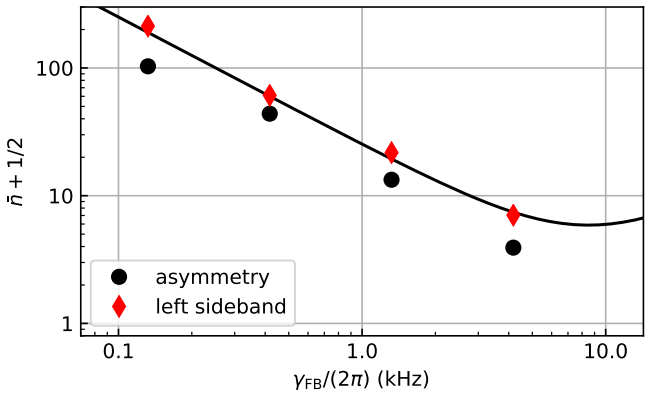


**Figure 4.3:** Mean occupation number as a function of feedback gain. The red diamonds are obtained by integrating the left sideband of the heterodyne spectrum according to Eq. (4.5). The black circles show the mean occupation number extracted from the sideband asymmetry according to Eq. (4.4). The black solid line corresponds to a parameter-free model according to Ref. [58]. Error bars (one standard deviation) are smaller than the symbol size.

frequency $\Delta f = -50\,\mathrm{kHz}$ (corresponding to Stokes scattering) carries more power than the right sideband at $\Delta f = +50\,\mathrm{kHz}$ (corresponding to anti-Stokes scattering). The power difference corresponds to the phonon energy $\hbar\Omega_z$ of the oscillator [59, 90–92, 97]. As a result, the mean occupation number $\bar{n}$ is related to the sideband asymmetry

$$R_- = \frac{\int \mathrm{d}f\ \tilde{S}_{zz}^{\mathrm{het,r}}(f)}{\int \mathrm{d}f\ \tilde{S}_{zz}^{\mathrm{het,l}}(f)}, \tag{4.3}$$

where $\tilde{S}_{zz}^{\mathrm{het,r}}$ ($\tilde{S}_{zz}^{\mathrm{het,l}}$) is the power spectral density of the right (left) sideband. We derive $R_-$ from the measured power spectral densities shown in Fig. 4.2. The integration range used throughout this work is indicated by the gray vertical dashed lines, and the horizontal gray solid line shows the noise floor that is subtracted before integration of the signal. We note that the measurement imprecision is not limited by quantum shot noise but by technical noise of the laser source. Importantly, the ratio $R_-$ can be influenced by the frequency-dependent transfer function of the measurement system. The measured asymmetry hence is $R_- = R_{\mathrm{TF}}\,\bar{n}/(\bar{n}+1)$, where $R_{\mathrm{TF}}$ is the ratio of the transfer function at the two

sidebands. To eliminate this classical effect as a possible source for the sideband asymmetry, we swap the position of the left and the right sideband by switching the frequency shift of the heterodyne reference from $-1\,\mathrm{MHz}$ to $+1\,\mathrm{MHz}$. With this reversed frequency shift, the left (right) sideband corresponds to anti-Stokes (Stokes) scattering, and we determine the corresponding sideband asymmetry $R_+ = R_{\mathrm{TF}}\,(\bar{n}+1)/\bar{n}$. Based on the sideband asymmetries $R_+$ and $R_-$, we can extract the mean phonon occupation $\bar{n}$ from the relation [59]

$$\sqrt{\frac{R_-}{R_+}} = \frac{\bar{n}}{\bar{n}+1}. \tag{4.4}$$

In Fig. 4.3, we plot as black circles the mean occupation number $\bar{n}$ of the $z$ mode of the particle as deduced from the sideband asymmetry according to Eq. (4.4) as a function of feedback gain $\gamma_{\mathrm{fb}}$. At a feedback gain of $\gamma_{\mathrm{fb}} = 2\pi \times 4\,\mathrm{kHz}$, we obtain an occupation of $\bar{n} = 4$.

In the following, we provide two cross-checks to corroborate our sideband-thermometry measurements. As a first check, we directly relate the power in the Stokes sideband to the energy of the motion, as commonly done in levitated optomechanics, using the relation

$$\bar{n} + 1 = c \int \mathrm{d}f\; \tilde{S}_{zz}^{\mathrm{het,\,1}}(f). \tag{4.5}$$

The resulting phonon occupation is shown as red diamonds in Fig. 4.3. Importantly, this procedure relies on a calibration factor $c$ which is determined in the mildly underdamped regime at $10\,\mathrm{mbar}$, where the particle is equilibrated to room temperature and behaves entirely classically* [56]. Therefore, the red diamonds in Fig. 4.3 can be interpreted as an energy measurement relative to the classical quantity $k_B T$ (with $T \sim 300\,\mathrm{K}$). In contrast, the black circles in Fig. 4.3 represent a measurement relative to the quantum of energy $\hbar\Omega_z$. The agreement between the two methods is satisfying. The observed difference can be ascribed to a systematic error of the classical calibration constant $c$, which is known to drift when reducing the pressure in the vacuum chamber [56]. We note that we have excluded any influence of (classical) laser intensity

*A detailed description of our calibration procedure is given in App. C.2.1

noise on the asymmetry exceeding the statistical uncertainty. To this end, we have compared sideband-thermometry measurements at different levels of laser intensity noise in the trap [94]. Details on our active laser stabilization can be found in App. C.1.

As a second consistency check, we compare our experimental results to the model of a cold-damped oscillator [48], following the procedure outlined in Ref. [58]. To this end, we quantify the coupling of the particle to the thermal bath by performing ring-down and reheating experiments. Together with the noise floor of the in-loop measurement, we obtain a parameter-free calculation of the expected energy under feedback cooling (black line in Fig. 4.3). The model (which relies on the classical energy-calibration constant) is in excellent agreement with the classically obtained measurements (red diamonds).

## 4.4 Discussion and conclusion

We have carried out two different measurements of the center-of-mass energy of a levitated oscillator. First, we have measured the energy relative to room temperature (red diamonds in Fig. 4.3). Second, we have measured the energy relative to the ground state energy $\hbar\Omega_z/2$ (black circles) and found satisfactory agreement between both methods. Thus, our experiments bring an optically levitated oscillator from the classical to the quantum regime, where zero-point fluctuations have a sizable contribution to the particle's energy. Let us discuss the limits of our cooling experiments. Detection of the oscillation along the optical axis ($z$ mode) in backscattering should allow the phonon population to be cooled below unity [96]. A straightforward route toward reaching this limit is to reduce laser noise on the detector to the shot noise limit in combination with a reduction in pressure by an order of magnitude to eliminate gas heating.

In conclusion, we have measured the sideband asymmetry in the motional spectrum of a levitated oscillator. This asymmetry is an unambiguous signature of the quantum ground state of the harmonic oscillator and arises in the limit of small phonon occupation numbers. Using active feedback cooling, we have compressed the center-of-mass energy of a harmonic oscillator by more than seven orders of magnitude, transitioning the system from the classical realm to the quantum regime. Importantly, all previous demonstrations of cooling a

mechanical oscillator to the quantum regime relied on cryogenic precooling and were accompanied by coupling to an optical cavity, either in order to capitalize on autonomous resolved sideband cooling, or to boost the measurement efficiency in an active feedback cooling scheme. In contrast, we use a single laser beam to trap a nanoparticle in free space. This configuration requires little experimental overhead and offers the advantage of largely unobstructed measurements and the opportunity to control the trapping potential spatially and temporally via the light field. These features of optically levitated oscillators hold promise for fundamental tests of physics in yet unexplored parameter regimes [21, 22]. At the same time, the absence of an optical resonator removes any timing constraints posed by the finite response time of a cavity. This fact might prove beneficial for optomechanical control schemes relying on fast pulse sequences [98].

# 5

# Optomechanics in free space

## 5.1 Introduction

In this thesis we strive toward bringing both measurement and control of the center-of-mass motion of an optically levitated nanoparticle to the quantum limit. Much of our work is inspired by cavity optomechanics, but notably we do not have an optical cavity in our setup. Over the last decades, a rich framework of cavity optomechanics has been developed [12, 66, 99]. In the canonical setting, a laser light field is sent to an optical cavity and the reflected or transmitted light is analyzed on a photodetector. The cavity field can exchange energy with a mechanical (phononic) mode through radiation pressure, which allows for both control and analysis of the mechanical motion through the input and output light fields.

In this chapter we provide a theoretical framework of a cavity-free optomechanical setup including a heterodyne detection scheme of the output field. Our toy model consists of a mirror in harmonic motion, off which we reflect a probe laser. The reflected laser beam is analyzed on a photodetector and the resulting photocurrent represents a measure of the mirror's position. In Sec. 5.2, we derive input-output relations for our system in the spirit of the theory by

Gardiner and Collett [100] and find an expression for the reflected light field. In Sec. 5.3, we analyze the photodetection process based on the theory put forward by Glauber [101] and find the statistical properties of the photocurrent as a function of the light field, which is impinging on the detector. In Sec. 5.4, we extend the detection scheme to allow for heterodyne detection. Combining the previously obtained results, in Sec. 5.5, we compute the spectrum of a heterodyne detector which measures the output field of our optomechanical setup. A feature of the computed spectrum is the motional sideband asymmetry, which we have observed experimentally in Ch. 4.

We note that in the optomechanics literature, an alternative model of the heterodyne detection process in contradiction to Glauber's theory is often used. We repeat the computation of the detected spectrum with this alternative model and compare both results. Our conclusion agrees with that of Børkje for a cavity-based system [102]. Both models predict the same spectrum, but depending on the chosen detection model, the sideband asymmetry is either due to the zero-point fluctuations (ZPF) of the mechanical motion or the ZPF of the light. Finally, in Sec. 5.6, we map our framework to cavity optomechanics. This allows us to extract system parameters like the quantum cooperativity and the measurement rate, which can then be compared to cavity setups.

## 5.2 Input-output formalism

The canonical description of quantum optomechanics consists of two resonators, an optical cavity and a mechanical oscillator, which are coupled through

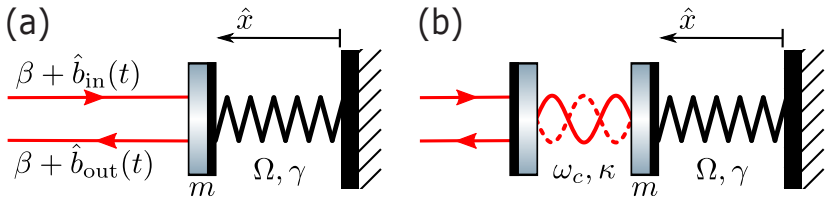


**Figure 5.1:** (a) Mirror on a spring in cavity-free setup. Symbols are explained in the text. (b) For comparison: Canonical optomechanical setup with a cavity with resonance frequency $\omega_c$ and linewidth $\kappa$, coupled to a mechanical oscillator.

radiation pressure. As depicted in Fig. 5.1(b), the input and output optical fields interact solely with the cavity field, which in turn interacts with the mechanics. Commonly, the outputs of the system are described in terms of the inputs in a scattering picture [100]. Here, we describe our levitated and oscillating particle as a mirror on a spring, off which we reflect light without the need of a cavity. Compared to cavity optomechanics, we therefore have a slightly simpler setup, where the input and output fields directly couple to the motion of the mirror. In the following derivation, we describe the system classically and later quantize the fields. The found expressions reflect those found in cavity optomechanics [66, 100].

Our toy model is depicted in Fig. 5.1(a). Our mirror with mass $m$ and position $x$ is forming a harmonic oscillator with eigenfrequency $\Omega$ and damping rate $\gamma$. A coherent light field $b_{\text{in}}(t)$ at frequency $\omega_{\text{L}}$ is reflected off the mirror to the output mode $b_{\text{out}}(t)$. In our notation, the fields are scaled such that $|b_{\text{in}}(t)|^2$ ($|b_{\text{out}}(t)|^2$) is the photon flux of the probe (reflected) beam in units of Hz. The equation of motion of $x$ is that of a harmonic oscillator

$$\ddot{x} + \gamma\dot{x} + \Omega^2 x = \frac{F_{\text{th}}(t) - F_{\text{rp}}(t)}{m}, \tag{5.1}$$

driven by a fluctuating force $F_{\text{th}}(t)$ due to the thermal bath and by radiation pressure $F_{\text{rp}}(t)$ due to the probe beam. Since each photon delivers momentum $2\hbar k$ with wavenumber $k$ to the mirror upon reflection, we can express the radiation pressure force as [42]

$$F_{\text{rp}}(t) = 2\hbar k|b_{\text{in}}(t)|^2. \tag{5.2}$$

The reflected light beam carries an additional phase factor $2kx(t)$ as compared to the impinging light. For small displacements $|2kx| \ll 1$, we find for the output mode

$$b_{\text{out}}(t) = b_{\text{in}}(t)\mathrm{e}^{-2\mathrm{i}kx(t)} \approx b_{\text{in}}(t)[1 - 2\mathrm{i}kx(t)]. \tag{5.3}$$

Note that the sign of the phase factor $2kx(t)$ must be negative in this case due to our choice of the coordinate system. Now, we will quantize the mechanics

$x \to \hat{x}(t)$ and the input light field $b_{\text{in}}(t) \to \beta + \hat{b}_{\text{in}}(t)$, where $\hat{x}(t)$ and $\hat{b}_{\text{in}}(t)$ are operators in the Heisenberg picture, and $\beta = \langle b_{\text{in}}(t) \rangle$ is the mean value of the light field. The operator $\hat{b}_{\text{in}}(t)$ is therefore zero mean and solely describes the vacuum fluctuations of the probe beam. While in principle $\beta$ is complex valued, its phase is a global phase that we cannot detect and we can set $\beta$ to be real. Assuming that we are driving the system with a large coherent field, that is, $\beta$ largely exceeds $\hat{b}_{\text{in}}(t)$, we can linearize the radiation-pressure force in Eq. (5.2) as

$$\hat{F}_{\text{rp}}(t) \approx 2\hbar k \left[ \beta^2 + \beta \hat{b}_{\text{in}}^\dagger(t) + \beta \hat{b}_{\text{in}}(t) \right]. \tag{5.4}$$

The first, constant term is a DC force, which only results in a shift of the oscillator's mean position, and we will omit it in the following. For the same assumptions (large coherent drive and small mechanical oscillations), we find for the output field [Eq. (5.3)]

$$\begin{aligned} b_{\text{out}}(t) &\to \left[ \beta + \hat{b}_{\text{in}}(t) \right] \left[ 1 - 2\mathrm{i} k \hat{x}(t) \right] \\ &\approx \beta + \hat{b}_{\text{in}}(t) - 2\mathrm{i}\beta k \hat{x}(t) \\ &=: \beta + \hat{b}_{\text{out}}(t). \end{aligned} \tag{5.5}$$

We see that the (constant) amplitude $\beta$ of the reflected light is the same as that of the input, but the fluctuations $\hat{b}_{\text{out}}(t)$ are increased by the motion of the mechanics. To summarize, we have the following equations of motion of the system:

$$\hat{x}(t) = \chi(t) \circledast \left[ \hat{F}_{\text{th}}(t) - 2\hbar k \beta \left[ \hat{b}_{\text{in}}(t) + \hat{b}_{\text{in}}^\dagger(t) \right] \right], \tag{5.6a}$$

$$\hat{b}_{\text{out}}(t) = \hat{b}_{\text{in}}(t) - 2\mathrm{i}\beta k \hat{x}(t). \tag{5.6b}$$

Here, $\chi(t)$ denotes the mechanical susceptibility in time domain and $\circledast$ stands for convolution. In Fourier space, the susceptibility takes its Lorentzian form

$$\chi[\omega] = \frac{1}{m} \frac{1}{\Omega^2 - \omega^2 - \mathrm{i}\gamma\omega}. \tag{5.7}$$

The (thermal) bath forcing term $F_{\text{th}}(t)$ is now also a quantum mechanical operator $\hat{F}_{\text{th}}(t)$. From Eq. (5.6a), we can see that the mirror is driven by the

amplitude quadrature $\hat{b}_{\text{in}}^\dagger(t) + \hat{b}_{\text{in}}(t)$ of the light in addition to the thermal drive $\hat{F}_{\text{th}}(t)$. The signal $\hat{x}(t)$ is then imprinted on the phase quadrature $\hat{b}_{\text{out}}^\dagger(t) - \hat{b}_{\text{out}}(t)$ of the reflected light, see Eq. (5.6b).

Equations (5.6) describe the time evolution of the system's output mode $\hat{b}_{\text{out}}(t)$ as a function of the inputs $\hat{F}_{\text{th}}(t)$ and $\hat{b}_{\text{in}}(t)$. In this input-output formalism, the mechanical mode $\hat{x}(t)$ is merely an internal state which cannot be observed or controlled directly. In standard cavity optomechanics, an additional equation describes the time evolution of the cavity field mode [100].

Let us calculate the power spectral density (PSD) of the position operator $\hat{x}(t)$ from Eq. (5.6a). We find

$$S_{\hat{x}\hat{x}}(\omega) = |\chi[\omega]|^2 \left[ S_{\hat{F}\hat{F}}^{\text{th}} + 4\hbar^2 k^2 \beta^2 \left( S_{\hat{b}^\dagger \hat{b}^\dagger}^{\text{in}} + S_{\hat{b}\hat{b}}^{\text{in}} + S_{\hat{b}^\dagger \hat{b}}^{\text{in}} + S_{\hat{b}\hat{b}^\dagger}^{\text{in}} \right) \right], \tag{5.8}$$

where we used Eqs. (A.13) and $\chi[-\omega] = \chi[\omega]^*$. We also assumed that the thermal force fluctuations are independent of the light field's fluctuations. The superscript $^{\text{in}}$ indicates that the spectral densities belong to the input mode. For a shot noise limited input beam, we know that [66]

$$\left\langle \hat{b}_{\text{in}}(t+\tau) \hat{b}_{\text{in}}^\dagger(t) \right\rangle = \delta(\tau), \tag{5.9a}$$

$$\left\langle \hat{b}_{\text{in}}^\dagger(t+\tau) \hat{b}_{\text{in}}(t) \right\rangle = \left\langle \hat{b}_{\text{in}}(t+\tau) \hat{b}_{\text{in}}(t) \right\rangle = \left\langle \hat{b}_{\text{in}}^\dagger(t+\tau) \hat{b}_{\text{in}}^\dagger(t) \right\rangle = 0. \tag{5.9b}$$

The corresponding input spectral densities hence are (note our definition of cross- and autocorrelations in App. A)

$$S_{\hat{b}^\dagger \hat{b}^\dagger}^{\text{in}} = \frac{1}{2\pi}, \tag{5.10a}$$

$$S_{\hat{b}^\dagger \hat{b}}^{\text{in}} = S_{\hat{b}\hat{b}^\dagger}^{\text{in}} = S_{\hat{b}\hat{b}}^{\text{in}} = 0. \tag{5.10b}$$

This allows us to simplify Eq. (5.8) to

$$S_{\hat{x}\hat{x}}(\omega) = |\chi[\omega]|^2 \left[ S_{\hat{F}\hat{F}}^{\text{th}}(\omega) + S_{FF}^{\text{ba}} \right], \tag{5.11}$$

where $S_{FF}^{\text{ba}} = 2\hbar^2 k^2 \beta^2 / \pi$ is the back-action force noise. We can see that in addition to the thermal drive $S_{\hat{F}\hat{F}}^{\text{th}}(\omega)$, the light field acts on the mechanics like a white background proportional to the light intensity $\beta^2$. Quantum mechanics

dictates the thermal force PSD $S^{\text{th}}_{\hat{F}\hat{F}}(\omega)$ to be asymmetric in frequency with [59, 66, 102]

$$S^{\text{th}}_{\hat{F}\hat{F}}(\pm\omega) = \frac{m\gamma\hbar\omega}{\pi}\left(n_{\text{BE}} + \frac{1}{2} \pm \frac{1}{2}\right), \tag{5.12}$$

where $n_{\text{BE}}$ is the Bose-Einstein occupation factor [see Eq. (4.1)]. Positive and negative frequencies are associated with absorption and emission of energy by the oscillator, respectively. Both processes are inherently asymmetric due to the existence of a ground state from which the oscillator cannot emit energy.

Note that, despite the fact that both $\hat{F}_{\text{th}}(t)$ and $\hat{x}(t)$ are Hermitian operators with real expectation values, their respective PSDs are asymmetric in frequency with $S_{\hat{x}\hat{x}}(-\omega) \neq S_{\hat{x}\hat{x}}(\omega)$. This is impossible for classical, real-valued processes. In the following, we will analyze how this asymmetry can be measured in the spectrum of a (real-valued) photocurrent.

For later convenience, let us also compute the PSD $S^{\text{out}}_{\hat{b}\hat{b}}(\omega)$ of the output light $\hat{b}_{\text{out}}(t)$. From the input-output relation Eq. (5.6b) we find

$$\begin{aligned} S^{\text{out}}_{\hat{b}\hat{b}}(\omega) &= S^{\text{in}}_{\hat{b}\hat{b}}(\omega) + 4\beta^2 k^2 S_{\hat{x}\hat{x}}(\omega) + 4\beta k \,\text{Im}\, S^{\text{in}}_{\hat{b}\hat{x}}(\omega) \\ &= 4\beta^2 k^2 S_{\hat{x}\hat{x}}(\omega), \end{aligned} \tag{5.13}$$

where we made use of Eqs. (A.7), (5.10), and of

$$S^{\text{in}}_{\hat{b}\hat{x}} = -2\hbar k\beta\chi[\omega]^* \left(S^{\text{in}}_{\hat{b}\hat{b}} + S^{\text{in}}_{\hat{b}\hat{b}^\dagger}\right) = 0. \tag{5.14}$$

## 5.3 Absorption-based photodetection

Consider an electromagnetic field mode $\hat{a}(t)$ which impinges on an absorption-based photodetector. We assume unity detection efficiency such that each photon is converted into an electron. The photon flux (in Hz) must be described by the quantum-mechanical operator $\hat{i}(t) = \hat{a}^\dagger(t)\hat{a}(t)$, while the electron flux is generally described by a classical, real variable $i(t)$, since we assume that we can arbitrarily amplify, copy, and store it. In general, $i(t)$ is a random Gaussian process fully described by its first two momenta $\langle i(t)\rangle$ and $G_{ii}(\tau)$. The latter is the autocorrelation function, for which we assume both stationarity and ergodicity of $i(t)$.

In this section we derive $\langle i(t)\rangle$ and $G_{ii}(\tau)$ as functions of the quantum-mechanical operator $\hat{a}(t)$. One might be tempted to simply replace both quantities by their quantum-mechanical counterparts, *i.e.*, $\left\langle \hat{i}(t) \right\rangle$ and $G_{\hat{i}\hat{i}}(\tau)$. This, however, is unphysical since $\hat{i}(t)$ does not necessarily commute with itself at different times and hence $G_{\hat{i}\hat{i}}(\tau)$ can be complex valued, while $G_{ii}(\tau)$ must be real valued (see Sec. A.2). Also, the corresponding PSD $S_{\hat{i}\hat{i}}(\omega)$, given by the Fourier transform of $G_{\hat{i}\hat{i}}(\tau)$, can in general be asymmetric in frequency, while its classical counter-part $S_{ii}(\omega)$ must be symmetric in frequency.

According to the photodetection theory put forward by Glauber [101], and Kelley and Kleiner [103], the correlators of absorption-based photocurrents, must be replaced by the normally ordered version of their quantum-mechanical counterparts. In such a treatment, the first two momenta of the classical photocurrent $i(t)$ are [97, 104–107]

$$\langle i(t)\rangle = \left\langle : \hat{i}(t) : \right\rangle_t = \left\langle \hat{a}^\dagger(t)\hat{a}(t) \right\rangle_t \tag{5.15}$$

and

$$\begin{aligned} G_{ii}(\tau) &= \left\langle : \hat{i}(t+\tau)\hat{i}(t) : \right\rangle_t + \delta(\tau) \left\langle : \hat{i}(t) : \right\rangle_t \\ &= \left\langle \hat{a}^\dagger(t)\hat{a}^\dagger(t+\tau)\hat{a}(t+\tau)\hat{a}(t) \right\rangle_t + \delta(\tau) \left\langle \hat{a}^\dagger(t)\hat{a}(t) \right\rangle_t , \end{aligned} \tag{5.16}$$

where the colons stand for normal and time ordering. Normal ordering means that anything in between the colons needs to be expressed in terms of ladder operators and all creation operators need to shifted before all annihilation operators. Time ordering demands that from left to right the time arguments are increasing in creation and decreasing in annihilation operators [105]*. Note the second, delta-like term in the autocorrelation function. Carmichael showed that we need this correction factor at $\tau = 0$ [104]. It comes from the fact that at $\tau = 0$ we correlate identical absorption events, whereas for $\tau \neq 0$, we always correlate different events. In his proper derivation, he introduces a detector "shutter time" $\tau_d$ during which he counts photon arrivals. The correlation then has different results for $\tau < \tau_d$ and $\tau > \tau_d$. In the limit of a fast detector ($\tau_d \to 0$) he arrives at Eqs. (5.16).

*We therefore implicitly assumed $\tau > 0$ here.

In the optomechanics community, an alternative way to express $\langle i(t)\rangle$ and $G_{ii}(\tau)$ as a function of $\hat{a}(t)$ is often used [91, 93–95, 108]. There, the authors replace the quantum-mechanical correlators by their *symmetrized* version. The photocurrent autocorrelation function is then $\bar{G}_{ii}(\tau) = [G_{\hat{i}\hat{i}}(\tau) + G_{\hat{i}\hat{i}}(-\tau)]/2$. In this chapter, we follow the above described theory by Glauber and rely on normal ordering of operators. In App. E.1, we then repeat the analysis using symmetrized correlators. In Sec. 5.5, we comment on different interpretations that arise due to the different detector models.

## 5.4 Heterodyne interferometry

We now consider the common case of heterodyne detection of a weak signal $\hat{b}(t)$. For this, $\hat{b}(t)$ is mixed on a beamsplitter with a strong, coherent local-oscillator (LO) field $\hat{\alpha}(t)$, as sketched in Fig. 5.2. For the LO we have $\hat{\alpha}(t)\,|\psi\rangle = \alpha \mathrm{e}^{\mathrm{i}\omega_{\mathrm{LO}}t}\,|\psi\rangle$, where $|\psi\rangle$ is the quantum state of the LO field. All light-field operators in this chapter are in a rotating frame at the optical frequency $\omega_{\mathrm{L}}$, that is, they have an additional phase factor $\mathrm{e}^{-\mathrm{i}\omega_{\mathrm{L}}t}$ in the lab frame. For $\omega_{\mathrm{LO}} = 0$ we speak of homodyne detection, and for $\omega_{\mathrm{LO}} \neq 0$ we speak of heterodyne detection. In our definition of time $t$, a red-shifted LO beam has a positive frequency shift $\omega_{\mathrm{LO}} > 0$ and vice versa [42]. The two beamsplitter outputs are individually measured with photodetectors and the resulting photocurrents

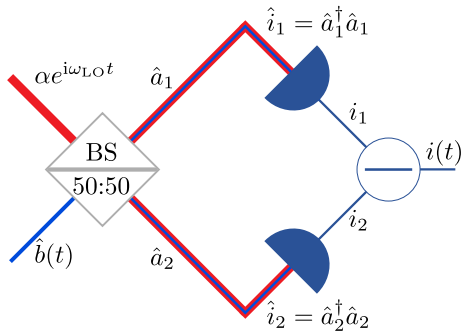


**Figure 5.2:** Heterodyne detection principle. The input $\hat{b}(t)$ is mixed with a strong local oscillator mode $\alpha$ which is detuned by $\omega_{\mathrm{LO}}$. The resulting interference is measured on a balanced photodetector.

are subtracted before amplification. Up to undetectable phase-factors, the two detected modes read

$$\begin{aligned}\hat{a}_1(t) &= \frac{\hat{b}(t) + \hat{\alpha}(t)}{\sqrt{2}},\\ \hat{a}_2(t) &= \frac{\hat{b}(t) - \hat{\alpha}(t)}{\sqrt{2}},\end{aligned} \tag{5.17}$$

where we assumed a 50:50 beamsplitter. For each mode, we can find the photon-flux operator

$$\begin{aligned}\hat{i}_1(t) = \hat{a}_1^\dagger(t)\hat{a}_1(t) &= \frac{\hat{b}^\dagger\hat{b} + \hat{\alpha}^\dagger\hat{\alpha} + \hat{b}^\dagger\hat{\alpha} + \hat{\alpha}^\dagger\hat{b}}{2},\\ \hat{i}_2(t) = \hat{a}_2^\dagger(t)\hat{a}_2(t) &= \frac{\hat{b}^\dagger\hat{b} + \hat{\alpha}^\dagger\hat{\alpha} - \hat{b}^\dagger\hat{\alpha} - \hat{\alpha}^\dagger\hat{b}}{2},\end{aligned} \tag{5.18}$$

where we omitted the time argument $t$. Next, we calculate the statistical properties of the resulting (classical) electron flux $i_{1,2}(t)$, as described in Sec. 5.3. Ultimately, we are interested in the difference current $i(t) = i_1(t) - i_2(t)$ and its correlations

$$\langle i(t)\rangle = \langle i_1(t)\rangle - \langle i_2(t)\rangle\,, \tag{5.19a}$$

$$G_{ii}(\tau) = G_{i_1i_1}(\tau) + G_{i_2i_2}(\tau) - G_{i_1i_2}(\tau) - G_{i_2i_1}(\tau), \tag{5.19b}$$

where $G_{i_1i_2}(\tau)$ and $G_{i_2i_1}(\tau)$ are the cross-correlation functions between both photocurrents. Their value is given by the normally ordered version of their quantum counterpart [101, 105]

$$G_{i_1i_2}(\tau) = \left\langle : \hat{i}_1(t+\tau)\hat{i}_2(t) : \right\rangle_t . \tag{5.20}$$

Contrary to a photocurrent autocorrelation function, this cross-correlation does not have a correction factor at $\tau = 0$. This is, because even at $\tau = 0$ the detection events are from different photons, namely those arriving at detector 1 and detector 2. Together with Eqs. (5.16), we now have all ingredients to

reexpress Eqs. (5.19) in terms of the input mode $\hat{b}(t)$:

$$\langle i(t)\rangle = \left\langle \hat{i}_1 \right\rangle_t - \left\langle \hat{i}_2 \right\rangle_t = \alpha^* \left\langle \mathrm{e}^{-\mathrm{i}\omega_{\mathrm{LO}}t} \right\rangle_t \left\langle \hat{b}(t) \right\rangle + c.c., \tag{5.21a}$$

$$\begin{aligned} G_{ii}(\tau) = |\alpha|^2 \left[\delta(\tau) + G_{\hat{b}\hat{b}}(\tau)\mathrm{e}^{\mathrm{i}\omega_{\mathrm{LO}}\tau} + G_{\hat{b}\hat{b}}(-\tau)\mathrm{e}^{-\mathrm{i}\omega_{\mathrm{LO}}\tau}\right] \\ + \left[\alpha^2 \left\langle \mathrm{e}^{\mathrm{i}\omega_{\mathrm{LO}}(2t+\tau)} \right\rangle_t G_{\hat{b}\hat{b}^\dagger}(-|\tau|) + c.c.\right]. \end{aligned} \tag{5.21b}$$

We assumed $\left\langle \hat{\alpha}^\dagger(t)\hat{\alpha}(t)\right\rangle = |\alpha|^2 \gg \left\langle \hat{b}^\dagger(t)\hat{b}(t)\right\rangle$, and $\hat{\alpha}$ and $\hat{b}$ to be independent. The derivation is detailed in App. E.2. So far we did not assume $\omega_{\mathrm{LO}} \neq 0$ and the found expression can be used for a homodyne detector, as well.

We now turn to heterodyne interferometry ($\omega_{\mathrm{LO}} \neq 0$) and find for the heterodyne photocurrent's correlations:

$$\langle i_{\mathrm{het}}(t)\rangle = 0, \tag{5.22a}$$

$$G_{ii}^{\mathrm{het}}(\tau) = |\alpha|^2 \left[\delta(\tau) + G_{\hat{b}\hat{b}}(\tau)\mathrm{e}^{\mathrm{i}\omega_{\mathrm{LO}}\tau} + G_{\hat{b}\hat{b}}(-\tau)\mathrm{e}^{-\mathrm{i}\omega_{\mathrm{LO}}\tau}\right]. \tag{5.22b}$$

The heterodyne detector current $i_{\mathrm{het}}(t)$ will therefore be zero on average and all information is in the second-order correlation $G_{ii}^{\mathrm{het}}(\tau)$. Let us calculate the corresponding photocurrent's PSD (see App. A.2 for the definition). We find

$$S_{ii}^{\mathrm{het}}(\omega) = |\alpha|^2 \left[\frac{1}{2\pi} + S_{\hat{b}\hat{b}}(\omega_{\mathrm{LO}} + \omega) + S_{\hat{b}\hat{b}}(\omega_{\mathrm{LO}} - \omega)\right]. \tag{5.23}$$

The first, constant term is associated with photon shot noise. From this expression, it is clear that $S_{ii}^{\mathrm{het}}(\omega) = S_{ii}^{\mathrm{het}}(-\omega)$. The photocurrent's spectrum is thus symmetric in frequency, just as it has to be because it is the PSD of a real-valued photocurrent. Let us look at the spectrum at a frequency $\omega_{\mathrm{LO}} + \omega$ with $|\omega| \ll \omega_{\mathrm{LO}}$. There we find

$$\begin{aligned} S_{ii}^{\mathrm{het}}(\omega_{\mathrm{LO}} + \omega) &= |\alpha|^2 \left[\frac{1}{2\pi} + S_{\hat{b}\hat{b}}(-\omega) + S_{\hat{b}\hat{b}}(2\omega_{\mathrm{LO}} + \omega)\right] \\ &\approx |\alpha|^2 \left[\frac{1}{2\pi} + S_{\hat{b}\hat{b}}(-\omega)\right]. \end{aligned} \tag{5.24}$$

Typically, the local oscillator frequency $|\omega_{\mathrm{LO}}|$ is much larger than all system frequencies, which might appear in the correlations of $\hat{b}(t)$. We therefore

approximated $S_{\hat{b}\hat{b}}(2\omega_{\mathrm{LO}}+\omega) \approx 0$ in the last expression. We observe that this type of measurement directly probes the PSD of $\hat{b}(t)$, shifted to the LO frequency. In particular, any asymmetry of $S_{\hat{b}\hat{b}}(\omega)$ around DC in its spectrum will be visible on the detector around the LO frequency.

## 5.5 Interpretation of sideband asymmetry

In Sec. 5.2, we have found expressions for the statistical properties of the optical output mode $\hat{b}_{\mathrm{out}}(t)$ of our cavity-free toy model. In Sec. 5.4, we then found an expression for the photocurrent PSD of a heterodyne detector in terms of the input mode $\hat{b}(t)$. Now, we combine both results, Eq. (5.13) and Eq. (5.24), and use $\hat{b}_{\mathrm{out}}(t)$ as an input to our heterodyne detector. We find the PSD of the detected signal at $\omega$ away from the LO frequency to be

$$S_{ii}^{\mathrm{het}}(\omega_{\mathrm{LO}}+\omega) = c_{\mathrm{het}}^2[S_{\mathrm{imp}}^{\mathrm{het}} + \overbrace{|\chi[\omega]|^2\left(S_{\hat{F}\hat{F}}^{\mathrm{th}}(-\omega)+S_{FF}^{\mathrm{ba}}\right)}^{S_{\hat{x}\hat{x}}(-\omega)}], \tag{5.25}$$

where $S_{FF}^{\mathrm{ba}} = 2\hbar^2k^2\beta^2/\pi$ is the back-action force noise, $S_{\mathrm{imp}}^{\mathrm{het}} = 1/(8\pi\beta^2k^2)$ is the measurement imprecision noise due to shot noise, and $c_{\mathrm{het}} = 2|\alpha|\beta k$ is the calibration factor of our detector.

Let us discuss Eq. (5.25), which is the central result of this chapter. In the absence of thermal noise, the imprecision-backaction product of our heterodyne detection scheme is $S_{\mathrm{imp}}^{\mathrm{het}}S_{FF}^{\mathrm{ba}} = 4\hbar^2/(4\pi)^2$. This is a factor four above the Heisenberg limit $\hbar^2/(4\pi)^2$. A factor of two can be attributed to the fact that half the time we are measuring the amplitude quadrature of the light, which does not carry any information about the mirror position $\hat{x}(t)$. In contrast, a homodyne detector always measures the light's phase quadrature. The other factor of two reflects that we distribute the signal into two sidebands, such that the effective noise bandwidth is twice as large as compared to a homodyne detector [66]. In App. E.3 we derive the imprecision noise $S_{\mathrm{imp}}^{\mathrm{hom}}$ on a homodyne detector, which is a factor four lower than $S_{\mathrm{imp}}^{\mathrm{het}}$ for the heterodyne detector, making the homodyne detector Heisenberg limited.

Further, we can see that our heterodyne detector is capable of measuring the *two-sided* and potentially asymmetric PSD $S_{\hat{x}\hat{x}}(\omega)$ of the mechanical motion.

We can choose which side to measure by choosing the sign of $\omega$ (as long as it is smaller than $\omega_{\mathrm{LO}}$).

Based on our derivation, we interpret the measured sideband asymmetry as a quantum feature of the mechanical motion. In molecular systems, where the sideband asymmetry is usually measured spectroscopically in Raman-type setups [81–83, 109, 110], this interpretation is undebated. In optomechanics, however, where the Stokes and anti-Stokes sidebands are usually resolved on a heterodyne detector, the origin of the asymmetry has been debated in literature. Some authors argue that it proves the quantum nature of the mechanics [85, 90, 111], whilst others claim that the effect is really due to the quantum nature of light [91, 93–95, 108]. As recognized by Børkje in Ref. [102], the interpretation of the asymmetry depends on the model for the heterodyne detection process. In this chapter we used *normally ordered* correlators and came to the conclusion that the asymmetry shows a quantum feature of the mechanical motion. The above mentioned references [91, 93–95, 108] on the other hand, use a *symmetrized* PSD to describe the photocurrent correlation.

In App. E.1 we repeat the above analysis with symmetrized correlators. The heterodyne photocurrent spectrum $\bar{S}_{ii}^{\mathrm{het}}$ then reads [Eq. (E.5)]

$$\bar{S}_{ii}^{\mathrm{het}}(\omega_{\mathrm{LO}}+\omega) = c_{\mathrm{het}}^2\left[S_{\mathrm{imp}}^{\mathrm{het}} + \frac{S_{\hat{x}\hat{x}}(\omega)+S_{\hat{x}\hat{x}}(-\omega)}{2} - \frac{\operatorname{Im} S_{\hat{b}^\dagger\hat{x}}^{\mathrm{in}}(\omega)}{2\beta k}\right]. \tag{5.26}$$

Clearly, the asymmetry in $S_{\hat{x}\hat{x}}(\omega)$ and therefore in $S_{\hat{F}\hat{F}}^{\mathrm{th}}(\omega)$ cannot be resolved with this detector. Instead, an additional term appears, containing a correlation between the sensing noise and the back-action noise [95]. We can evaluate it as

$$-\frac{\operatorname{Im} S_{\hat{b}^\dagger\hat{x}}^{\mathrm{in}}(\omega)}{2\beta k} = \hbar S_{\hat{b}^\dagger\hat{b}^\dagger}^{\mathrm{in}} \operatorname{Im}\chi[\omega]^* = \frac{-m\gamma\hbar\omega}{2\pi}|\chi[\omega]|^2. \tag{5.27}$$

Note, that this term is an odd function of $\omega$ and therefore asymmetric in frequency. It is this asymmetry that appears in the photocurrent's PSD. By using a *symmetrized* PSD to account for the detection, we should therefore interpret the asymmetry as an effect of the quantum nature of the input light field as it appears due shot noise $S_{\hat{b}^\dagger\hat{b}^\dagger}^{\mathrm{in}} = 1/(2\pi)$.

Finally, let us insert the expression for $S_{\hat{x}\hat{x}}(\omega)$ [Eq. (5.11)] in combination

with $S^{\text{th}}_{\hat{F}\hat{F}}(\omega)$ [Eq. (5.12)] in the photocurrent PSD $S^{\text{het}}_{ii}(\omega)$. Independent of the detector model [Eq.(5.25) or Eq.(5.26)], we find the same photocurrent PSD ($\omega > 0$):

$$\begin{aligned} S^{\text{het}}_{ii}(\omega_{\text{LO}} \pm \omega) &= c^2_{\text{het}} \left[ S^{\text{het}}_{\text{imp}} + \frac{m\gamma\hbar\omega}{\pi} |\chi[\omega]|^2 \left( n_{\text{tot}} + \frac{1}{2} \mp \frac{1}{2} \right) \right] \\ n_{\text{tot}} &= n_{\text{BE}} + 2\frac{\hbar k^2 \beta^2}{m\gamma\omega} \end{aligned} \tag{5.28}$$

We see that the oscillator's occupation number $n_{\text{tot}}$ is given by the sum of the bath occupation number $n_{\text{BE}}$ and a factor proportional to the light's intensity $\beta^2$, which can be understood as the measurement back action. We can also see that for a red-shifted LO beam, as we have assumed above, the Stokes sideband $[\propto (n_{\text{tot}} + 1)]$ appears at $\omega_{\text{LO}} - \Omega$ and the anti-Stokes sideband $[\propto n_{\text{tot}}]$ appears at $\omega_{\text{LO}} + \Omega$ on the heterodyne detector. This agrees with our observations in Ch. 4. For a blue-shifted LO beam, the sidebands exchange their positions.

## 5.6 Mapping to cavity optomechanics

Before we conclude this chapter, we map our framework to standard cavity optomechanics. For this, we rephrase the input-output relations [Eqs. (5.6)] in terms of the quadrature operators

$$\begin{aligned} \hat{Q}(t) &= \frac{1}{\sqrt{2}} \frac{\hat{x}(t)}{x_{\text{ZPF}}}, \\ \hat{P}_{\text{in}}(t) &= \frac{x_{\text{ZPF}} \hat{F}_{\text{th}}(t)}{\hbar\sqrt{\gamma}}, \\ \hat{X}_{\{\text{in,out}\}}(t) &= \frac{1}{\sqrt{2}} \left[ \hat{b}^\dagger_{\{\text{in,out}\}}(t) + \hat{b}_{\{\text{in,out}\}}(t) \right], \\ \hat{Y}_{\{\text{in,out}\}}(t) &= \frac{\mathrm{i}}{\sqrt{2}} \left[ \hat{b}^\dagger_{\{\text{in,out}\}}(t) - \hat{b}_{\{\text{in,out}\}}(t) \right], \end{aligned} \tag{5.29}$$

where we use the same definitions as Ref. [66]. We then find

$$\begin{aligned}\hat{Q}(t) &= \sqrt{2\gamma} m\Omega\chi(t) \circledast \left[\hat{P}_{\text{in}}(t) - \sqrt{2C}\hat{X}_{\text{in}}\right], \\ \hat{X}_{\text{out}}(t) &= \hat{X}_{\text{in}}(t), \\ \hat{Y}_{\text{out}}(t) &= \hat{Y}_{\text{in}}(t) - 2\sqrt{\gamma C}\hat{Q}(t),\end{aligned} \tag{5.30}$$

where

$$C = \frac{4\beta^2 k^2 x_{\text{ZPF}}^2}{\gamma}. \tag{5.31}$$

We see that Eqs. (5.30) exactly reflect the input-output relations in cavity optomechanics* and we identify $C$ as the *cooperativity* of our system. In cavity-based systems, the cooperativity is $C = 4g^2/(\gamma\kappa)$ on resonance, where $g$ is the light-enhanced optomechanical coupling rate and $\kappa$ is the cavity linewidth. Since we do not have a cavity, it is difficult to find an equivalent coupling rate, but the scaling $C \propto \{\beta^2, k^2, x_{\text{ZPF}}^2\}$ is identical to the scaling of $g^2$ for a cavity-system in each parameter. In this analogy, we replace the number of cavity-photons by the photon flux $\beta^2$.

Finally, we can extract two more parameters of our system, namely the *measurement rate*

$$\Gamma_{\text{meas}} = \gamma C = 4\beta^2 k^2 x_{\text{ZPF}}^2 \tag{5.32}$$

and the *quantum cooperativity* [12]

$$C_q = \frac{C}{\bar{n}_{\text{BE}}} = \frac{S_{FF}^{\text{ba}}}{S_{\hat{F}\hat{F}}^{\text{th}}(-\Omega)}. \tag{5.33}$$

The quantum cooperativity thus is the ratio of the mechanical heating due to photon backaction and thermal fluctuations. This result is identical to cavity optomechanics [12], and we could have used it to define the (quantum) cooperativity in the first place. We can evaluate $C_q$ for free-space levitated op-

*Note that in Ref. [66] the susceptibility is defined as $\chi_{\text{BM}}(t) = m\Omega\chi(t)$.

tomechanics by inserting the respective force PSDs [Eq. (5.12) and Eqs. (3.4)]:

$$C_q = \frac{1}{5}\begin{pmatrix}1\\2\\2+5A^2\end{pmatrix}\frac{P_{\text{dip}}}{2c^2 m\gamma n_{\text{BE}}} \approx \frac{1}{5}\begin{pmatrix}1\\2\\2+5A^2\end{pmatrix}\frac{\hbar k P_{\text{dip}}}{2cm\gamma k_B T_b}. \tag{5.34}$$

Here, we assumed a bath temperature $T_b \gg \hbar\omega/k_B$. The elements of the vector represent the three motional directions $x, y, z$ of the particle in its trap (see Ch. 3).

Let us put the found expressions into context of feedback cooling. In Ch. 2 we showed that with linear feedback, we can cool the oscillator's motion to an occupation number that is solely given by the *measurement efficiency* $\eta$, which describes how close the system is to the Heisenberg limit of the imprecision-backaction product. For a homodyne detector with detection efficiency $\eta_d$, we find in App. E.4 $S_{\text{imp}}^{\text{hom},\eta_d} = 1/(32\pi\beta^2 k^2 \eta_d)$. From the discussion in Sec. 5.5, we know that the total force noise $S_{FF}^{\text{tot}} = S_{FF}^{\text{th}} + S_{FF}^{\text{ba}}$ has a thermal contribution ($S_{FF}^{\text{th}}$) and a measurement-backaction contribution ($S_{FF}^{\text{ba}}$). We therefore find the overall measurement efficiency of our homodyne detector [29]

$$\eta = \frac{\hbar^2/(4\pi)^2}{S_{\text{imp}}^{\text{hom},\eta_d} S_{FF}^{\text{tot}}} = \frac{\hbar^2/(4\pi)^2}{S_{\text{imp}}^{\text{hom},\eta_d} S_{FF}^{\text{ba}}\,(1+1/C_q)} = \frac{\eta_d}{1+1/C_q}. \tag{5.35}$$

To achieve quantum control ($\eta \to 1$), we have to maximize both the detection efficiency and the quantum cooperativity. In Ch. 3 we discussed how to achieve a large detection efficiency $\eta_d$ in our cavity-free setup. On the other hand, we can maximize $C_q$ by reducing the bath temperature $T_b$ (for example in a cryostat) or by minimizing the coupling $\gamma$ to the bath via the pressure. Other parameters that can be tuned in the laboratory are the trap laser power $P_{\text{trap}}$, the radius $R$ of the sphere, and the wavelength $\lambda$ of the light. The scattered dipole power scales as $P_{\text{dip}} \propto R^6 P_{\text{trap}}/\lambda^4$ [42] and the intrinsic gas damping rate as $\gamma \propto 1/R^2$ [18]. The quantum cooperativity hence scales as $C_q \propto P_{\text{trap}}(R/\lambda)^5$ and can be increased linearly in the trap power. Interestingly, it scales with fifth power of the ratio $R/\lambda$, which suggests to use large particles. Note, however, that for this derivation we assumed a dipolar scatterer, which fails when $R$ approaches $\lambda$.

## 5.7 Conclusions

We developed a framework to compute the classical signals on a heterodyne detector in free-space optomechanics. We found equations of motion of the light and mechanical degrees of freedom in analogy to the canonical cavity-optomechanics framework. By comparing to the canonical framework, we could extract quantities like the quantum cooperativity and the measurement rate, which can be directly compared to other systems. We analyzed the mechanism by which the intrinsic sideband asymmetry, arising from zero-point fluctuations, appears in the heterodyne spectrum. We concluded that it can be traced back to the mechanical ZPF, if the heterodyne detector is modeled by normally ordered correlators. If, on the other hand, the detector is modeled with symmetrized correlators, we traced back the asymmetry to the light's ZPF. This result is in accordance with the findings of Børkje [102]. For the future, it would be intriguing to find an experiment that would clearly differentiate the two detector models. It might, however, turn out that both models always predict the same result.

We think that the framework provided in this chapter, might be valuable for the levitated optomechanics community for experiments that strive to achieve quantum control over the levitated object in free space.

# 6

# Conclusions and outlook

Can an object be in two locations at once? This might be one of the oldest questions in the context of quantum mechanics, which stimulated Erwin Schrödinger to come up with his famous *Gedankenexperiment* where a cat is both alive and dead simultaneously [112]. While this thesis does not address this question directly, it might serve as a stepping stone to prepare a macroscopic *cat* state of a levitated nanoparticle in the future as proposed in Refs. [25, 113, 114]. Almost all observations in this thesis, and in fact in the whole of levitated optomechanics so far, can be explained purely classically. In phase space of position and velocity, the particle is therefore well located at a single point. Before we return to the introductory question, let us recap the contents of this thesis with a focus on the "quantum ingredients" at each step.

In chapter 2 we analyzed, both theoretically and experimentally, a linear feedback cooling technique of our levitated nanoparticle. We assumed all classical equations of motion and showed that we can cool the motional energy to

$$E_{\mathrm{FB}} = 2\pi\Omega\sqrt{S_{ff}S_{\mathrm{imp}}}, \tag{6.1}$$

where $\Omega$ is the particle's oscillation frequency. This minimal oscillation energy was given by the product of the detection (imprecision) noise $S_{\mathrm{imp}}$ and the

force noise $S_{ff}$ acting on the particle. By applying Heisenberg's uncertainty principle, which can be phrased as $S_{\mathrm{imp}}S_{ff} \geq [\hbar/(4\pi)]^2$ [59], we found that under optimal Heisenberg-limited detection we would have been able to cool to the oscillator's ground-state energy $E_{\mathrm{FB}} = \hbar\Omega/2$. Assuming that this is indeed the lowest possible energy, we hence concluded that our linear feedback technique is as good as permitted by (quantum) physics.

However, the imprecision-backaction product $S_{\mathrm{imp}}S_{ff}$ was still a factor 1000 above the Heisenberg limit at this stage and we were still far in the classical regime. In chapter 3 we analyzed our optical detection principle of the scattering particle theoretically. We assumed classical light fields, which fluctuate to account for photon shot noise. Based on this, we calculated both the imprecision noise $S_{\mathrm{imp}}$ of a position detector as well as the force (back action) noise $S_{ff}^{\mathrm{ba}}$ acting on the scatterer due to photon recoil. We found an ideal detection scheme, which in principle resolves the position along all three directions at the Heisenberg limit $S_{\mathrm{imp}}S_{ff}^{\mathrm{ba}} = [\hbar/(4\pi)]^2$, but which demands exotic beam shapes that are usually not available in the laboratory. We then returned to a more realistic setting, where we used Gaussian beams only, and computed the expected detection efficiency as a function of the numerical aperture of the optics generating the trap. We found that the detection efficiency, which describes how close the detector imprecision is to the fundamental noise level, depends strongly on the direction of motion. The longitudinal $z$ motion can be resolved in a backscattering scheme with an appreciably high detection efficiency above $0.6$. This should suffice for feedback cooling of the $z$ motion to below one phonon in the future.

In chapter 4 we applied this knowledge and changed the setup accordingly. This allowed us to cool the $z$ motion to about four quanta. Moreover, in a heterodyne interference measurement we were able to resolve the asymmetry between Stokes and anti-Stokes scattering, which served as an energy measurement calibrated against the quantum of motional energy $\hbar\Omega_z$. Although the exact origin of this effect is debated in literature, a purely classical theory would not predict this effect [102]. In chapter 5 we provided a theoretical framework of optomechanics without a cavity and explored the debate about the origin of the sideband asymmetry. We concluded that depending on the model for the photodetector the interpretation of the origin differs slightly.

Let us return to the initial question of whether an object can be in two places at once. In our experience, particles have one single location at all times and therefore the answer is no. But in the realm of quantum mechanics, the position of any particle is described by a wavefunction, which is a measure of the probability of finding a particle at a certain position. A conceivable wavefunction of a single particle is a *cat* state, which has two distinct maxima separated by a large distance in space. In this situation, the particle could be found at any of the two locations (maxima) with a certain probability. Importantly, we cannot interpret this situation as the particle being either in one or the other location. This is because the wavefunction can interfere with itself at a later time, just like a classical wave would, and the resulting interference pattern would not be present if the particle were described by a single location at all times. This effect, which is demonstrated in Youngs' double-slit experiment, is in stark contradiction with our daily experience. It has nonetheless been observed experimentally with systems of ever-growing masses ranging from (mass-less) photons over electrons ($10^{-30}\,\mathrm{kg}$) to protons ($10^{-27}\,\mathrm{kg}$) and even $C_{60}$ molecules ($10^{-24}\,\mathrm{kg}$) [115].

Optically levitated nanoparticles with masses exceeding $10^{-18}\,\mathrm{kg}$ have been proposed as prime candidates to further push the scales at which quantum mechanics can be tested by creating macroscopic superposition states [25, 113, 114]. The proposed experimental protocols are as follows. First, a nanoparticle is confined in an optical trap before the trapping light is switched off. This lets the particle freely fall and its wavefunction to grow larger than the particle's dimension. A short interaction with light realizes an effective double-slit experiment which leaves the particle in a *cat* state. After another short time of free fall, the two parts of the wavefunction interfere with each other and a final position measurement will feature an interference pattern. What makes levitated nanoparticles promising candidates for testing quantum mechanics at macroscopic scales is their "unclampedness". In particular, by simply switching off the trap beam, the particle's wavefunction expands in free space to a size comparable to the particle dimension or the wavelength. In mechanically clamped systems on the other hand, such a largely extended state would require a high potential energy to be put into the system, which represents a source of decoherence. Recent advances in the field of levitated particles, especially

in free-fall experiments [116], in combination with optical cavities [30–36], and in combination with electric Paul traps [31, 117–120] make such proposals appear feasible in future experiments.

The final result in such experiments, *i.e.*, the interference pattern, can only be observed by averaging many experimental trials. This, however, requires the system's quantum state to be as *pure* as possible, where purity essentially means that the wavefunction is identical every time the experiment is repeated. The purity of a thermal state of a harmonic oscillator with mean occupation $\bar{n}$ is $1/(2\bar{n}+1)$ [121]. The only thermal state with a purity of $1$ is the ground state with $\bar{n}=0$. In this thesis, we therefore showed that under linear feedback with measurement efficiency $\eta$, we can achieve a purity of $\sqrt{\eta}$.

Within this intriguing quest of generating macroscopic superposition states, in this thesis we have focused on the state initialization. We provided a road map to purify the state of an optically levitated nanoparticle in space. Experimentally, we realized a mean occupation number $\bar{n}=4$ and therefore a purity of about $0.1$. By further reducing the gas interaction, for example in a cryogentic environment, we expect to reach a purity of above $0.5$ in future experiments.

With potentially many imponderables ahead, we are slowly but surely moving toward realizing a Schrödinger cat state with our particle.

# A

# Mathematical tools

## A.1 Fourier transform

Throughout this thesis, we use the following definition of the Fourier transform of a time-dependent function $f(t)$:

$$f[\omega] = \mathcal{F}\{f\}(\omega) := \int \mathrm{d}t\; f(t)\mathrm{e}^{\mathrm{i}\omega t}. \tag{A.1}$$

Whenever integrals are shown without boundaries, they are implicitly assumed to be $-\infty$ and $\infty$. The first two time derivatives are Fourier transformed in the following way:

$$\mathcal{F}\left\{\dot{f}\right\}(\omega) = \int \mathrm{d}t\; \dot{f}(t)\mathrm{e}^{\mathrm{i}\omega t} = -\mathrm{i}\omega f[\omega], \tag{A.2a}$$

$$\mathcal{F}\left\{\ddot{f}\right\}(\omega) = \int \mathrm{d}t\; \ddot{f}(t)\mathrm{e}^{\mathrm{i}\omega t} = -\omega^2 f[\omega]. \tag{A.2b}$$

The harmonic oscillator equation for $\gamma, \Omega > 0$ is therefore transformed as

$$\mathcal{F}\left\{\ddot{f} + \gamma\dot{f} + \Omega^2 f\right\}(\omega) = \left(\Omega^2 - \omega^2 - \mathrm{i}\gamma\omega\right) f[\omega]. \tag{A.3}$$

A time delay $\tau$ turns into a phase in frequency space as

$$\mathcal{F}\left\{f(t-\tau)\right\}(\omega) = \int \mathrm{d}t\ f(t-\tau)\mathrm{e}^{\mathrm{i}\omega t} = \mathrm{e}^{\mathrm{i}\omega\tau} f[\omega]. \tag{A.4}$$

## A.2 Correlation functions and spectral densities

Throughout this work, we use the following definition of the cross-correlation function of time-dependent operators $\hat{a}(t)$ and $\hat{b}(t)$:

$$G_{\hat{a}\hat{b}}(\tau) = \left\langle \hat{a}^\dagger(t+\tau)\hat{b}(t)\right\rangle_t. \tag{A.5}$$

The brakets $\langle\cdot\rangle$ represent the expected value operator and the subscript $\cdot_t$ refers to time averaging. For stationary and ergodic processes, the result is bound and only depends on $\tau$. The cross-spectral density $S_{\hat{a}\hat{b}}(\omega)$is then defined as $1/(2\pi)$ times the Fourier transform of $G_{\hat{a}\hat{b}}(\tau)$ according to

$$S_{\hat{a}\hat{b}}(\omega) = \frac{1}{2\pi}\int \mathrm{d}\tau\ \mathrm{e}^{\mathrm{i}\omega\tau} G_{\hat{a}\hat{b}}(\tau). \tag{A.6}$$

In the following, we list a few important symmetry relations:

$$G_{\hat{a}\hat{b}}(-\tau) = \left\langle \hat{a}^\dagger(t)\hat{b}(t+\tau)\right\rangle_t = \left\langle \hat{b}^\dagger(t+\tau)\hat{a}(t)\right\rangle_t^* = G_{\hat{b}\hat{a}}(\tau)^*, \tag{A.7a}$$

$$S_{\hat{a}\hat{b}}(\omega)^* = \int \frac{\mathrm{d}\tau}{2\pi}\ \mathrm{e}^{-\mathrm{i}\omega\tau} G_{\hat{a}\hat{b}}(\tau)^* = \int \frac{\mathrm{d}\tau}{2\pi}\ \mathrm{e}^{\mathrm{i}\omega\tau} G_{\hat{b}\hat{a}}(\tau) = S_{\hat{b}\hat{a}}(\omega). \tag{A.7b}$$

The autocorrelation function $G_{\hat{a}\hat{a}}(\tau)$ and the power spectral density (PSD) $S_{\hat{a}\hat{a}}(\omega)$ of $\hat{a}(t)$ are special cases of the cross-correlation function and the cross-spectral density, repsectively. We find

$$G_{\hat{a}\hat{a}}(-\tau)^* = G_{\hat{a}\hat{a}}(\tau), \tag{A.8a}$$

$$S_{\hat{a}\hat{a}}(\omega)^* = S_{\hat{a}\hat{a}}(\omega) \in \mathbb{R}. \tag{A.8b}$$

All above identities apply equally for classical random processes. For the special, but important case of a real-valued random process $i(t)$, we have

$G_{ii}(\tau) \in \mathbb{R}$ and hence

$$G_{ii}(-\tau) = G_{ii}(\tau), \tag{A.9a}$$

$$S_{ii}(-\omega) = \frac{1}{2\pi}\int \mathrm{d}\tau\, \mathrm{e}^{-\mathrm{i}\omega\tau} G_{ii}(\tau) = \frac{1}{2\pi}\int \mathrm{d}\tau\, \mathrm{e}^{\mathrm{i}\omega\tau} G_{ii}(-\tau) = S_{ii}(\omega). \tag{A.9b}$$

The PSD of a real-valued classical random process is therefore symmetric in frequency, while the PSD of an operator can be asymmetric in frequency. In all theoretical derivations throughout this work, we use the above defined spectral densities, which are *two-sided* and depend on angular frequency $\omega$. When we measure real time traces in experiments, we state *one-sided* PSDs, which depends on real frequency $f > 0$, as

$$\tilde{S}_{ii}(f) = 2\int \mathrm{d}\tau\, \mathrm{e}^{2\pi\mathrm{i}f\tau} G_{ii}(\tau) = 4\pi S_{ii}(2\pi f). \tag{A.10}$$

When a measured time trace is processed, $\tilde{S}_{ii}(f)$ is usually estimated by the averaged absolute squared value of the fast Fourier transform of the measurement record, as explained in Ref. [44].

## A.3 Parseval's theorem

For a real, random process $i(t)$ with PSD $S_{ii}(\omega)$, the variance of the process can be calculated as the integral over the PSD:

$$\begin{aligned}\int \mathrm{d}\omega\, S_{ii}(\omega) &= \frac{1}{2\pi}\int \mathrm{d}\omega \int \mathrm{d}\tau\, \mathrm{e}^{\mathrm{i}\omega\tau} G_{ii}(\tau) \\ &= \frac{1}{2\pi}\int \mathrm{d}\tau\, G_{ii}(\tau)\int \mathrm{d}\omega\, \mathrm{e}^{\mathrm{i}\omega\tau} \\ &= \int \mathrm{d}\tau\, G_{ii}(\tau)\delta(\tau) = \left\langle i(t)^2 \right\rangle .\end{aligned} \tag{A.11}$$

Here, we used $\int \mathrm{d}\omega\, \mathrm{e}^{\mathrm{i}\omega\tau} = 2\pi\delta(\tau)$, where $\delta(\tau)$ is Dirac's delta function. Eq. (A.11) is known as Parseval's theorem and for the single-sided PSD $\tilde{S}_{ii}(f)$

it reads

$$\int_0^\infty \mathrm{d}f\ \tilde{S}_{ii}(f) = 4\pi \int_0^\infty \mathrm{d}f\ S_{ii}(2\pi f) = \int_{-\infty}^\infty \mathrm{d}\omega\ S_{ii}(\omega) = \left\langle i(t)^2 \right\rangle, \tag{A.12}$$

where we used $S_{ii}(\omega) = S_{ii}(-\omega)$.

## A.4 Cross-correlation and convolution

For two time dependent operators $\hat{A}(t)$ and $\hat{B}(t)$ and a function $f(t)$, we have the following relationships:

$$\begin{aligned} S_{\hat{A}(f\circledast\hat{B})}(\omega) &= \int \frac{\mathrm{d}\tau}{2\pi}\, \mathrm{e}^{\mathrm{i}\omega\tau} \left\langle \hat{A}^\dagger(t+\tau) \int \mathrm{d}t'\ f(t')\hat{B}(t-t') \right\rangle_{t=0} \\ &= \int \mathrm{d}t'\ f(t')\mathrm{e}^{-\mathrm{i}\omega t'} \int \frac{\mathrm{d}\tau}{2\pi}\, \mathrm{e}^{\mathrm{i}\omega(\tau+t')} \left\langle \hat{A}^\dagger(t+\tau)\hat{B}(t-t') \right\rangle_{t=0} \\ &= \int \mathrm{d}t'\ f(t')\mathrm{e}^{-\mathrm{i}\omega t'} S_{\hat{A}\hat{B}}(\omega) = f[-\omega] S_{\hat{A}\hat{B}}(\omega), \end{aligned} \tag{A.13a}$$

$$\begin{aligned} S_{(f\circledast\hat{A})\hat{B}}(\omega) &= \int \frac{\mathrm{d}\tau}{2\pi}\, \mathrm{e}^{\mathrm{i}\omega\tau} \left\langle \int \mathrm{d}t'\ f^*(t')\hat{A}^\dagger(t+\tau-t')\hat{B}(t) \right\rangle_{t=0} \\ &= \int \mathrm{d}t'\ f^*(t')\mathrm{e}^{\mathrm{i}\omega t'} \int \frac{\mathrm{d}\tau}{2\pi}\, \mathrm{e}^{\mathrm{i}\omega(\tau-t')} \left\langle \hat{A}^\dagger(t+\tau-t')\hat{B}(t) \right\rangle_{t=0} \\ &= \left( \int \mathrm{d}t'\ f(t')\mathrm{e}^{-\mathrm{i}\omega t'} \right)^* S_{\hat{A}\hat{B}}(\omega) = f[-\omega]^* S_{\hat{A}\hat{B}}(\omega). \end{aligned} \tag{A.13b}$$

## A.5 Integral of Lorentzian functions

A reoccurring task in this thesis is to find integrals over the PSD of harmonic signals in order to find the associated energy. This involves integrals of the Lorentzian function, which we show in this section to be

$$\int \mathrm{d}\omega\ |\chi[\omega]|^2 = \int \mathrm{d}\omega\ \frac{1}{(\Omega^2-\omega^2)^2+\gamma^2\omega^2} = \frac{\pi}{\gamma\Omega^2}, \tag{A.14}$$

where

$$\chi[\omega] = \frac{1}{\Omega^2 - \omega^2 - \mathrm{i}\gamma\omega} \tag{A.15}$$

is the susceptibility of a harmonic oscillator with mass $m = 1$ [compare Eq. (5.7)]. To calculate the integral, we use Parseval's theorem [Eq. (A.11)] and solve it in time space, which requires us to know $\chi(t)$. Let us look at the following Fourier integral for $\omega_0,\ \gamma > 0$:

$$\begin{aligned}\int_0^\infty \mathrm{d}t\ \mathrm{e}^{-\frac{\gamma t}{2}} \sin(\omega_0 t)\mathrm{e}^{\mathrm{i}\omega t} &= \frac{1}{2\mathrm{i}} \int_0^\infty \mathrm{d}t\ \mathrm{e}^{-\frac{\gamma t}{2}} \left(\mathrm{e}^{\mathrm{i}(\omega+\omega_0)t} - \mathrm{e}^{\mathrm{i}(\omega-\omega_0)t}\right) \\ &= \frac{\omega_0}{\gamma^2/4 + \omega_0^2 - \omega^2 - \mathrm{i}\gamma\omega}.\end{aligned} \tag{A.16}$$

We can therefore conclude

$$\chi(t) = \Theta(t)\frac{1}{\omega_0}\mathrm{e}^{-\frac{\gamma t}{2}} \sin(\omega_0 t), \tag{A.17}$$

where we substituted $\omega_0 = \sqrt{\Omega^2 - \gamma^2/4}$ and where $\Theta(t)$ is the Heaviside step function. Note, that the found expression for $\chi(t)$ is true even if $\Omega < \gamma/2$, in which case $\omega_0$ becomes imaginary. Since we then have $\gamma/2 > \sqrt{\gamma^2/4 - \Omega^2} = |\omega_0|$, the integral in Eq. (A.16) still converges.
Now we can compute the integral in Eq. (A.14):

$$\begin{aligned}\int \mathrm{d}\omega\ |\chi[\omega]|^2 &= \int \mathrm{d}\omega\ \left[\int \mathrm{d}t\ \chi[t]\mathrm{e}^{\mathrm{i}\omega t}\right]^* \int \mathrm{d}t'\ \chi[t']\mathrm{e}^{\mathrm{i}\omega t'} \\ &= 2\pi \int \mathrm{d}t\ \int \mathrm{d}t'\ \chi[t]^*\chi[t']\delta(t'-t) \\ &= 2\pi \int \mathrm{d}t\ |\chi[t]|^2 = 2\pi \int_0^\infty \mathrm{d}t\ \frac{1}{\omega_0^2}\mathrm{e}^{-\gamma t} \sin(\omega_0 t)^2 \\ &= \frac{\pi}{\gamma}\frac{4}{\gamma^2 + 4\omega_0^2} = \frac{\pi}{\gamma\Omega^2}.\end{aligned} \tag{A.18}$$

When integrating the PSD of the velocity of a harmonic oscillator, we come across the following integral:

$$\begin{aligned}\int \mathrm{d}\omega \, \frac{\omega^2}{(\Omega^2-\omega^2)^2+\gamma^2\omega^2} &= \int \mathrm{d}\omega \, \left|-\mathrm{i}\omega\chi[\omega]\right|^2 = 2\pi \int \mathrm{d}t \, \left|\frac{\mathrm{d}}{\mathrm{d}t}\chi[t]\right|^2 \\ &= 2\pi \int_0^\infty \mathrm{d}t \, \frac{1}{\omega_0^2}\mathrm{e}^{-\gamma t}\left[-\frac{\gamma}{2}\sin(\omega_0 t)+\omega_0\cos(\omega_0 t)\right]^2 = \frac{\pi}{\gamma}.\end{aligned} \tag{A.19}$$

## A.6 Power spectral density of shot noise

This section is about the PSD of shot noise. It is not meant as a rigorous proof, which can be found elsewhere [75, 104]. We know from quantum theory that for a coherent state, the number of excitations is Poisson distributed. Let us assume a shot-noise limited beam of average photon flux $\bar{i}$, which impinges on an ideal photon counter. The flux $i(t)$ of detection events is a random process with mean $\langle i(t)\rangle = \bar{i}$. Its fluctuations $\delta i(t) = i(t) - \bar{i}$ is a zero-mean process, which is uncorrelated in time. The autocorrelation function is therefore [104]

$$G_{\delta i \delta i}(\tau) = \langle \delta i(t+\tau)\delta i(t)\rangle = \bar{i}\delta(\tau). \tag{A.20}$$

We can verify this result by calculating the statistical properties of the number $N(t) = \int_0^t \mathrm{d}t' \, i(t')$ of clicks on the detector in the time interval $[0,t]$. First, we subtract the mean $\langle N(t)\rangle = \bar{i}t$ from $N(t)$ to find the fluctuations $\delta N(t) = N(t) - \bar{i}t = \int_0^t \mathrm{d}t' \, \delta i(t')$. Now we can find the variance of $N(t)$, which is

$$\begin{aligned}\mathrm{Var}[N(t)] = \left\langle \delta N(t)^2 \right\rangle &= \int_0^t \mathrm{d}t' \int_0^t \mathrm{d}t'' \, \left\langle \delta i(t')\delta i(t'')\right\rangle \\ &= \bar{i}\int_0^t \mathrm{d}t' \int_0^t \mathrm{d}t'' \, \delta(t'-t'') = \bar{i}t = \langle N(t)\rangle \,.\end{aligned} \tag{A.21}$$

This result verifies that the variance of $N(t)$ equals the mean of $N(t)$, which is an essential property of a Poisson distribution. From the autocorrelation

$G_{\delta i \delta i}(\tau)$, we can find the two-sided PSD of the flux fluctuations as

$$S_{\delta i \delta i}(\omega) = \frac{\bar{i}}{2\pi}. \tag{A.22}$$

Experimentally, we usually measure the photon flux as an optical power $P(t) = \hbar\omega_\mathrm{L} i(t)$, where $\omega_\mathrm{L}$ is the laser frequency. The two- and single-sided PSDs of the power fluctuations are then

$$S_{PP}(\omega) = \frac{\hbar^2\omega_\mathrm{L}^2\bar{i}}{2\pi} = \frac{\hbar\omega_\mathrm{L}\bar{P}}{2\pi}, \tag{A.23a}$$

$$\tilde{S}_{PP}(f) = 2\hbar\omega_\mathrm{L}\bar{P}, \tag{A.23b}$$

where $\bar{P} = \hbar\omega_\mathrm{L}\bar{i}$ is the average power.
Let us exchange photons for electrons and look at the shot noise of an electric current $I(t) = qi(t)$ with average current $\bar{I} = q\bar{i}$ and elementary charge $q$. The two- and single-sided PSDs of the current fluctuations read [75]

$$\begin{aligned} S_{II}(\omega) &= \frac{q^2\bar{i}}{2\pi} = \frac{q\bar{I}}{2\pi}, \\ \tilde{S}_{II}(f) &= 2q\bar{I}. \end{aligned} \tag{A.24}$$

Let us finally assume a photodetector with quantum efficiency $\eta_Q < 1$. This detector converts an optical power $\bar{P}$ into a photocurrent $\bar{I}_\mathrm{phot} = \mathcal{R}\bar{P}$, where $\mathcal{R} = \eta_Q q/(\hbar\omega_\mathrm{L})$ is the detector's responsivity. The detector can be modeled as an ideal photodetector with unity quantum efficiency and a beamsplitter with transmission coefficient $\eta_Q$ in front of the optical input. The input power to the ideal photodetector is then $\bar{P}_\mathrm{id} = \eta_Q\bar{P}$. This power fluctuates due to shot-noise with PSD $S^\mathrm{id}_{PP}(\omega) = \hbar\omega_\mathrm{L}\eta_Q\bar{P}/(2\pi)$. Equivalently, the photocurrent PSD is

$$S^\mathrm{phot}_{II}(\omega) = \left(\frac{q}{\hbar\omega_\mathrm{L}}\right)^2 S^\mathrm{id}_{PP}(\omega) = \frac{q\bar{I}_\mathrm{phot}}{2\pi}. \tag{A.25}$$

We see that in a shot-noise limited detection scheme, the photocurrent fluctuations are exactly given by the current shot noise due to the mean photocurrent $\bar{I}_\mathrm{phot}$. If we interpret the photocurrent $\bar{I}_\mathrm{phot}$ as a measure for the optical power $\bar{P} = \bar{I}_\mathrm{phot}/\mathcal{R}$, then we find that the PSD of the imprecision of this power

measurement is $S_{II}^{\text{phot}}(\omega)/\mathcal{R}^2 = \hbar\omega_{\text{L}}\bar{P}/(2\pi\eta_Q) = S_{PP}(\omega)/\eta_Q$. Only in the limit of unity quantum efficiency, this is equal to the optical shot noise $S_{PP}(\omega)$ [Eq. (A.23a)] due to input power $\bar{P}$. In other words, the measurement noise increases as the detector quantum efficiency decreases. In App. C.8 we describe how to measure shot noise on a photodetector experimentally.

# B

# Equipartition under linear feedback cooling

In this appendix we analyze our measurement based feedback from chapter 2. We note that in general, a harmonic oscillator under linear feedback breaks the equipartition theorem [29, 60, 61], a fact that we became aware of after writing the papers [58] and [122]. In these papers, which form the basis of Ch. 2 and Ch. 4, the feedback damping rate is much smaller than the eigenfrequency of the system. Here we show that in that limit, where the system is underdamped even under feedback, the equipartition theorem still holds.

Let us revisit the equation of motion of a harmonic oscillator $x$ with eigenfrequency $\Omega$ and mass $m$ under a linear feedback. In frequency space, it reads [compare Eq. (2.1)]

$$x[\omega] = \tilde{\chi}_{\mathrm{FB}}[\omega]\left(\frac{f_{\mathrm{fluct}}[\omega]}{m\Omega^2} + h_{\mathrm{FB}}[\omega]x_{\mathrm{imp}}[\omega]\right) \tag{B.1}$$

with the (unitless) mechanical susceptibility under feedback

$$\tilde{\chi}_{\mathrm{FB}}[\omega] = \frac{1}{1 - \frac{\omega^2}{\Omega^2} - \mathrm{i}\frac{\gamma_0\omega}{\Omega^2} - h_{\mathrm{FB}}[\omega]}. \tag{B.2}$$

Here, $\gamma_0$ is the natural damping rate, $f_{\text{fluct}}$ is a fluctuating force driving the oscillator, and $x_{\text{imp}}$ is the imprecision noise on the in-loop detector. The feedback filter function $h_{\text{FB}}[\omega]$ is normalized to be unitless. In analogy to the analysis in Ch. 2, we calculate the position power spectral density (PSD)

$$S_{xx}(\omega) = |\tilde{\chi}_{\text{FB}}[\omega]|^2 \left( \frac{S_{ff}}{m^2\Omega^4} + |h_{\text{FB}}[\omega]|^2 S_{\text{imp}} \right), \tag{B.3}$$

where we assume $f_{\text{fluct}}$ and $x_{\text{imp}}$ to be white noise processes with constant PSDs $S_{ff}$ and $S_{\text{imp}}$, and to be statistically independent. For the following discussion, it is useful to replace $S_{ff}$ and $S_{\text{imp}}$ by two new parameters, the *measurement efficiency*

$$\eta = \frac{\hbar^2}{(4\pi)^2} \frac{1}{S_{ff} S_{\text{imp}}} \tag{B.4}$$

and

$$\gamma^x_{\text{opt}} = \frac{1}{m\Omega} \sqrt{\frac{S_{ff}}{S_{\text{imp}}}}. \tag{B.5}$$

Heisenberg's uncertainty relation demands that $\eta \leq 1$ [59] (see discussion in Ch. 2). We will later see that $\gamma^x_{\text{opt}}$ is the feedback damping rate, which minimizes the position fluctuations for a perfect derivative filter. In terms of $\eta$ and $\gamma^x_{\text{opt}}$, we have

$$S_{xx}(\omega) = \frac{x^2_{\text{ZPF}}}{2\pi\sqrt{\eta}\Omega} |\tilde{\chi}_{\text{FB}}|^2 \left( \frac{\gamma^x_{\text{opt}}}{\Omega} + |h_{\text{FB}}|^2 \frac{\Omega}{\gamma^x_{\text{opt}}} \right), \tag{B.6a}$$

$$S_{pp}(\omega) = m^2\omega^2 S_{xx}(\omega) = \frac{p^2_{\text{ZPF}}}{2\pi\sqrt{\eta}\Omega} \frac{\omega^2}{\Omega^2} |\tilde{\chi}_{\text{FB}}|^2 \left( \frac{\gamma^x_{\text{opt}}}{\Omega} + |h_{\text{FB}}|^2 \frac{\Omega}{\gamma^x_{\text{opt}}} \right), \tag{B.6b}$$

where $S_{pp}(\omega)$ is the momentum PSD. We used the position and momentum zero-point fluctuations $x^2_{\text{ZPF}} = \hbar/(2m\Omega)$ and $p^2_{\text{ZPF}} = m\hbar\Omega/2$, respectively. The variance of the position and momentum fluctuations are then $\langle x^2 \rangle = \int \mathrm{d}\omega\, S_{xx}(\omega)$ and $\langle p^2 \rangle = \int \mathrm{d}\omega\, S_{pp}(\omega)$. The total energy of the motion under feedback is

$$E_{\text{FB}} = \frac{\hbar\Omega}{4} \left( \frac{\langle x^2 \rangle}{x^2_{\text{ZPF}}} + \frac{\langle p^2 \rangle}{p^2_{\text{ZPF}}} \right). \tag{B.7}$$

Next, we need to assume a specific filter type. Let us start with a perfect

derivative filter in analogy to the discussion in Ch. 2. That is $h_{\mathrm{FB}} = h_{\mathrm{deriv}} = \mathrm{i}\omega\gamma_{\mathrm{FB}}/\Omega^2$ with a feedback damping rate $\gamma_{\mathrm{FB}}$. Using Eqs. (A.14) and (A.19) we can analytically find the position fluctuations to be

$$\left\langle x^2 \right\rangle_{\mathrm{deriv}} = \frac{x_{\mathrm{ZPF}}^2}{2\sqrt{\eta}} \left( \frac{\gamma_{\mathrm{opt}}^x}{\gamma_{\mathrm{FB}}} + \frac{\gamma_{\mathrm{FB}}}{\gamma_{\mathrm{opt}}^x} \right). \tag{B.8}$$

Here, we assumed the feedback induced damping to largely exceed the natural damping ($\gamma_{\mathrm{FB}} \gg \gamma_0$), a condition that is usually valid. This expression is minimized by optimizing the feedback, and we see that a feedback damping rate of $\gamma_{\mathrm{FB}} = \gamma_{\mathrm{opt}}^x$ minimizes the position fluctuations. In the following discussion in Ch. 2, we assumed the equipartition theorem, according to which $\left\langle p^2 \right\rangle / p_{\mathrm{ZPF}}^2 = \left\langle x^2 \right\rangle / x_{\mathrm{ZPF}}^2$. With this assumption, the energy under feedback is $E_{\mathrm{deriv}} = \hbar\Omega/(2\sqrt{\eta})$ such that we can cool to the ground state energy $E_{\mathrm{GS}} = \hbar\Omega/2$ for unity measurement efficiency.

Importantly however, the feedback in general breaks the equipartition theorem [29, 60, 61]. In the following discussion, we will find that this effect is strong when $\gamma_{\mathrm{FB}}$ approaches $\Omega$. For a resonant system under feedback with $\gamma_{\mathrm{FB}} \ll \Omega$, however, the equipartition theorem still holds and the analysis in chapters 2 and 4 is correct.

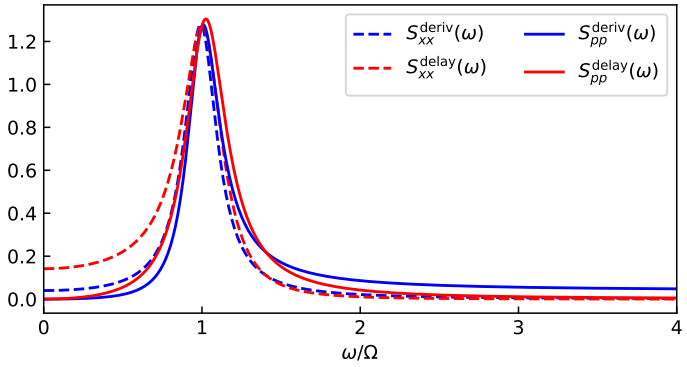


**Figure B.1:** $S_{xx}(\omega)$ (dashed) in units of $x_{\mathrm{ZPF}}^2/\Omega$ and $S_{pp}(\omega)$ (solid) in units of $p_{\mathrm{ZPF}}^2/\Omega$ according to Eqs. (B.6). The feedback filter is a perfect derivative filter in blue and a delay filter in red with parameters $\gamma_{\mathrm{opt}}^x = \gamma_{\mathrm{FB}} = \Omega/4$ and $\eta = 1$.

Let us look at the momentum PSD $S_{pp}(\omega)$ under a derivative filter. We see that for large frequencies, $S_{pp}(\omega)$ does not decay to zero since the last term in Eq. (B.6b) scales as $(\omega/\Omega)^4|\chi_{\mathrm{FB}}[\omega]|^2 \to 1$ as $\omega \to \infty$. This means that the derivative filter induces white momentum fluctuations for large frequencies such that the oscillator would have infinite kinetic energy. This is clearly unphysical and any real feedback has a certain bandwidth, which limits the energy. Also, note that this energy is fed back at large frequencies far off resonance. In Fig. B.1 we show the position and momentum PSD for a derivative filter as a blue dashed and a blue solid line, respectively. We assume a relatively large feedback damping of $\gamma_{\mathrm{FB}} = \gamma^x_{\mathrm{opt}} = \Omega/4$ here. While we can clearly see that for large frequencies $S^{\mathrm{deriv}}_{pp}$ does not decay to zero, the system is still resonant with most energy close to the resonance frequency $\Omega$.

In the following, we assume the filter bandwidth to be $4\Omega$, which limits the total kinetic energy. With this assumption, we show in Fig. B.2 the total energy under feedback $E_{\mathrm{deriv}}$ according to Eq. (B.7) as a function of the applied $\gamma_{\mathrm{FB}}$ (blue lines) and for various values of $\gamma^x_{\mathrm{opt}}$ (blue circles). For each $\gamma^x_{\mathrm{opt}}$ we numerically find an optimum feedback value $\gamma_{\mathrm{opt}}$, which minimizes the

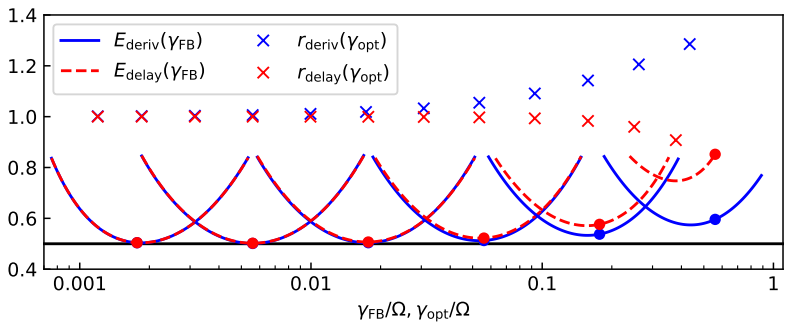


**Figure B.2:** Comparison of derivative (blue symbols) and delay filter (red symbols). We show the motional energy as a function of the feedback damping rate $\gamma_{\mathrm{FB}}$ for various values of $\gamma^x_{\mathrm{opt}} = \sqrt{S_{ff}/S_{\mathrm{imp}}}/(m\Omega)$ (solid and dashed lines). The energy is given in units of $\hbar\Omega/\sqrt{\eta}$. For each curve, the value of $\gamma^x_{\mathrm{opt}}$ is indicated as a circle. We observe that the actual optimal feedback rate $\gamma_{\mathrm{opt}}$, which minimizes the energy, is smaller than $\gamma^x_{\mathrm{opt}}$ for $\gamma^x_{\mathrm{opt}}$ approaching $\Omega$. The crosses indicate the squeezing parameter at $\gamma_{\mathrm{opt}}$. The black line indicates the theoretical limit of $\hbar\Omega/(2\sqrt{\eta})$.

energy instead of the position fluctuations. For each optimal feedback value, we compute a squeezing parameter $r$ defined as

$$r = \frac{\langle p^2 \rangle}{p_{\mathrm{ZPF}}^2} \frac{x_{\mathrm{ZPF}}^2}{\langle x^2 \rangle} \tag{B.9}$$

and show $r$ as blue crosses in Fig. B.2.

We see that in the limit of small feedback damping $\gamma_{\mathrm{opt}}^x \ll \Omega$, the optimal feedback damping rate $\gamma_{\mathrm{opt}}$ equals $\gamma_{\mathrm{opt}}^x$. In the same limit, we see that the squeezing parameter approaches unity and the energy under feedback reaches $E_{\mathrm{opt}} = \hbar\Omega/(2\sqrt{\eta})$ (black line). We interpret this result that the equipartition theorem holds in this limit, and that the filter can cool the motion to its quantum ground state for $\eta \to 1$. In the opposite limit ($\gamma_{\mathrm{opt}}^x \lessapprox \Omega$) however, the momentum fluctuations start to exceed the position fluctuations and equipartition does not hold. In that limit, the optimal feedback damping which minimizes the energy, is smaller than $\gamma_{\mathrm{opt}}^x$ and the feedback does not achieve ground-state cooling.

As detailed in App. C.5, in the lab we typically do not implement a derivative filter, but rely on a delay filter, which mimics a derivative filter on resonance by delaying the signal for a quarter of an oscillation period. The filter transfer function then reads $h_{\mathrm{FB}} = h_{\mathrm{delay}} = (\gamma_{\mathrm{FB}}/\Omega)\exp\left[\mathrm{i}\pi\omega/(2\Omega)\right]$, see Eq. (A.4). We cannot integrate the susceptibility $|\tilde{\chi}_{\mathrm{delay}}|^2$ analytically in this case, but need to rely on numerical integration. In Fig. B.1, we show the position and momentum PSD for a delay filter as a red dashed and a red solid line, respectively. Contrary to the previously discussed derivative filter, the momentum PSD for this filter does decay to zero limiting the total kinetic energy without the need of a finite filter bandwidth*. In Fig. B.2, we perform the same analysis for the delay filter in red symbols as for the derivative filter before. We note that in the small feedback damping limit ($\gamma_{\mathrm{opt}}^x \ll \Omega$) both filters behave identical without breaking the equipartition theorem and both can reach the quantum ground state. In the other limit of $\gamma_{\mathrm{opt}}^x \lessapprox \Omega$, the delay filter, too, breaks equipartition and cannot reach the ground state. In contrast to the derivative filter, however, it leads to smaller momentum than position

*This result can also be understood without numerical evaluation by noting that $|h_{\mathrm{delay}}| = \gamma_{\mathrm{FB}}/\Omega$ is independent of frequency and therefore $S_{pp}(\omega \to \infty) \to 0$.

fluctuations with $r_{\text{delay}} < 1$.

Let us put our results in the perspective of the experiments described in chapters 2 and 4, where we used a delay filter. In chapter 2 we had an oscillation frequency in the transverse $y$ direction of $150\,\text{kHz}$ and found an optimal cooling rate of about $1\,\text{kHz}$ so that $\gamma_{\text{opt}}/\Omega \approx 7 \times 10^{-3}$. In chapter 4 we feedback cooled with $\gamma_{\text{FB}} \approx 4\,\text{kHz}$ an oscillator with $\Omega = 50\,\text{kHz}$ such that $\gamma_{\text{FB}}/\Omega \approx 8 \times 10^{-2}$. From the analysis shown here, we can estimate the squeezing parameter to be $r_{\text{delay}} \approx 0.9997$ and $0.993$ in the two cases. We conclude that the equipartition theorem largely holds in both cases. The filter limit is a factor of less than $1\,\%$ and $10\,\%$ above the theoretical limit of $E_{\text{deriv}} = \hbar\Omega/(2\sqrt{\eta})$.

The derivation provided here is purely classical with the exception that we assumed a Heisenberg limit for the imprecision-backaction product. In the future, we should make a quantum analysis of the problem inspired by cavity optomechanics, which would include a stochastic master equation [61, 123–126].

# C

# Detailed experimental setup

In this appendix, we detail the experimental setup used to obtain the measurements in chapters 2 and 4. This document is addressed to experimentalists, who are building up a similar experiment. We first give an overview of the setup and then zoom into the various blocks in the following sections. Additionally, we detail how to calibrate a photodetector against shot noise in Sec. C.8.

The setup is based on the dissertation by Vijay Jain [46] and sketched in Fig. C.1. A $1064\,\mathrm{nm}$ laser * is intensity modulated by an electro-optical modu-

*Coherent Mephisto 2W

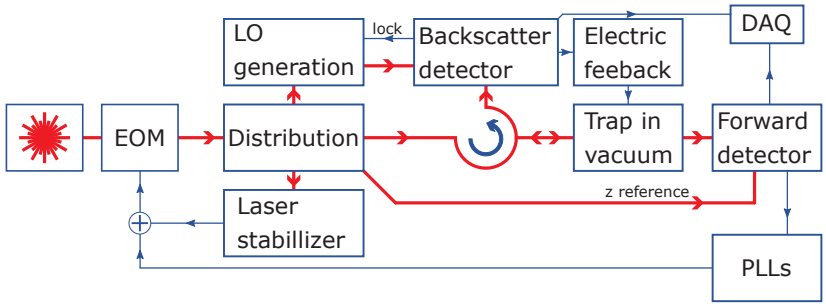


**Figure C.1:** Experimental setup overview.

lator (EOM)*. Most of the light is sent through a free-space circulator to the vacuum chamber, which contains the optical trap. The forward scattered light is sent to a split detection scheme [43, 44, 46, 69] whilst the backscattered light is collected at the third port of the circulator and sent to another interferometric detector. In forward scattering, the trap light serves as a local oscillator (LO), which does not exist in backscattering. We therefore send a fraction of the laser light to a "LO generator", which controls both phase and frequency of the LO beam. It interferes on the "backscatter detector" with the backscattered light from the particle. The electric signal from this detector is used to lock the path length difference between the particle and the LO light. The detector signal is then used to feedback-cool the center-of-mass motion of the particle electrically. In order to stabilize the particle in the trap, we use parametric feedback cooling [18, 43] based on phase-locked loops (PLLs) [41, 46]. Finally, to exclude classical noise effects in the asymmetry measurements in chapter 4, we stabilize the relative intensity noise of the laser actively by feeding back the measured intensity to the EOM. All parts of the setup are individually explained below.

## C.1 Laser distribution and stabilization

In Fig. C.2 we show how the laser is split between the various blocks of the setup. The EOM is optically biased using circular light from a quarter-wave plate (QWP) such that its response to the voltage input $V_{\mathrm{mod}}$ is maximized. This way we can avoid a large DC voltage at the EOM, which could be subject to noise. In practice, the EOM is driven by less than $10\,\mathrm{V}$ peak-to-peak without the need of a high-voltage amplifier. The EOM's output light, which is phase-modulated in one field component by the applied voltage $V_{\mathrm{mod}}$, is sent through a polarizing beamsplitter (PBS $\mathrm{P}_2$), which turns the phase modulation into an amplitude modulation. The light is then split using combinations of half-wave plates (HWPs) and PBSs ($\mathrm{P}_3$ - $\mathrm{P}_5$). The light used for trapping (about $300\,\mathrm{mW}$) and the LO light (about $50\,\mathrm{mW}$) are coupled into two polarizing-maintaining (PM) fibers. A small fraction of the light is sent in free space to the z-detector in

*Conoptics M350-210.

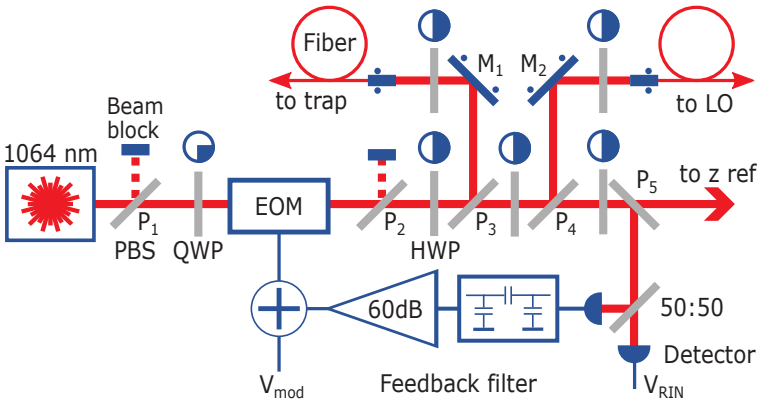


**Figure C.2:** Laser distribution and stabilizer. The components are explained in the text. The circles at the fiber collimators and mirrors $M_1$ and $M_2$ indicate degrees of freedom needed to couple the light into the fibers. The electric input $V_{\mathrm{mod}}$ is used for intensity modulation of the laser. The dashed lines at PBS outputs indicate that the PBS' input polarization is chosen such that the intensity at this output is minimized.

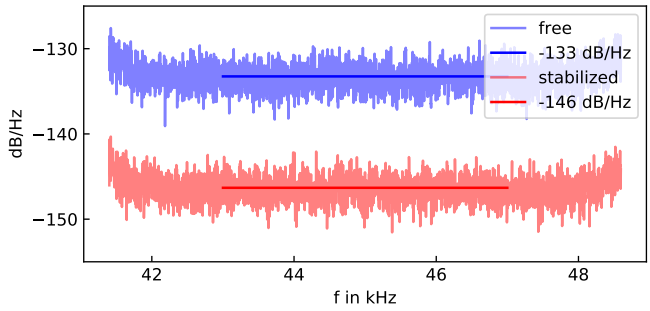


**Figure C.3:** Measured laser RIN with (light red) and without (light blue) active stabilization. The straight lines indicate the average value (see legend) including the frequency range of averaging. The single-sided spectra are measured with a lock-in amplifier and normalized by the DC value. A RIN reduction of about 13 dB is achieved. The apparent increase of the spectra at the edges is an artifact of the demodulation process. The measured photocurrent was 1.5 mA, which amounts to a shot noise contribution of $-156.7\,\mathrm{dB/Hz}$ to RIN [Compare Eq. (A.24)].

forward scattering for balancing [43]. About $2\,\mathrm{mW}$ are sent to two independent photodetectors* in order to measure the laser's relative intensity noise (RIN). The output signal of one of the detectors is band-pass filtered, amplified, and fed back to the EOM in order to reduce the RIN of the laser actively. The other detector signal $V_{\mathrm{RIN}}$ represents an out-of-loop measurement of the laser RIN, the normalized PSD of which we plot in Fig. C.3 (see caption for details). We achieve a RIN reduction of $13\,\mathrm{dB}$ at $45\,\mathrm{kHz}$.

The implemented feedback is all analog and relies on a first-order high-pass (HPF) and a first-order low-pass filter (LPF). The filters are home built and are implemented by three capacitors as indicated in Fig. C.2. The DC-blocking (center) one is a $1\,\mu\mathrm{F}$ ceramic capacitor, which leads to a cut-off frequency of the HPF of $1.6\,\mathrm{kHz}$ due to the $50\,\Omega$ resistors at the detector output and the amplifier† input. This way we make sure that we do not feed back the DC power. Importantly, the loop gain must be negative, which we ensure by biasing the EOM with circular light of the correct handedness. Since the loop has a decreasing phase with frequency (due to the respective transfer functions of the detector, the BNC cables, and the EOM), the loop gain turns positive for large enough frequency. For stable operation, the (absolute) gain must be small enough at that frequency. For this, the LPF is implemented by two $10\,\mathrm{nF}$ capacitors to ground with a cut-off frequency of about $320\,\mathrm{kHz}$. The feedback therefore reduces laser RIN in the frequency range from $1.6\,\mathrm{kHz}$ to $320\,\mathrm{kHz}$.

## C.2 Optical trap and backscatter detector

This section is devoted to the most central part of our setup, which consists of the optical trap and the backscatter detector as depicted in Fig. C.4. The trap light comes from a PM fiber and, using a HWP and the PBS $\mathrm{P}_1$, the residual polarization modulations are turned into intensity modulations. The PBS $\mathrm{P}_2$ and the following Faraday rotator (FR) form a free-space circulator, the function of which we describe below. The reflected port of $\mathrm{P}_2$ is sent to a Photodiode ($V_{\mathrm{trap}}$), which monitors the trap power in real time. The FR‡ rotates the polarization by

*Thorlabs PDA10CS and Thorlabs PDA20CS
†Femto HVA-10M-60-B with $60\,\mathrm{dB}$ gain.
‡Qioptiq LINOS FI-1060-5SC HP

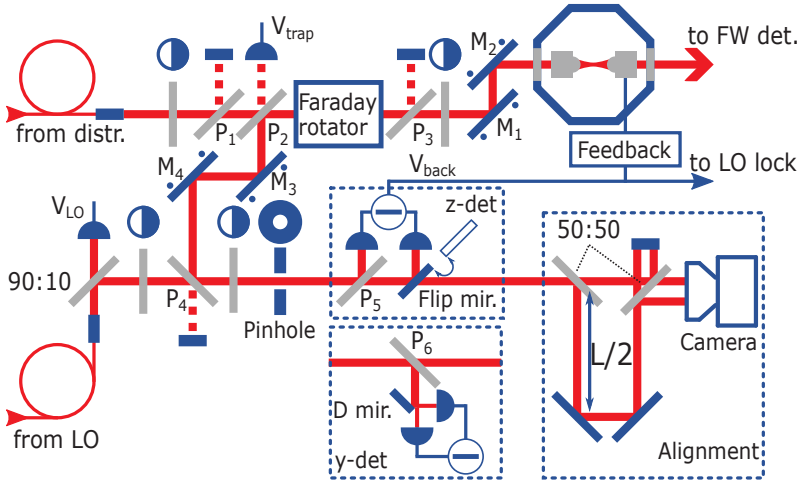


**Figure C.4:** Optical trap and backscatter detector. For chapter 2, the box labeled "y-det" replaced the box "z-det".

45° before PBS $P_3$ cleans the polarization again ($P_3$ is mounted to the FR at an angle of 45° to match the polarization axis). A HWP rotates the polarization to vertical in the lab frame before the two mirrors $M_1$ and $M_2$ steer the beam into the trap. Finally, the trap is formed using an overfilled 0.85 NA objective*. We installed an electrode close by the trap, which we can use to electrically drive the particle using the Coulomb force and to apply a damping force. Before turning to the forward scattered detection in Sec. C.4, here we concentrate on the particle light (about 10 µW) that is scattered back into the trap objective. Because the particle is trapped at the focal spot (or very close to it on the optical axis), its scattered light travels back on the same beam path as the trap light. The polarization of the scattered light is rotated by another 45° in the FR, such that it reflects out at $P_2$. This way, we split the trap beam and the backscattered beam.

In order to have an interferometric position measurement of the trapped particle, the backscattered light is combined with a local oscillator (LO) beam (about 4 mW), which comes from another PM fiber. We monitor the LO power with a photodetector ($V_{\mathrm{LO}}$ in the figure). In Ch. 4, we sketched a 50:50

*Olympus LCPLN100XIR

beamsplitter in Fig. 4.1, which combines the beams. In the lab however, we use a combination of two PBSs ($P_4$ and $P_5$) with a HWP in between. By rotating the HWP, this combination acts like a $R$:$T$ beamsplitter, where the reflection and transmission coefficients $R$ and $T$ can be tuned by the HWP angle. We tune the angle such that the following photodetector with output voltage $V_{\text{back}}$ is balanced, which means that $R \approx T \approx 1/2$. This home-built photodetector ($V_{\text{back}}$) is the central photodetector. It locks the interferometer (see Sec. C.3.1 for details on the lock) and provides us with both a homodyne readout of the particle position $z(t)$ along the optical axis and a heterodyne readout for sideband thermometry, simultaneously.

All other components that are present in Fig. C.4 have the sole purpose of aligning the two beams (the backscattered beam from the particle and the LO beam). Due to backreflections from interfaces in the beam path, there is in general a lot more reflected light than just the particle scattering. These reflections can be spatially separated by slightly tilting the interfaces from normal incidence. A pinhole is then used to block them. For overlapping both beams, a flip mirror is installed such that the beams can be sent to a camera*, where both beams are imaged individually (by blocking one of the paths). We use a combination of two 50:50 beamsplitters to generate a second (spatially separated) image on the camera at a distance $L \approx 1\,\mathrm{m}$ further down the optical path. The two mirrors $M_3$ and $M_4$ are used to beam steer the backscattered light until both beams are aligned on the camera. It turned out useful to have the scattered beam steerable rather than the LO beam, because it contains much less light and therefore the balancing of the detector does not change when the beam is steered.

For the measurements in chapter 2, where we were focusing on the transverse $y$ motion, we used a slightly different setup in backscattering (inset in Fig. C.4 labeled "y-det"). We used a D-shaped mirror to implement a split detection scheme, which is sensitive to transverse motion, at one output of $P_6$. Note that the other PBS output was not detected and in this scheme one would require a second balanced photodiode to maximize the detection efficiency.

*Point Grey Research CMLN-13S2M

### C.2.1 Calibration of backscatter detector

The purpose of the photodetectors is to measure the particle position and hence a calibration is necessary to convert from volt to meter. We calibrate the forward detectors (see Sec. C.4) in the mildly underdamped regime at a pressure of $10\,\mathrm{mbar}$ by equating the measured oscillation amplitude to a temperature of $300\,\mathrm{K}$ [56]. In backscattering however, we were not able to copy this procedure. This was because of the high detection efficiency in backsacttering, which led to a strong non-linear position detection when the particle was equilibrated to $300\,\mathrm{K}$. We therefore used a different approach and translated the calibration from the forward detectors. At a low pressure (below $10^{-5}\,\mathrm{mbar}$), we stabilized the particle with some weak parametric feedback, and applied an RF tone to the electrode close by the trap, driving the particle's oscillation coherently close to its resonance frequency. We made the tone strong enough to have a good signal-to-noise ratio in both backward and forward scattering. By equating the signal power on both detectors, we calibrated the backscatter detector (both the homodyne and heterodyne readout).

## C.3 Local oscillator generation

We use a combination of two acousto-optical modulators (AOMs), to frequency and phase control the LO beam as depicted in Fig. C.5. The light from the input

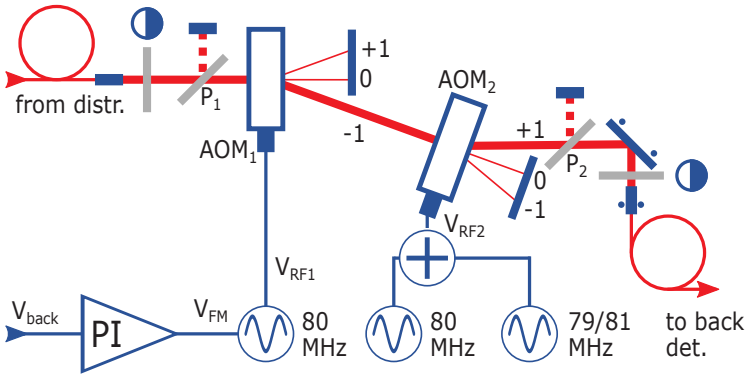


**Figure C.5:** Local oscillator generation.

fiber is polarized by PBS $P_1$ before entering the first $AOM_1$, which is driven by an $80\,\mathrm{MHz}$ radio-frequency (RF) tone*, which can be frequency modulated (FM) by voltage $V_{\mathrm{FM}}$. The negative first-order light (labeled "-1"), which is detuned by $-80\,\mathrm{MHz}$, is separated spatially and sent to the second $AOM_2$, which is driven by the sum two RF-tones of equal power†. The first RF tone is at $80\,\mathrm{MHz}$ and the second can be switched between $79$ and $81\,\mathrm{MHz}$. From $AOM_2$ we separate the positive first order light (labeled "+1") and couple it into a PM fiber.

The input light field to our LO generator is a coherent laser field of the form $E_{\mathrm{in}}e^{-\mathrm{i}\omega_L t}$ with some amplitude $E_{\mathrm{in}}$ and laser frequency $\omega_L$. The AOM combination described before generates the following light field in the output fiber:

$$E_{\mathrm{LO}}(t) = \left(E_{\mathrm{hom}} + E_{\mathrm{het}}\mathrm{e}^{\pm\mathrm{i}\omega_{\mathrm{LO}}t}\right) e^{\mathrm{i}\phi_{\mathrm{LO}}} e^{-\mathrm{i}\omega_L t}. \tag{C.1}$$

The output light is the sum of two light fields due to the fact that we drive $AOM_2$ by the sum of two RF tones. We choose the RF tones with equal power, such that $E_{\mathrm{hom}} \approx E_{\mathrm{het}}$. The field $E_{\mathrm{het}}$ has a negative (positive) frequency shift of $\omega_{\mathrm{LO}} = 2\pi \times 1\,\mathrm{MHz}$ with respect to the laser if the switchable RF frequency is set to $79$ ($81$) $\mathrm{MHz}$. The output phase $\phi_{\mathrm{LO}}$ is controlled by the FM voltage $V_{\mathrm{FM}}$ as

$$\phi_{\mathrm{LO}} = K_O \int_0^t \mathrm{d}t'\, V_{\mathrm{FM}}(t'), \tag{C.2}$$

where $K_O$ is the controlled-oscillator gain (in rad Hz/V).

Note that we use the AOMs in single-pass configuration, which means that the angle of the output beam depends to first order on the applied frequency. We mitigate this problem by coupling into another PM fiber, such that beam pointing modulations turn into amplitude modulations. In other words, $|E_{\mathrm{het}}|^2$ slightly changes when the RF frequency is switched between $79$ and $81\,\mathrm{MHz}$.

*Source: PeakTech 4046 arbitrary waveform generator, amplified by Mini-Circuits ZHL-3A+. For the measurements in chapter 4, we used moglabs XRF421 as a frequency source.

†Adder: Mini-Circuits ZFSC-2-4B-S+

### C.3.1 Locking the interferometer

With the setup described in sections C.2 and C.3, we built an interferometer with the photodetector labeled $V_{\text{back}}$ in Fig. C.4. When balanced, this detector has the following output voltage, which is due to the interference between the LO and the backsacttered particle light:

$$V_{\text{back}} = K_D \left[\sin(\tilde{k}z + \phi_{\text{err}} - \phi_{\text{LO}}) + \sin(\tilde{k}z + \phi_{\text{err}} - \phi_{\text{LO}} \mp \omega_{\text{LO}}t)\right] \quad \text{(C.3)}$$

Here, $K_D$ is the detector's gain (in V) and is proportional to the amplitudes of both the LO and the particle light (we assumed $E_{\text{het}} = E_{\text{hom}}$). The particle position signal $z$ appears on this detector with some factor $\tilde{k}$, which is in the order of the wavenumber $k$, but the exact value of which depends on the geometry of the system (see Ch. 3). Due to drifts of the interferometer, there will always be a slowly varying phase error $\phi_{\text{err}}$ present, which we cannot control. The second sine term in Eq. (C.3) represents the heterodyne measurement of our particle signal, the frequency components of which are solely around the LO frequency of 1 MHz. We omit it in the following and concentrate on the homodyne interference, which reads

$$V_{\text{back}} = K_D \left[\sin(\phi_{\text{err}} - \phi_{\text{LO}}) + \tilde{k}z\cos(\phi_{\text{err}} - \phi_{\text{LO}})\right], \quad \text{(C.4)}$$

where we assumed $\tilde{k}z \ll 1$, which is usually given. In order to have a most sensitive position readout of the particle, we therefore require the homodyne interferometer to be locked with $\phi_{\text{LO}} - \phi_{\text{err}} \approx 0$, in which case we have (to first order in the phase error)

$$V_{\text{back}} = K_D(\phi_{\text{err}} - \phi_{\text{LO}} + \tilde{k}z). \quad \text{(C.5)}$$

To achieve phase locking, we feed $V_{\text{back}}$ to a PI-controller*, whose output $V_{\text{FM}}$ controls the LO phase $\phi_{\text{LO}}$. In the following, we explain how to choose the proportional (P) and integral (I) gains of the PI controller such that stable locking is achieved.

Note that $\phi_{\text{LO}}$ is not proportional to the applied voltage $V_{\text{FM}}$, but to its time

*Zurich Instruments HF2LI

integral due to the FM modulation [see Eq. (C.2)]. It turns out that locking this interferometer is equivalent to locking a second-order phase-locked loop [127]. Around DC, we find

$$\begin{aligned} V_{\text{back}} &= K_D\left(\phi_{\text{err}} - \phi_{\text{LO}}\right) = K_D\left(\phi_{\text{err}} - K_O\int_0^t \mathrm{d}t' V_{FM}\right) \\ &= K_D\phi_{\text{err}} - K_D K_O\int_0^t \mathrm{d}t'\left(PV_{\text{back}} + I\int_0^{t'}\mathrm{d}t'' V_{\text{back}}\right), \end{aligned} \tag{C.6}$$

where we used Eq. (C.2) and plugged in the PI-controller equations. We differentiate the above equation twice with respect to time and find in Fourier space (see App. A):

$$V_{\text{back}}[\omega]\left[-\omega^2 + K_D K_O\left(-\mathrm{i}\omega P + I\right)\right] = -\omega^2 K_D\phi_{\text{err}}[\omega]. \tag{C.7}$$

Now we can find the transfer function from phase error to detected voltage and find

$$\frac{V_{\text{back}}[\omega]}{\phi_{\text{err}}[\omega]} = K_D\frac{-\omega^2}{-\omega^2 - \mathrm{i}\omega\underbrace{K_D K_O P}_{\frac{\omega_0}{Q}} + \underbrace{K_D K_O I}_{\omega_0^2}}. \tag{C.8}$$

This is a second-order high-pass filter with natural frequency $\omega_0 = \sqrt{K_D K_O I}$ and quality factor $Q = \omega_0/(K_D K_O P)$. Slow drifts of the interferometer with frequencies below $\omega_0$ are therefore balanced away. For stable operation, we set $Q = 1/\sqrt{2}$ [127]. With this assumption, we can express the $P$ and $I$ values in terms of the lock bandwidth $\omega_0$ and the system parameters $K_D$ and $K_O$:

$$\begin{aligned} I &= \frac{\omega_0^2}{K_D K_O}, \\ P &= \frac{\sqrt{2}}{K_D K_O}\omega_0. \end{aligned} \tag{C.9}$$

Finally, we need to measure both $K_D$ and $K_O$ in our system. For this, we apply a constant voltage to $V_{\text{FM}}$ such that $\phi_{\text{LO}} = K_O V_{\text{FM}} t$. This leads to an oscillating detector voltage $V_{\text{back}} = K_D \sin\left(\phi_{\text{err}} - K_O V_{\text{FM}} t\right)$. By measuring the oscillation frequency $f_{\text{mod}}$ and amplitude $V_{\text{amp}}$, we find $K_D = V_{\text{amp}}$ and

$K_O = 2\pi f_{\text{mod}}/V_{\text{FM}}$. In practice, we usually apply $V_{\text{FM}} = 0.1\,\text{V}$ and measure $f_{\text{mod}} = 6\,\text{Hz}$ and $V_{\text{amp}} = 15\,\text{mV}$ such that $K_D = 15\,\text{mV}$ and $K_O = 2\pi \times 60\,\text{Hz/V}$. For a desired lock bandwidth of $\omega_0 = 2\pi \times 20\,\text{Hz}$, we find $P = 31$ and $I = 2.8\,\text{kHz}$. These values can be used to configure the PI loop in the lab. Note that we want our lock bandwidth $\omega_0$ to be much smaller than our signal frequency, which is the particle's oscillation frequency.

## C.4 Forward detection scheme

The forward scattered light by the particle is collimated by an aspheric collection lens* inside the vacuum chamber and send through a Faraday isolator†, which minimizes backreflections into the trap, to a set of photodetectors. For the measurements in chapter 2, this setup was identical to the one described by Vijay Jain [46]. Most of the light (about $80\,\text{mW}$) was directed to a home-built, high-power balanced photodetector [128] measuring the y-motion, while small fractions were directed to two more detectors ($x$ and $z$).

In chapter 4, we made use of the backscattered light and changed the forward detection setup as depicted in Fig. C.6. A small fraction ($1\,\text{mW}$) of the light is sent to a quadrant photodiode‡ to measure the transverse motions ($x$ and $y$). About $20\,\text{mW}$ are sent to a balanced photodiode to measure the longitudinal motion and about $80\,\text{mW}$ are dumped at a beam block (not shown). It turns out that there is enough signal from the transverse directions ($x$ and $y$) on the

*Lightpath 355330, C-coated, NA=0.77
†Qioptiq LINOS FI-1060-3SC HP
‡Thorlabs PDQ30C

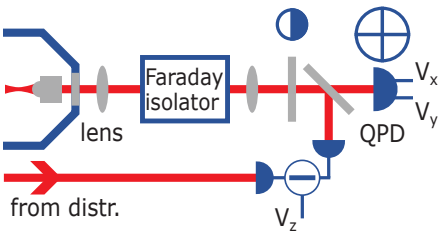


**Figure C.6:** Forward detection scheme.

backscatter detector to stabilize the particle sufficiently, such that the forward scattered detector can also be completely removed including the collection lens.

## C.5 Electric feedback scheme

In order to electrically feedback cool the particle motion using a linear feedback force, we employ both analog and digital electronics as depicted in Fig. C.7. In this section we explain the details of the electronic setup, which was used in chapters 2 and 4. Ideally, the feedback would be a perfect derivative filter with arbitrary gain*, which means $V_{\mathrm{FB}} \propto -\gamma_{\mathrm{FB}} \mathrm{d}V_d/\mathrm{d}t$, where $V_{\mathrm{FB}}$ is the voltage applied to the electrode at the trap, $V_d$ is the detector voltage measuring the particle position, and $\gamma_{\mathrm{FB}}$ is the feedback gain which should be tunable (see Ch. 2). In Fourier space we have $V_{\mathrm{FB}}[\omega] \propto \mathrm{i}\gamma_{\mathrm{FB}}\omega V_d[\omega]$.

Our particle's motion is resonant with center frequency $\Omega$ and small bandwidth. Instead of implementing a derivative filter, we mimic its effect by delaying the signal for time $\tau = \pi/(2\Omega)$. In frequency space, this means $V_{\mathrm{FB}}[\omega] \propto \gamma_{\mathrm{FB}} \exp[\mathrm{i}\pi\omega/(2\Omega)] V_d[\omega] = \mathrm{i}\gamma_{\mathrm{FB}} V_d[\omega] \exp[\mathrm{i}\pi\Delta/(2\Omega)]$ [see Eq. (A.4)], where $\Delta = \omega - \Omega$ is the detuning from the system's center frequency. This delay filter mimics a derivative filter, but makes both a phase and an amplitude error for $\Delta \neq 0$. To first order, the phase error is $\pi\Delta/(2\Omega)$ and the relative amplitude error is $-\Delta/\Omega$.

After this general introduction, let us turn our attention to the implementation. The delay is implemented digitally (see Sec. C.6) with a time-step size of 32 ns and a maximum delay of 32.8 µs. Since the delay is a quarter of a period

*Note the discussion in App. B.

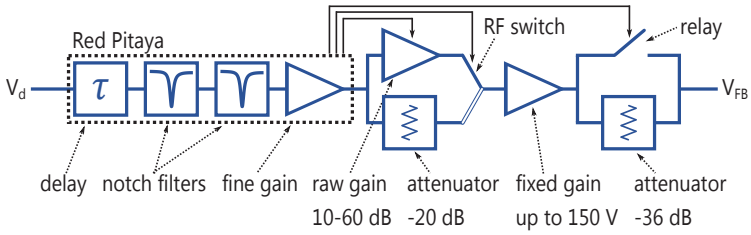


**Figure C.7:** Electric feedback scheme.

as explained above, the range of delay corresponds to oscillation frequencies from 7.6 kHz to the 10 MHz regime. At a frequency of 50 kHz, like in chapter 4, we can tune the phase with an accuracy of $2\pi\ 50\,\mathrm{kHz} \cdot 32\,\mathrm{ns} = 0.576°$.

We use two digital, second-order notch filters with quality factor 5 and tunable center frequency to remove the oscillation frequencies from the other two particle modes (along the axes we are not interested in) from the signal. The final digital component allows us to fine-tune the overall gain of the feedback. All of the digital filters described above are implemented on an FPGA on the platform *Red Pitaya*. A detailed description of this is given in Sec. C.6.

We need our filter to function over many orders of magnitude of gain. Using a set of analog amplifiers and attenuators, we can control the gain in a range of 86 dB, across which the feedback noise is limited by its input noise. The first amplifier's* gain can be controlled from the Red Pitaya across a range of 50 dB with 10 dB steps. Afterward, a high-voltage amplifier† amplifies the signal up to $\pm 150$ V. A combination of an RF attenuator‡ and a relay at the output of the high-voltage amplifier increases the total range of the analog gain to 86 dB.

To perform reheating measurements (chapter 2), a fast RF switch§ can be controlled from the Red Pitaya. When switched, it bypasses the first analog amplifier, effectively lowering the feedback gain by at least 30 dB, depending on the amplifier's gain setting.

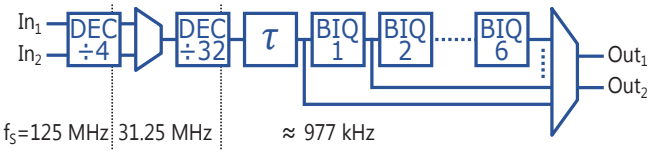


**Figure C.8:** Biquad filter implementation on Red Pitaya. Each component can be configured via Ethernet.

## C.6 FPGA implementation of electronic feedback

A central part of the previously described feedback are digitally implemented filters running on a versatile open-source platform called *Red Pitaya*. We implemented a set of six so-called biquad filters (BIQ) that can be independently configured from a PC. This section gives an overview of our implementation but does not serve as a comprehensive documentation of the code. A related project developed during this PhD is a fully functional phase-locked loop running on the Red Pitaya platform. A documentation can be found online[*].

At the heart of each Red Pitaya is a field-programmable gate array (FPGA)[†], which can be freely programmed. In addition to the configurable hardware, a Red Pitaya includes a small CPU and memory running Linux for easy access. Peripherals include two analog-to-digital converters (ADCs) and two digital-to-analog converters (DACs), all of which run at a clock frequency of $125\,\mathrm{MHz}$ and a resolution of $14\,\mathrm{bits}$, as well as an Ethernet connection. A high-level schematic of the FPGA circuitry is shown in Fig. C.8. At first, the 14-bit samples from the two ADCs at a sample frequency of $125\,\mathrm{MHz}$ are downsampled by a factor of four in a decimation filter (DEC) to $31.25\,\mathrm{MHz}$. This also serves as the clock frequency for the following hardware and hence the clock period is $32\,\mathrm{ns}$. A multiplexer selects one of the input signals, which is further downsampled by a factor 32 to $976.5625\,\mathrm{kHz}$. The frequency of the input signal is therefore (Nyquist)-limited to about $488\,\mathrm{kHz}$, which is half the sample frequency. Note the difference between sample and clock frequency. Samples propagate through the system at the sample frequency, while the underlying logic operates at the clock frequency. The next element is a delay filter, which can delay the signal by up to 32 steps at the sample rate ($977\,\mathrm{kHz}$) and by another 32 steps at the clock frequency ($31.25\,\mathrm{MHz}$). This allows for delays of up to $32.8\,\mu\mathrm{s}$ with a step size of $32\,\mathrm{ns}$. Next, the signal enters a pipeline of six BIQs, which we describe below. Finally, we can (at runtime) connect the output ADCs to any of

[*] Femto DHPVA-201
[†] Falco Systems WMA-300
[‡] Mini-Circuits BW-S30W5+
[§] Mini-Circuits ZX80-DR230+
[*] https://git.ee.ethz.ch/tefelix/redpitayapll
[†] Xilinx Zynq 7010 SoC

the BIQs or to the delay filter using another multiplexer.

Each biquad filter implements the following difference equation

$$y_n = a_0 x_n + a_1 x_{n-1} + a_2 x_{n-2} - b_1 y_{n-1} - b_2 y_{n-2}, \tag{C.10}$$

where $a_{1,2,3}$ and $b_{1,2}$ are real parameters. $y_n$ ($x_n$) is the current output (input) sample. The output depends on previous input samples $x_{n-i}$ and also previous output samples $y_{n-i}$. Such a filter is called infinite-impulse response (IIR) filter of second order. The five parameters can be configured at runtime. This way, each BIQ can implement a second-order low-, high-, or band- pass as well as a notch (band-stop) filter. A helpful blog about this topic with a coefficient calculator can be found under Ref. [129]. The necessary accuracy of each of the parameters roughly scales with the ratio of sample to natural frequency of the filter. This motivates to minimize the sample frequency as much as possible. Since our system frequencies are in the 10-100 kHz regime, we chose to downsample to about 1 MHz, as described above. Each BIQ can also attenuate or amplify the signal, which we use to fine-tune the feedback gain in Sec. C.5. The digital implementation of the BIQs is based on the blog in Ref. [130]. The filter values are controlled via Ethernet connection and a python script from the laboratory PC.

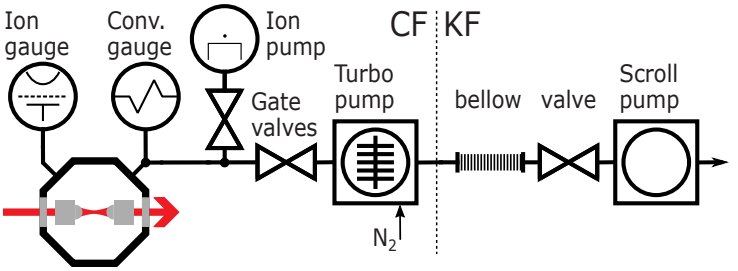


**Figure C.9:** Schematic of the vacuum system. All vacuum components from the trap to the turbo pump have CF flanges with copper gaskets. The prepump system has KF flanges.

## C.7 Vacuum system

The vacuum system (see Fig. C.9) was built by Vijay Jain (Ref. [46]) and consists of a vacuum chamber* with the optical trap. It is pumped with a combination of three pumps, a turbo pump (TP) † backed by a scroll pump ‡, and an ion getter pump (IGP)§. We slightly modified the system from Ref. [46] with the goal to pump to lower pressure. We removed a $2\,\mathrm{m}$ long flexible bellow between the TP and the chamber reducing the vacuum volume, such that the pump lies on the optical table now. We can observe its rotation frequency in the spectrum, but importantly this does not affect trapping and we can close a gate valve to disconnect the TP from the chamber and switch it off. In this case, the chamber's pressure is kept constant solely by the IGP. Just before writing this thesis, we exchanged the vacuum windows ¶ which included Viton O-rings for ones without O-rings ‖. This clearly improved the base pressure of the chamber to $2 \times 10^{-9}\,\mathrm{mbar}$.

## C.8 Photodetector characterization against shot noise

An important task in characterizing a photodetector is to resolve photon shot noise. This section is intended to serve as a guideline for other experimentalists. First, we concentrate on a single photodiode detector and then turn to a balanced photodetector.

We focus a laser beam of power $P$ on a photodetector with known transfer function $Z_{\mathrm{TF}}(f)$. $Z_{\mathrm{TF}}(f)$ describes the gain from photocurrent $I$ to the detector voltage $V$ in units of $\Omega$. It is usually a first-order low-pass filter with DC transimpedance gain $Z_{\mathrm{TF}}(0)$ and should be specified in the detector's datasheet. We first measure the responsivity $\mathcal{R} = I/P$ of the photodiode to estimate the coupling efficiency. For this, we measure the DC voltage $V$ and divide by the DC transimpedance gain $Z_{\mathrm{TF}}(0)$ to get $I$. In order to exclude detector

*Kimball Physics MCF600-SphOct-F2C8
†Agilent TwisTorr 304 FS
‡Agilent S110
§SAES NEXTorr D 200-5
¶Thorlabs VPCH42-C
‖Torr Scientific VPZ38, AR coated at $1064\,\mathrm{nm}$

nonlinearities, we should repeat this at different power levels $P$ and fit the linear regime for small powers. By comparing the measured to the specified $\mathcal{R}$, we get an idea of how well we couple the light into the photodiode. Note, however, that any error in the original power measurement (*e.g.* with a dedicated power meter) will directly translate into an error in the measured $\mathcal{R}$. Next, we measure a single-sided PSD $\tilde{S}_{VV}(f)$ of the detector voltage. We refer to dissertation [44] for details on this procedure. We convert to the PSD of the photocurrent $\tilde{S}_{II}(f) = \tilde{S}_{VV}(f)/|Z_{\mathrm{TF}}(f)|^2$, which we can compare to the known (constant) value of shot noise $\tilde{S}_{II}^{\mathrm{sn}}(f) = 2qI$ [Eq. (A.24)].

Every real measurement is subject to other noise sources, such that the measured noise $\tilde{S}_{II}(f)$ always exceeds shot noise $\tilde{S}_{II}^{\mathrm{sn}}$. At least, there will be input noise of the measurement device, electronic noise of the detector, and excess RIN of the laser. By disconnecting the detector, or better by shorting the input to the measurement device with a $50\,\Omega$ termination, we measure the input noise. Electronic detector noise is measured by blocking the optical power. Both of these should be much smaller than the optical noise floor. Laser RIN exceeding shot noise will be present for large optical power and depends on the laser's stability.

Another way to identify shot noise in an optical measurement is to look at the scaling of $\tilde{S}_{II}(f)$ with the input power $P$ [131]. Electronic noise arising in the detector does not scale with the input power, and excess RIN scales with a square law. Only shot noise *should* scale linearly with the input power, and this way the three processes can be differentiated. Importantly, this method fails if the optical power $P$ is tuned by active elements, which add noise themselves. The power $P$ should be tuned passively, *e.g.* using neutral density filters, in this scaling method.

In a balanced detection scheme, excess RIN can be removed because it is common mode to both photodiodes. Note that characterizing the responsivity $\mathcal{R}$ can be more challenging here. This is because we often put a large power on each photodiode, which would saturate the detector if it would not be balanced by the other diode. The DC detector voltage, however, is now a measure for the detector imbalance and not for the optical input power, which gives rise to shot noise. In this case, we characterize the responsivity $\mathcal{R}$ by using a small power on only one of the photodiodes without saturating the detector. The

following procedure of comparing the measured noise floor to shot noise is then in analogy to the case of a single photodiode detector.

# D

# SI: Optimal position detection

Here we present supplementary information to chapter 3. This supplement was published with the article F. Tebbenjohanns, M. Frimmer, and L. Novotny, Phys. Rev. A **100**, 043821 (2019).

## D.1 Effective wavelength of focused field

In this Appendix, we show that a strongly focused field in the focal region appears, to first order, as a plane wave propagating along the optical axis with an effective wavelength determined by the numerical aperture of the focusing lens. We start with the focal field generated by a highly overfilled objective, which can be written analytically in cylindrical coordinates $(\rho, \phi, z)$ as [42]

$$\mathbf{E}_{\text{foc}} \propto \begin{pmatrix} I_{00} + I_{02}\cos(2\phi) \\ I_{02}\sin(2\phi) \\ -2\mathrm{i}I_{01}\sin(\phi) \end{pmatrix}, \tag{D.1}$$

where the incoming light is polarized along $x$. The integrals $I_{00}$, $I_{01}$, and $I_{02}$ depend on coordinates $\rho$ and $z$:

$$I_{00} = \int_0^{\Theta_{\text{tl}}} \mathrm{d}\theta \, \sqrt{c} s (1+c) J_0(k\rho s) \mathrm{e}^{\mathrm{i}kzc}, \tag{D.2a}$$

$$I_{01} = \int_0^{\Theta_{\text{tl}}} \mathrm{d}\theta \, \sqrt{c} s^2 J_1(k\rho s) \mathrm{e}^{\mathrm{i}kzc}, \tag{D.2b}$$

$$I_{02} = \int_0^{\Theta_{\text{tl}}} \mathrm{d}\theta \, \sqrt{c} s (1-c) J_2(k\rho s) \mathrm{e}^{\mathrm{i}kzc}, \tag{D.2c}$$

where $c = \cos(\theta)$ and $s = \sin(\theta)$. Furthermore, $J_n$ are the Bessel functions of the first kind for $n \in \{0, 1, 2\}$, which we expand to first order as $J_0(x) = 1$, $J_1(x) = x/2$, and $J_2(x) = 0$. The $x$ component of $\mathbf{E}_{\text{foc}}$ to first order reads $C + \mathrm{i}kzD \approx C \exp(\mathrm{i}kzD/C)$ where $C$ and $D$ are integrals over $\theta$ which are independent of any coordinates. The electric field component along $y$ vanishes to first order. The phase of the $z$ component of the field is constant to first order, but its amplitude is linear in the transverse directions and vanishes at the origin. Importantly, the $z$ component of the field is $\pi/2$ out of phase with the $x$ polarization such that it appears only to second order in standard homodyne detection schemes. We hence conclude that the focal field in close vicinity to the focus can be approximated as an $x$ polarized plane wave traveling in the positive $z$ direction according to $\mathbf{E}_{\text{foc}} = E_0 \mathbf{n}_x \exp(\mathrm{i}Akz)$, with

$$A = \frac{\int_0^{\Theta_{\text{tl}}} \mathrm{d}\theta \, s\sqrt{c}(1+c)c}{\int_0^{\Theta_{\text{tl}}} \mathrm{d}\theta \, s\sqrt{c}(1+c)}. \tag{D.3}$$

See App. D.5 for an analytical expression for $A$.

## D.2 Derivation of measurement backaction

The differential power $\mathrm{d}p_{\text{dip}}$ radiated by an $x$ polarized dipolar scatterer into solid angle $\mathrm{d}\Omega = \sin(\theta)\mathrm{d}\theta\mathrm{d}\phi$ is given by Eq. (3.3). This power exerts a radiation pressure force $\mathrm{d}F^x_{\text{rp}} = -(\mathbf{n}_x \cdot \mathbf{n}_r)\mathrm{d}p_{\text{dip}}/c$ on the scatterer along the $x$ direction. Assuming shot noise to dominate the fluctuations of the scattered power, we find for the power spectral density of the scattered power $\mathrm{d}p_{\text{dip}}$ along

direction $\mathbf{n}_r$*

$$\mathrm{d}s_{pp}(\theta,\phi) = \frac{\hbar k c}{2\pi}\mathrm{d}p_{\mathrm{dip}}. \tag{D.4}$$

Due to these fluctuations, the radiation pressure force along $\mathbf{n}_x$ fluctuates with power spectral density $\mathrm{d}s^x_{\mathrm{ba}} = (\mathbf{n}_x \cdot \mathbf{n}_r)^2\ \mathrm{d}s_{pp}(\theta,\phi)/c^2$. We integrate this differential contribution to the measurement backaction over the unit sphere to find the backaction noise spectral density along the $x$ direction:

$$S^x_{\mathrm{ba}} = \int \mathrm{d}s^x_{\mathrm{ba}}(\theta,\phi) = \frac{1}{5}\frac{\hbar k}{2\pi c}P_{\mathrm{dip}}. \tag{D.5}$$

By analogous derivations, we find the values for $S^y_{\mathrm{ba}}$ and $S^z_{\mathrm{ba}}$ as given by Eqs. (3.4). As described in the main text, along the $z$ direction, $S^z_{\mathrm{ba}}$ needs to be amended by an additional contribution for a scatterer polarized by a traveling wave, which exerts a radiation pressure force along its propagation direction. While our derivation rests on a semiclassical treatment, our results match a full quantum derivation for a two-level system in the classical limit [76].

## D.3 Derivation of optimal measurement imprecision

In this Appendix, we derive the measurement imprecision of our ideal measurement scheme. Equation (3.6) in the main text is the differential power impinging on a detector covering a solid angle $\mathrm{d}\Omega$ and located at $(\theta,\phi)$. Let us temporarily assume that the scatterer is only displaced along the $x$ axis, such that $y_0 = z_0 = 0$. Then, the locally measured power

$$\mathrm{d}p_{\mathrm{det}}(\theta,\phi) = [\gamma^2 + 2\gamma k \sin(\theta)\cos(\phi)x_0]\mathrm{d}p_{\mathrm{dip}} \tag{D.6}$$

linearly depends on position $x_0$ and therefore is a measure for the scatterer's position $x_0$. The first term contributing to $\mathrm{d}p_{\mathrm{det}}$ is independent of $x_0$, but dominates the fluctuations of the measurement through photon shot noise. The power spectral density of the fluctuations is

$$\mathrm{d}s^{\mathrm{det}}_{pp}(\theta,\phi) = \frac{\hbar k c}{2\pi}\gamma^2\mathrm{d}p_{\mathrm{dip}}. \tag{D.7}$$

*Compare Eq. (A.23).

In order to extract the position $x_0$ from the differential detector signal Eq. (D.6), it needs to be divided by the pre-factor $\mathrm{d}\beta(\theta,\phi) = 2\gamma k \sin(\theta)\cos(\phi)\mathrm{d}p_{\mathrm{dip}}$. Accordingly, we translate the fluctuations given in Eq. (D.7) to fluctuations of the position as

$$s^x_{\mathrm{imp}}(\theta,\phi) = \frac{\mathrm{d}s^{\mathrm{det}}_{pp}(\theta,\phi)}{\mathrm{d}\beta(\theta,\phi)^2}. \tag{D.8}$$

In analogy, we derive $s^y_{\mathrm{imp}}(\theta,\phi)$ and $s^z_{\mathrm{imp}}(\theta,\phi)$ given in Eqs. (3.7). Recall that $s^j_{\mathrm{imp}}(\theta,\phi)$ for $j \in \{x,y,z\}$ are the power spectral densities of the measurement imprecision associated with a differential detector located at $(\theta,\phi)$. Importantly, we find $s^j_{\mathrm{imp}}(\theta,\phi) \propto 1/(\mathrm{d}\Omega)$, meaning that as the solid angle $\mathrm{d}\Omega$ goes to zero the imprecision noise of the detector diverges to infinity. This intuitively makes sense, since the signal vanishes together with the detector area.

As mentioned in the main text, we perform inverse-variance weighting [77] in order to minimize the total imprecision when the signals from all detectors covering the unit sphere are combined. The local reading of $x_0$ is hence weighted with the inverse of $s^x_{\mathrm{imp}}(\theta,\phi)$ before averaging over the unit sphere. The total imprecision then turns out to be [see Eq. (D.28)]

$$S^x_{\mathrm{imp}} = \left[\int \frac{1}{s^x_{\mathrm{imp}}(\theta,\phi)}\right]^{-1} = \left[\int \frac{\mathrm{d}\beta(\theta,\phi)^2}{\mathrm{d}s^{\mathrm{det}}_{pp}(\theta,\phi)}\right]^{-1} = 5\frac{\hbar c}{8\pi k}\frac{1}{P_{\mathrm{dip}}}, \tag{D.9}$$

where the integral runs over the full unit sphere. The results for all three axes are given in Eqs. (3.8).

Finally, let us drop our assumption that the scatterer is only displaced along one axis and allow for the position $\mathbf{r}_0$ to have three non-zero components. In this case, $\mathrm{d}p_{\mathrm{det}}$ depends on a linear superposition of $x_0$, $y_0$, and $z_0$ and, therefore, also the local reading for the position along $x$

$$\begin{aligned}\tilde{x}_0(\theta,\phi) &= \frac{\mathrm{d}p_{\mathrm{det}}(\theta,\phi) - \gamma^2\mathrm{d}p_{\mathrm{dip}}}{\mathrm{d}\beta(\theta,\phi)} \\ &= x_0 + y_0\tan(\phi) + z_0\frac{\cos(\theta)-A}{\sin(\theta)\cos(\phi)}\end{aligned} \tag{D.10}$$

includes contributions by $y_0$ and $z_0$. Nevertheless, when combining the information from all differential detectors correctly, following the procedure of inverse

variance weighting, we indeed find

$$x_0 = S^x_{\text{imp}} \int \frac{\mathrm{d}\beta(\theta,\phi)^2}{\mathrm{d}s^{\text{det}}_{pp}(\theta,\phi)}\, \tilde{x}_0(\theta,\phi), \tag{D.11}$$

meaning that the contributions of $y_0$ and $z_0$ cancel. Analogously, $y_0$ and $z_0$ can be extracted from the measurements $\mathrm{d}p_{\text{det}}$ using

$$\tilde{y}_0(\theta,\phi) = \frac{\mathrm{d}p_{\text{det}} - \gamma^2 \mathrm{d}p_{\text{dip}}}{2\gamma k \sin(\theta)\sin(\phi)\,\mathrm{d}p_{\text{dip}}}, \tag{D.12a}$$

$$\tilde{z}_0(\theta,\phi) = \frac{\mathrm{d}p_{\text{det}} - \gamma^2 \mathrm{d}p_{\text{dip}}}{2\gamma k[\cos(\theta) - A]\,\mathrm{d}p_{\text{dip}}}, \tag{D.12b}$$

together with an appropriately adjusted version of Eq. (D.11).

## D.4 Derivation of realistic measurement imprecision

The situation under consideration is sketched in Fig. D.1. An $x$ polarized plane wave is focused by a trapping lens with numerical aperture $\mathrm{NA}_{\text{tl}} = \sin(\Theta_{\text{tl}})$

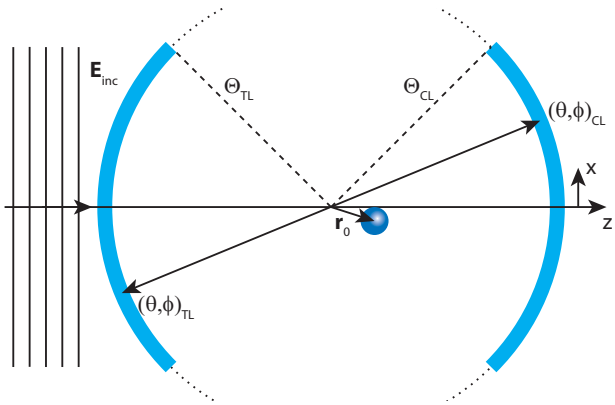


**Figure D.1:** Laboratory detection system. A trapping lens with numerical aperture $\mathrm{NA}_{\text{tl}} = \sin(\Theta_{\text{tl}})$ focuses an $x$ polarized plane wave. On the opposite side, the fields are collimated by a collection lens with numerical aperture $\mathrm{NA}_{\text{cl}} = \sin(\Theta_{\text{cl}})$. The coordinate pair $(\theta, \phi)$ denotes a point both on the collection and on the trapping lens. A particle close to the focal point scatters the focused field.

before being recollimated by a collection lens with numerical aperture $\mathrm{NA}_{\mathrm{cl}} = \sin(\Theta_{\mathrm{cl}})$. A dipolar scatterer is positioned at $\mathbf{r}_0$ in close vicinity to the focus located at the origin. The scattered field, given by Eq. (3.2), is interfered with the trapping beam on the reference surface of the collection lens. We formulate the fields using the formalism laid out in Ref. [42], such that the electric field on the reference sphere of the trapping lens reads

$$\mathbf{E}_\infty = E_{\mathrm{inc}} \left[ -\sin(\phi)\mathbf{n}_\phi + \cos(\phi)\mathbf{n}_\theta \right] \sqrt{\cos(\theta)}. \tag{D.13}$$

Here, $\mathbf{n}_\phi$ and $\mathbf{n}_\theta$ are spherical unit vectors along the azimuthal and polar direction, respectively. Note that in our notation, the polar angle $\theta$ spans the range $[0 \ldots \pi/2]$, while the azimuthal angle $\phi$ spans $[0 \ldots 2\pi]$. Therefore, the coordinate pair $(\theta, \phi)$ denotes both a point on the trapping lens and a point on the collection lens (lying diametrically opposite relative to the origin). In this notation, the trapping field on the collection lens (where it serves as the reference field in a forward-scattering detection scheme) takes the exact same form as the field in Eq. (D.13), besides an additional (irrelevant) phase factor accounting for propagation through the focal region.

### D.4.1 Quadrant detection in the forward direction

We first turn our attention to the case of detection in the forward direction, where the field trapping the particle naturally serves as a self-aligned reference field. The total field on the reference sphere of the collection lens reads $\mathbf{E}_\infty + \mathrm{i}\mathbf{E}_{\mathrm{sc}}$, with $\mathbf{E}_{\mathrm{sc}}$ the field scattered by the particle from Eq. (3.2). The relative phase between both fields is fixed to $\pi/2$, since the field in the focal region (driving the dipolar scatterer) carries the Gouy phase shift relative to the field on the reference sphere (and the polarizability of the particle is assumed to be purely real) [42].

Under the assumption of a strong reference field and a small particle displacement $\mathbf{r}_0$ from the origin, the differential power in direction $(\theta, \phi)$ per

unit solid angle is

$$\begin{aligned}\frac{\mathrm{d}p_{\mathrm{cl}}(\theta,\phi)}{\mathrm{d}\Omega} &= P_{\mathrm{inc}}\cos(\theta) + \sqrt{3P_{\mathrm{dip}}P_{\mathrm{inc}}\cos(\theta)/(2\pi)} \\ &\times \left[\sin(\phi)^2 + \cos(\phi)^2\cos(\theta)\right] \\ &\times k\left(\mathbf{r}_0\cdot\mathbf{n}_r - Az_0\right).\end{aligned} \tag{D.14}$$

Here, $P_{\mathrm{inc}} \propto E_{\mathrm{inc}}^2$ is the power of the trapping beam. Note that the polarization of the scattered dipole field $\mathbf{E}_{\mathrm{dip}} \propto [\mathbf{n}_x - (x/r)\mathbf{n}_r]$ differs from the reference field. As usual in homodyne detection, we find two contributions to the power. The first contribution is independent of the scatterer's position and dominates the associated photon shot noise, while the second (interference) term is a measure for the scatterer's position $\mathbf{r}_0$.

Typically, the intensity distribution on the reference sphere is not spatially resolved. Instead, the fields are sent to a quadrant photodetector aligned along the $x$ and $y$ axes. The detector measures the integrated power striking the individual quadrants. The power $P_1^Q$ in the first quadrant is given by

$$\begin{aligned}P_1^Q =& \int_0^{\Theta_{\mathrm{cl}}} \mathrm{d}\theta\ \sin(\theta) \int_0^{\pi/2} \mathrm{d}\phi\ p_{\mathrm{cl}}(\theta,\phi) \\ =& P_{\mathrm{inc}}\frac{\pi}{4}\mathrm{NA}_{\mathrm{cl}}^2 + k\sqrt{3P_{\mathrm{inc}}P_{\mathrm{dip}}/(2\pi)}\mathbf{B}^{\mathrm{fw}}\mathbf{r}_0.\end{aligned} \tag{D.15}$$

The powers $P_n^Q$ in the other quadrants ($n = 2,3,4$) are equivalent with the replacements $x_0 \to -x_0$ for $n \in \{2,3\}$ and $y_0 \to -y_0$ for $n \in \{3,4\}$. In Eq. (D.15), we have furthermore introduced the quantity

$$\mathbf{B}^{\mathrm{fw}} = \int_0^{\Theta_{\mathrm{cl}}} \mathrm{d}\theta\ s\sqrt{c}\begin{pmatrix} s(1+2c)/3 \\ s(2+c)/3 \\ \pi(c-A)(1+c)/4 \end{pmatrix}, \tag{D.16}$$

where we use the abbreviations $s = \sin(\theta)$ and $c = \cos(\theta)$. An analytical solution of the third component $B_z^{\mathrm{fw}}$ is given in Appendix D.5. We note that the particle position $\mathbf{r}_0$ can be extracted from the values $P_n^Q$ of the quadrant

detector. Specifically we have

$$(P_1^Q + P_4^Q) - (P_2^Q + P_3^Q) = P_x^{\text{cal}}\, kx_0, \tag{D.17a}$$

$$(P_1^Q + P_2^Q) - (P_3^Q + P_4^Q) = P_y^{\text{cal}}\, ky_0, \tag{D.17b}$$

$$\sum_{n=1}^{4} P_n^Q - P_{\text{inc}}\pi \text{NA}_{\text{cl}}^2 = P_z^{\text{cal}}\, kz_0, \tag{D.17c}$$

with the calibration factors

$$P_j^{\text{cal}} = \sqrt{24 P_{\text{inc}} P_{\text{dip}}/\pi}\; B_j^{\text{fw}}, \quad j \in \{x, y, z\}, \tag{D.18}$$

where $B_j^{\text{fw}}$ is the $j$th vector component of Eq. (D.16). To get access to $z_0$, a constant reference power has to be subtracted. Assuming that the detection is shot-noise limited, each of the position measurements will be subject to fluctuations with a white power spectrum

$$S_{PP}^Q = \frac{\hbar k c}{2} P_{\text{inc}} \text{NA}_{\text{cl}}^2, \tag{D.19}$$

arising from the first term in Eq. (D.15). By dividing these fluctuations by the calibration factor $(P_j^{\text{cal}} k)^2$, we find the imprecision noise spectral density for the motion of the particle along the $j$ axis

$$S_{\text{imp}}^{j,\text{fw}} = \frac{S_{PP}^Q}{(P_j^{\text{cal}} k)^2} = \frac{\hbar c}{k P_{\text{dip}}} \frac{\pi \text{NA}_{\text{cl}}^2}{48 \left(B_j^{\text{fw}}\right)^2}. \tag{D.20}$$

As detailed in Sec. 3.3, we compare the calculated imprecision noise of the realistic detection system to the one obtained in the ideal case [Eqs. (3.8)] to obtain the measurement efficiencies in forward scattering, which are plotted in

Fig. 3.4(a):

$$\eta_x^{\mathrm{fw}} = \frac{30\left(B_x^{\mathrm{fw}}\right)^2}{\pi^2 \mathrm{NA}_{\mathrm{cl}}^2}, \tag{D.21a}$$

$$\eta_y^{\mathrm{fw}} = \frac{15\left(B_y^{\mathrm{fw}}\right)^2}{\pi^2 \mathrm{NA}_{\mathrm{cl}}^2}, \tag{D.21b}$$

$$\eta_z^{\mathrm{fw}} = \frac{1}{1+\frac{5}{2}A^2}\frac{15\left(B_z^{\mathrm{fw}}\right)^2}{\pi^2 \mathrm{NA}_{\mathrm{cl}}^2}. \tag{D.21c}$$

Finally, we discuss the feature that $\eta_z^{\mathrm{fw}}$ plotted in Fig. 3.4(a) vanishes for a symmetric setup. This feature can be understood by looking at $B_z^{\mathrm{fw}} = (\pi/4)\int_0^{\Theta_{\mathrm{cl}}} \mathrm{d}\theta\; s\sqrt{c}(c-A)(1+c)$ from Eq. (D.16), with $c = \cos(\theta)$ and $s = \sin(\theta)$. The factor $[\cos(\theta) - A]$ in the integrand changes sign as the collection angle $\theta$ passes a certain critical value. For a symmetric setup ($\mathrm{NA}_{\mathrm{tl}} = \mathrm{NA}_{\mathrm{cl}}$), the integration over $\theta$ is truncated such that it strictly vanishes. This result can be obtained directly by plugging Eq. (D.3) into $B_z^{\mathrm{fw}}$ and assuming $\mathrm{NA}_{\mathrm{tl}} = \mathrm{NA}_{\mathrm{cl}}$.

Note that the derivation presented here tacitly assumed $\mathrm{NA}_{\mathrm{cl}} < \mathrm{NA}_{\mathrm{tl}}$, since when $\theta$ exceeds the maximum angle of the trapping beam $\Theta_{\mathrm{tl}} = \sin^{-1}(\mathrm{NA}_{\mathrm{tl}})$ the reference power drops to zero, such that there is no signal (but also no excess noise). For this reason, the detection efficiencies plotted in Fig. 3.4(a) are constant for $\mathrm{NA}_{\mathrm{cl}} > \mathrm{NA}_{\mathrm{tl}}$.

### D.4.2 Quadrant detection in the backward direction

To analyze the case of backscattering detection, we assume a reference field, which has the same spatial distribution as the trapping field. The reference beam is then identical to Eq. (D.13) by our choice of coordinates. Following the same derivations as in Sec. D.4.1, with the field scattered by the dipole expressed in the coordinate system given by the reference spheres, we find expressions for the imprecision noise spectral densities in backward scattering $S_{\mathrm{imp}}^{j,\mathrm{bw}}$. They are identical to Eq. (D.20) under the substitutions $\Theta_{\mathrm{cl}} \to \Theta_{\mathrm{tl}}$, $\mathrm{NA}_{\mathrm{cl}} \to \mathrm{NA}_{\mathrm{tl}}$, as

well as $\mathbf{B}^{\mathrm{fw}} \to \mathbf{B}^{\mathrm{bw}}$, with

$$\mathbf{B}^{\mathrm{bw}} = \int_0^{\Theta_{\mathrm{tr}}} \mathrm{d}\theta \; s\sqrt{c} \begin{pmatrix} s(1+2c)/3 \\ s(2+c)/3 \\ \pi(c+A)(1+c)/4 \end{pmatrix}, \tag{D.22}$$

where $s = \sin(\theta)$ and $c = \cos(\theta)$. Note that $\mathbf{B}^{\mathrm{bw}}$ differs from $\mathbf{B}^{\mathrm{fw}}$ only in the third vector component. Since both $A$ and $\mathbf{B}^{\mathrm{bw}}$ depend on $\Theta_{\mathrm{tl}}$, the $z$ component can be further simplified by inserting Eq. (D.3) for $A$, which yields

$$B_z^{\mathrm{bw}} = \frac{\pi}{2} \int_0^{\Theta_{\mathrm{tl}}} \mathrm{d}\theta \; s\sqrt{c}(1+c)c. \tag{D.23}$$

An analytical solution of $B_z^{\mathrm{bw}}$ is given in Appendix D.5. In analogy to forward scattering, we compare the obtained imprecision noise $S_{\mathrm{imp}}^{j,\mathrm{bw}}$ to the one for an ideal measurement given by Eqs. (3.8), in order to compute the detection efficiencies in backscattering $\eta_j^{\mathrm{bw}}$, as plotted in Fig. 3.4(b).

## D.5 Analytical solutions

In this appendix, we calculate analytical solutions of Eqs. (D.3), (D.16), and (D.23). To ease our notation, we define

$$C(\Theta) = \int_0^{\Theta} \mathrm{d}\theta \; s\sqrt{c}(1+c), \tag{D.24a}$$

$$D(\Theta) = \int_0^{\Theta} \mathrm{d}\theta \; s\sqrt{c}(1+c)c, \tag{D.24b}$$

where $s = \sin(\theta)$ and $c = \cos(\theta)$. We can solve both integrals analytically and find

$$C(\Theta) = 2\left(\frac{8}{15} - \frac{\cos(\Theta)^{3/2}}{3} - \frac{\cos(\Theta)^{5/2}}{5}\right), \tag{D.25a}$$

$$D(\Theta) = 2\left(\frac{12}{35} - \frac{\cos(\Theta)^{5/2}}{5} - \frac{\cos(\Theta)^{7/2}}{7}\right). \tag{D.25b}$$

This allows us to find solutions of the following integrals in terms of the functions $C(\Theta)$ and $D(\Theta)$:

$$A = \frac{D(\Theta_{\text{tl}})}{C(\Theta_{\text{tl}})}, \tag{D.26a}$$

$$B_z^{\text{fw}} = \frac{\pi}{4}\left[D(\Theta_{\text{cl}}) - AC(\Theta_{\text{cl}})\right], \tag{D.26b}$$

$$B_z^{\text{bw}} = \frac{\pi}{2}D(\Theta_{\text{tl}}). \tag{D.26c}$$

## D.6 Inverse variance weighting

Given $n$ independent Gaussian random variables $X_i$ with $i = 1, 2, \ldots, n$ with identical mean but different variances $\sigma_i^2$, one can find that the weighted average, which minimizes the variance, is given by [77]

$$X = \sigma^2 \sum_{i=1}^{n} \frac{X_i}{\sigma_i^2} \tag{D.27}$$

with

$$\sigma^2 = \left(\sum_{j=1}^{n} \frac{1}{\sigma_j^2}\right)^{-1}. \tag{D.28}$$

We see that $X$ is a random variable with $\langle X \rangle = \langle X_i \rangle$ and $\text{Var}(X) = \sigma^2$.

# E

# SI: Optomechanics in free space

Here we present supplementary information to chapter 5.

## E.1 Symmetrized power spectral density

In the main text, in sections 5.3, 5.4, and 5.5, we derived the correlations of the photocurrent from a heterodyne detector measuring the motion of a vibrating mirror. Following Glauber and Carmichael, we derived the photocurrent statistics in a normally ordered treatment to model the detection process. There is a common alternative way found in literature, where the photocurrent correlations are taken to be the symmetrized version of their quantum mechanical counter parts. In this appendix, we repeat the derivations of chapter 5 using symmetrized correlations. In the following, we point out which equations in the main text need to be adapted in this alternative detection model.

The correlations of the measured photocurrent, Eq. (5.15) and Eq. (5.16),

now read

$$\langle i(t)\rangle = \left\langle \hat{i}(t)\right\rangle_t = \left\langle \hat{a}^\dagger(t)\hat{a}(t)\right\rangle_t, \tag{E.1a}$$

$$\begin{aligned}\bar{G}_{ii}(\tau) &= \frac{1}{2}\left[\left\langle \hat{i}(t+\tau)\hat{i}(t)\right\rangle_t + \left\langle \hat{i}(t)\hat{i}(t+\tau)\right\rangle_t\right] \\ &= \frac{1}{2}\left\langle \hat{a}^\dagger(t+\tau)\hat{a}(t+\tau)\hat{a}^\dagger(t)\hat{a}(t)\right\rangle_t \\ &+ \frac{1}{2}\left\langle \hat{a}^\dagger(t)\hat{a}(t)\hat{a}^\dagger(t+\tau)\hat{a}(t+\tau)\right\rangle_t .\end{aligned} \tag{E.1b}$$

The (symmetrized) photocurrent's correlation function $\bar{G}^{\text{het}}_{ii}(\tau)$ and the spectrum $\bar{S}^{\text{het}}_{ii}(\omega)$ on our heterodyne detector [compare Eqs. (5.22) and (5.23)] now read [94]

$$\begin{aligned}\bar{G}^{\text{het}}_{ii}(\tau) = \frac{|\alpha|^2}{2}\big[&G_{\hat{b}\hat{b}}(\tau)\mathrm{e}^{\mathrm{i}\omega_{\text{LO}}\tau} + G_{\hat{b}^\dagger\hat{b}^\dagger}(\tau)\mathrm{e}^{-\mathrm{i}\omega_{\text{LO}}\tau} \\ &+ G_{\hat{b}\hat{b}}(-\tau)\mathrm{e}^{-\mathrm{i}\omega_{\text{LO}}\tau} + G_{\hat{b}^\dagger\hat{b}^\dagger}(-\tau)\mathrm{e}^{\mathrm{i}\omega_{\text{LO}}\tau}\big],\end{aligned} \tag{E.2a}$$

$$\begin{aligned}\bar{S}^{\text{het}}_{ii}(\omega) = \frac{|\alpha|^2}{2}\big[&S_{\hat{b}\hat{b}}(\omega+\omega_{\text{LO}}) + S_{\hat{b}^\dagger\hat{b}^\dagger}(\omega-\omega_{\text{LO}}) \\ &+ S_{\hat{b}\hat{b}}(-\omega+\omega_{\text{LO}}) + S_{\hat{b}^\dagger\hat{b}^\dagger}(-\omega-\omega_{\text{LO}})\big],\end{aligned} \tag{E.2b}$$

$$\begin{aligned}\bar{S}^{\text{het}}_{ii}(\omega_{\text{LO}}+\omega) = \frac{|\alpha|^2}{2}\big[&S_{\hat{b}\hat{b}}(-\omega) + S_{\hat{b}^\dagger\hat{b}^\dagger}(\omega) \\ &+ S_{\hat{b}\hat{b}}(2\omega_{\text{LO}}+\omega) + S_{\hat{b}^\dagger\hat{b}^\dagger}(-2\omega_{\text{LO}}-\omega)\big].\end{aligned} \tag{E.2c}$$

A detailed derivation can be found in App. E.2. As in Eq. (5.24), we can neglect $S_{\hat{b}\hat{b}}(2\omega_{\text{LO}}+\omega)$ if the LO frequency is chosen large enough. Equally, all non-constant components of $S_{\hat{b}^\dagger\hat{b}^\dagger}(-2\omega_{\text{LO}}-\omega)$ can be neglected, but importantly, this term (due to its anti-normal order) includes a constant, shot-noise term, which cannot be neglected.

Next, we use the reflected mode $\hat{b}_{\text{out}}(t)$ from our vibrating mirror

[Eq. (5.6b)] as an input to our photodetector and find

$$\begin{aligned}\bar{S}_{ii}^{\text{het}}(\omega_{\text{LO}}+\omega) =& \frac{|\alpha|^2}{2}\left[S_{\hat{b}\hat{b}}^{\text{out}}(-\omega)+S_{\hat{b}^\dagger\hat{b}^\dagger}^{\text{out}}(\omega)+S_{\hat{b}^\dagger\hat{b}^\dagger}^{\text{out}}(-2\omega_{\text{LO}}-\omega)\right]\\ =& \frac{|\alpha|^2}{2}\Big[S_{\hat{b}\hat{b}}^{\text{in}}(-\omega)+S_{\hat{b}^\dagger\hat{b}^\dagger}^{\text{in}}(\omega)+S_{\hat{b}^\dagger\hat{b}^\dagger}^{\text{in}}(-2\omega_{\text{LO}}-\omega)\\ &+4\beta^2k^2\left[S_{\hat{x}\hat{x}}(-\omega)+S_{\hat{x}\hat{x}}(\omega)\right]\\ &+4\beta k\text{Im}\left[S_{\hat{b}\hat{x}}^{\text{in}}(-\omega)-S_{\hat{b}^\dagger\hat{x}}^{\text{in}}(\omega)\right]\Big],\end{aligned} \tag{E.3}$$

where we neglected all terms which include the mechanical motion $\hat{x}(t)$ at $2\omega_{\text{LO}}$. The last cross-correlation can be solved in terms of the inputs as

$$S_{\hat{b}^\dagger\hat{x}}^{\text{in}}(\omega) = -2\hbar k\beta\chi[\omega]^*\left[S_{\hat{b}^\dagger\hat{b}^\dagger}^{\text{in}}(\omega)+S_{\hat{b}^\dagger\hat{b}}^{\text{in}}(\omega)\right]. \tag{E.4}$$

All other correlations are given in the main text [Eqs. (5.8) and following] and we find

$$\begin{aligned}\bar{S}_{ii}^{\text{het}}(\omega_{\text{LO}}+\omega) = \frac{|\alpha|^2}{2\pi}\Bigg[1+\overbrace{4\hbar\beta^2k^2\text{Im}\,\chi[\omega]^*}^{-4\pi\beta k\text{Im}\,S_{\hat{b}^\dagger\hat{x}}^{\text{in}}(\omega)}\\ +8\pi\beta^2k^2\overbrace{|\chi[\omega]|^2\left(\left[S_{\hat{F}\hat{F}}^{\text{th}}(\omega)+S_{\hat{F}\hat{F}}^{\text{th}}(-\omega)\right]/2+2\hbar^2k^2\beta^2/\pi\right)}^{[S_{\hat{x}\hat{x}}(\omega)+S_{\hat{x}\hat{x}}(-\omega)]/2}\Bigg].\end{aligned} \tag{E.5}$$

Clearly, the asymmetric spectrum of the force correlations vanishes in this expression and in fact, any asymmetry in $S_{\hat{x}\hat{x}}(\omega)$ *cannot* be probed. However, there is an additional non-vanishing term containing correlations between the input light field and the motion $S_{\hat{b}^\dagger\hat{x}}^{\text{in}}(\omega)$ due to the probe light driving the motion. The implications of these findings are discussed in the main text.

## E.2 Derivation of Eq. (5.21b) and Eq. (E.2a)

In this appendix, we find the photocurrent autocorrelation function $G_{ii}(\tau)$ [Eq. (5.21b)] in terms of the input field $\hat{b}(t)$ by inserting Eqs. (5.18) into

Eq. (5.19b). For this, we first note that we can write Eqs. (5.18) as

$$\begin{aligned}\hat{i}_1(t) &= A + B,\\ \hat{i}_2(t) &= A - B\end{aligned} \tag{E.6}$$

with

$$\begin{aligned}2A &= \hat{b}^\dagger\hat{b} + \hat{\alpha}^\dagger\hat{\alpha},\\ 2B &= \hat{b}^\dagger\hat{\alpha} + \hat{\alpha}^\dagger\hat{b},\end{aligned} \tag{E.7}$$

where we dropped the time arguments. Now we will write the following current-current operators in terms of $A$ and $B$:

$$\begin{aligned}\hat{i}_1(t+\tau)\hat{i}_1(t) &= A_\tau A + B_\tau B + A_\tau B + B_\tau A,\\ \hat{i}_2(t+\tau)\hat{i}_2(t) &= A_\tau A + B_\tau B - A_\tau B - B_\tau A,\\ \hat{i}_1(t+\tau)\hat{i}_2(t) &= A_\tau A - B_\tau B - A_\tau B + B_\tau A,\\ \hat{i}_2(t+\tau)\hat{i}_1(t) &= A_\tau A - B_\tau B + A_\tau B - B_\tau A.\end{aligned} \tag{E.8}$$

The subscript $_\tau$ abbreviates a time delay of the argument by $\tau$, *i.e.*, $A_\tau = A(t+\tau)$. Now we can solve for the difference-current autocorrelation operator $\hat{G}_{ii}(\tau)$ assuming $\hat{\alpha}$ and $\hat{b}$ to be independent:

$$\begin{aligned}\hat{G}_{ii}(\tau) =& \hat{i}_1(t+\tau)\hat{i}_1(t) + \hat{i}_2(t+\tau)\hat{i}_2(t)\\ &- \hat{i}_1(t+\tau)\hat{i}_2(t) - \hat{i}_2(t+\tau)\hat{i}_1(t)\\ =& 4B_\tau B\\ =& \hat{b}_\tau^\dagger\hat{b}\hat{\alpha}_\tau\hat{\alpha}^\dagger + \hat{b}_\tau\hat{b}^\dagger\hat{\alpha}_\tau^\dagger\hat{\alpha} + \hat{b}_\tau^\dagger\hat{b}^\dagger\hat{\alpha}_\tau\hat{\alpha} + \hat{b}_\tau\hat{b}\hat{\alpha}_\tau^\dagger\hat{\alpha}^\dagger.\end{aligned} \tag{E.9}$$

Assuming that the photocurrent's autocorrelation function is given as the normal- and time-ordered version of $\hat{G}_{ii}(\tau)$ as detailed in chapter 5, we find

$$\begin{aligned} G_{ii}(\tau) =& \left\langle : \hat{G}_{ii}(\tau) : \right\rangle + \delta(\tau) \left\langle : \hat{i}_1(t) + \hat{i}_2(t) : \right\rangle \\ =& 4 \left\langle : B_\tau B : \right\rangle + 2 \left\langle : A : \right\rangle \delta(\tau) \\ =& \left\langle \hat{b}_\tau^\dagger \hat{b} \right\rangle \left\langle \hat{\alpha}^\dagger \hat{\alpha}_\tau \right\rangle + \left\langle \hat{b}^\dagger \hat{b}_\tau \right\rangle \left\langle \hat{\alpha}_\tau^\dagger \hat{\alpha} \right\rangle + \left\langle \hat{b}^\dagger \hat{b}_\tau^\dagger \right\rangle \langle \hat{\alpha}_\tau \hat{\alpha} \rangle \\ &+ \left\langle \hat{b}_\tau \hat{b} \right\rangle \left\langle \hat{\alpha}^\dagger \hat{\alpha}_\tau^\dagger \right\rangle + \left( \left\langle \hat{b}^\dagger \hat{b} \right\rangle + \left\langle \hat{\alpha}^\dagger \hat{\alpha} \right\rangle \right) \delta(\tau), \end{aligned} \tag{E.10}$$

where we assumed $\tau > 0$ for time ordering. Next, we assume $\hat{\alpha}$ to be a coherent field with $\hat{\alpha} |\psi\rangle = \alpha e^{i\omega_{LO} t} |\psi\rangle$ like in the main text. We are in a rotating frame at the optical frequency $\omega_L$, such that all operators have an additional phase factor $e^{-i\omega_L t}$ in the real frame, which we skip. With this, we find Eq. (5.21b):

$$\begin{aligned} G_{ii}(\tau) = |\alpha|^2 G_{\hat{b}\hat{b}}(\tau) e^{i\omega_{LO}\tau} + |\alpha|^2 G_{\hat{b}\hat{b}}(-\tau) e^{-i\omega_{LO}\tau} + \left( \left\langle \hat{b}^\dagger \hat{b} \right\rangle + |\alpha|^2 \right) \delta(\tau) \\ + \alpha^2 G_{\hat{b}\hat{b}^\dagger}(-|\tau|) \left\langle e^{i\omega_{LO}(2t+\tau)} \right\rangle_t + (\alpha^*)^2 G_{\hat{b}^\dagger \hat{b}}(|\tau|) \left\langle e^{-i\omega_{LO}(2t+\tau)} \right\rangle_t \end{aligned} \tag{E.11}$$

Note that for a heterodyne detector where $\omega_{LO} \neq 0$, the third and forth term vanish due to averaging in time. For a homodyne detector with $\omega_{LO} = 0$, however, they do not vanish. The absolute value operator that appears in the third and forth terms results from time ordering.

In contrast to the normally ordered treatment above, in App. E.1 we use the symmetrized version of the correlation function. In this case, we find $\bar{G}_{ii}^{\text{het}}(\tau)$ [Eq. (E.2a)]:

$$\begin{aligned} \bar{G}_{ii}^{\text{het}}(\tau) =& \frac{1}{2} \left\langle \hat{G}_{ii}(\tau) + \hat{G}_{ii}(-\tau) \right\rangle \\ =& \frac{1}{2} \left\langle \hat{b}_\tau^\dagger \hat{b} \hat{\alpha}_\tau \hat{\alpha}^\dagger + \hat{b}_\tau \hat{b}^\dagger \hat{\alpha}_\tau^\dagger \hat{\alpha} + \hat{b}_\tau^\dagger \hat{b}^\dagger \hat{\alpha}_\tau \hat{\alpha} + \hat{b}_\tau \hat{b} \hat{\alpha}_\tau^\dagger \hat{\alpha}^\dagger \right\rangle \\ &+ \frac{1}{2} \left\langle \hat{b}^\dagger \hat{b}_\tau \hat{\alpha} \hat{\alpha}_\tau^\dagger + \hat{b} \hat{b}_\tau^\dagger \hat{\alpha}^\dagger \hat{\alpha}_\tau + \hat{b}^\dagger \hat{b}_\tau^\dagger \hat{\alpha} \hat{\alpha}_\tau + \hat{b} \hat{b}_\tau \hat{\alpha}^\dagger \hat{\alpha}_\tau^\dagger \right\rangle \\ =& \frac{|\alpha|^2}{2} \left[ G_{\hat{b}\hat{b}}(\tau) e^{i\omega_{LO}\tau} + G_{\hat{b}^\dagger \hat{b}^\dagger}(\tau) e^{-i\omega_{LO}\tau} \right. \\ &\left. + G_{\hat{b}\hat{b}}(-\tau) e^{-i\omega_{LO}\tau} + G_{\hat{b}^\dagger \hat{b}^\dagger}(-\tau) e^{i\omega_{LO}\tau} \right] + \delta(\tau) \left\langle \hat{b}^\dagger \hat{b} \right\rangle. \end{aligned} \tag{E.12}$$

We assumed heterodyne detection ($\omega_{\mathrm{LO}} \neq 0$) and we averaged over oscillations of the type $\mathrm{e}^{\pm 2\mathrm{i}\omega_{\mathrm{LO}}t}$. We also assumed $\hat{\alpha}$ and $\hat{b}$ to be independent and used the fact $\left\langle \hat{\alpha}_\tau \hat{\alpha}^\dagger \right\rangle = \delta(\tau) + \left\langle \hat{\alpha}^\dagger \hat{\alpha}_\tau \right\rangle$. Note that in general, a similar equation is not true for $\hat{b}$. For a strong reference $\hat{\alpha}$, the last term $\delta(\tau) \left\langle \hat{b}^\dagger \hat{b} \right\rangle$ is much smaller than the other terms and can be neglected.

## E.3 Homodyne detection

For completeness, let us now turn to a homodyne detector, for which $\omega_{\mathrm{LO}} = 0$ in Eq. (E.11). Furthermore we write $\alpha = |\alpha| \mathrm{e}^{\mathrm{i}\theta}$, where $\theta$ is called the analyzer angle. We now find

$$\langle i_{\mathrm{hom}}(t) \rangle = |\alpha| \left( \mathrm{e}^{-\mathrm{i}\theta} \left\langle \hat{b}(t) \right\rangle + \mathrm{e}^{\mathrm{i}\theta} \left\langle \hat{b}^\dagger(t) \right\rangle \right) \tag{E.13a}$$

$$\begin{aligned} G_{ii}^{\mathrm{hom}}(\tau) = |\alpha|^2 \big[ & \delta(\tau) + G_{\hat{b}\hat{b}}(\tau) + G_{\hat{b}\hat{b}}(-\tau) \\ & + \mathrm{e}^{2\mathrm{i}\theta} G_{\hat{b}\hat{b}^\dagger}(-|\tau|) + \mathrm{e}^{-2\mathrm{i}\theta} G_{\hat{b}^\dagger\hat{b}}(|\tau|) \big] \end{aligned} \tag{E.13b}$$

$$\begin{aligned} S_{ii}^{\mathrm{hom}}(\omega) = |\alpha|^2 \Big[ & \frac{1}{2\pi} + S_{\hat{b}\hat{b}}(\omega) + S_{\hat{b}\hat{b}}(-\omega) \\ & + \mathrm{e}^{2\mathrm{i}\theta} S_{\hat{b}^\dagger\hat{b}}(-\omega)^* + \mathrm{e}^{-2\mathrm{i}\theta} S_{\hat{b}^\dagger\hat{b}}(\omega) \Big] \end{aligned} \tag{E.13c}$$

From Eq.(E.13b) to Eq. (E.13c) we tacitly assumed that $G_{\hat{b}^\dagger\hat{b}}(|\tau|) = G_{\hat{b}^\dagger\hat{b}}(\tau)$ such that their Fourier transform $S_{\hat{b}^\dagger\hat{b}}(\omega)$ is even. Later we plug $S_{\hat{b}^\dagger\hat{b}}^{\mathrm{out}}(\omega)$ into this equation, which indeed is an even function, see Eq. (E.15). As expected, this spectrum is symmetric in frequency and any asymmetry of $S_{\hat{b}\hat{b}}(\omega)$ cannot be seen.

In analogy to Sec. 5.5, we now send the reflected probe light $\hat{b}_{\mathrm{out}}(t)$ of a vibrating mirror to the homodyne detector. From the main text, we know

$$S_{\hat{b}\hat{b}}^{\mathrm{out}}(\omega) = 4\beta^2 k^2 S_{\hat{x}\hat{x}}(\omega). \tag{E.14}$$

Using the input-output relations [Eqs. (5.6)], we furthermore find

$$\begin{aligned} S^{\text{out}}_{\hat{b}^\dagger\hat{b}}(\omega) &= S^{\text{in}}_{\hat{b}^\dagger\hat{b}}(\omega) - 4\beta^2k^2S_{\hat{x}\hat{x}}(\omega) - 2\mathrm{i}\beta k\left[S^{\text{in}}_{\hat{b}^\dagger\hat{x}}(\omega) + S^{\text{in}}_{\hat{x}\hat{b}}(\omega)\right] \\ &= -4\beta^2k^2S_{\hat{x}\hat{x}}(\omega) + \frac{2\mathrm{i}\hbar}{\pi}\beta^2k^2\chi[\omega]^* \\ &= -4\beta^2k^2\frac{S_{\hat{x}\hat{x}}(\omega) + S_{\hat{x}\hat{x}}(-\omega)}{2} + \frac{2\mathrm{i}\hbar}{\pi}\beta^2k^2\mathrm{Re}\,\chi[\omega]. \end{aligned} \tag{E.15}$$

where we used Eqs. (5.10) for the input correlations and $\chi[-\omega] = \chi[\omega]^*$. For the last identity, which proves that $S^{\text{out}}_{\hat{b}^\dagger\hat{b}}(\omega) = S^{\text{out}}_{\hat{b}^\dagger\hat{b}}(-\omega)$ is an even function, we used

$$\frac{S_{\hat{x}\hat{x}}(\omega) - S_{\hat{x}\hat{x}}(-\omega)}{2} = |\chi[\omega]|^2\frac{m\gamma\hbar\omega}{2\pi} = \frac{\hbar}{2\pi}\mathrm{Im}\,\chi[\omega]. \tag{E.16}$$

Let us further analyze the homodyne detection by fixing the analyzer angle to $\theta = \pi/2$. This makes the detector phase sensitive, since then $i_{\text{hom}}(t) \propto \mathrm{i}[\hat{b}^\dagger(t) - \hat{b}(t)]$. The homodyne PSD then becomes

$$S^{\text{hom}}_{ii}(\omega) = c^2_{\text{hom}}\left[S^{\text{hom}}_{\text{imp}} + \frac{S_{\hat{x}\hat{x}}(\omega) + S_{\hat{x}\hat{x}}(-\omega)}{2}\right], \tag{E.17}$$

where $S^{\text{hom}}_{\text{imp}} = 1/(32\pi\beta^2k^2)$ is the imprecision noise of the homodyne detector with unit detection efficiency and $c_{\text{hom}} = 4|\alpha|\beta k$ is the calibration factor. Our homodyne detector thus measures the symmetrized position PSD $[S_{\hat{x}\hat{x}}(\omega) + S_{\hat{x}\hat{x}}(-\omega)]/2$, as expected. In the main text we show that this detector operates at the Heisenberg limit of the imprecision-backaction product.

## E.4 Inefficient detection

In chapter 5, we derived models for a heterodyne and a homodyne detection scheme of a vibrating mirror in Eq. (5.25) and Eq. (E.17). For the derivation, we assumed unity detection efficiency, which is typically not given in the lab. Specifically, in levitated optomechanics we show in Ch. 3, that detecting a specific direction of motion of the particle is associated with a detection inefficiency due to the finite NA of the trapping optic and a non-ideal mode overlap. Here, we enrich the framework developed in Ch. 5 by introducing a

detection efficiency $\eta_d < 1$. For this, we attenuate the signal mode $\hat{b}(t)$ (see Fig. 5.2), which we model by a beamsplitter with transmission coefficient $\eta_d$. The new mode $\hat{c}(t)$ at the input of the 50:50 beamsplitter then reads

$$\hat{c}(t) = \sqrt{\eta_d}\hat{b}(t) + \sqrt{1-\eta_d}\hat{b}_{\text{vac}}(t), \tag{E.18}$$

where $\hat{b}_{\text{vac}}(t)$ are inevitable vacuum fluctuations [66]. These vacuum fluctuations are independent of the input mode $\hat{b}(t)$, and we find for the PSD of the new input mode $\hat{c}(t)$:

$$S_{\hat{c}\hat{c}}(\omega) = \eta_d S_{\hat{b}\hat{b}}(\omega) + (1-\eta_d)S^{\text{vac}}_{\hat{b}\hat{b}}(\omega) = \eta_d S_{\hat{b}\hat{b}}(\omega). \tag{E.19}$$

In Eqs. (5.10) we explicitly found $S^{\text{vac}}_{\hat{b}\hat{b}}(\omega) = 0$ for vacuum fluctuations. The effect of inefficiency on the spectra obtained by homodyne (heterodyne) detection is that the imprecision noise $S^{\text{hom}}_{\text{imp}}$ ($S^{\text{het}}_{\text{imp}}$) is increased by $1/\eta_d$ and (less importantly) the calibration factor $c_{\text{hom}}$ ($c_{\text{het}}$) is decreased by $\sqrt{\eta_d}$. We find [Compare to Eq. (5.25) and Eq. (E.17)]

$$\begin{aligned} S^{\text{hom},\eta_d}_{\text{imp}} &= (32\pi\beta^2 k^2 \eta_d)^{-1}, \\ S^{\text{het},\eta_d}_{\text{imp}} &= (8\pi\beta^2 k^2 \eta_d)^{-1}. \end{aligned} \tag{E.20}$$

# References


[1] B. P. Abbott *et al.* (LIGO Scientific and Virgo Collaborations), *Observation of Gravitational Waves from a Binary Black Hole Merger*, Phys. Rev. Lett. **116**, 061102 (2016).

[2] P. J. Mohr, D. B. Newell, and B. N. Taylor, *CODATA recommended values of the fundamental physical constants: 2014*, Rev. Mod. Phys. **88**, 035009 (2016).

[3] A. Ashkin, *Acceleration and Trapping of Particles by Radiation Pressure*, Phys. Rev. Lett. **24**, 156 (1970).

[4] A. Ashkin, *Applications of Laser Radiation Pressure*, Science **210**, 1081 (1980).

[5] W. D. Phillips, *Nobel Lecture: Laser cooling and trapping of neutral atoms*, Rev. Mod. Phys. **70**, 721 (1998).

[6] A. Ashkin, *Optical Trapping and Manipulation of Neutral Particles Using Lasers* (World Scientific, Singapore, 2006).

[7] V. B. Braginsky and F. Y. Khalili, *Quantum Measurement* (Cambridge University, Cambridge, England, 1992).

[8] J. Teufel, T. Donner, M. Castellanos-Beltran, J. Harlow, and K. Lehnert, *Nanomechanical motion measured with an imprecision below that at the standard quantum limit*, Nat. Nanotechnol. **4**, 820 (2009).

[9] G. Anetsberger, E. Gavartin, O. Arcizet, Q. P. Unterreithmeier, E. M. Weig, M. L. Gorodetsky, J. P. Kotthaus, and T. J. Kippenberg, *Measuring nanomechanical motion with an imprecision below the standard quantum limit*, Phys. Rev. A **82**, 061804(R) (2010).

[10] P. Verlot, A. Tavernarakis, T. Briant, P.-F. Cohadon, and A. Heidmann, *Backaction Amplification and Quantum Limits in Optomechanical Measurements*, Phys. Rev. Lett. **104**, 133602 (2010).

[11] T. P. Purdy, R. W. Peterson, and C. A. Regal, *Observation of Radiation Pressure Shot Noise on a Macroscopic Object*, Science **339**, 801 (2013).

[12] M. Aspelmeyer, T. J. Kippenberg, and F. Marquardt, *Cavity optomechanics*, Rev. Mod. Phys. **86**, 1391 (2014).

[13] A. Ashkin and J. M. Dziedzic, *Feedback stabilization of optically levitated particles*, Appl. Phys. Lett. **30**, 202 (1977).

[14] A. Ashkin, J. M. Dziedzic, J. E. Bjorkholm, and S. Chu, *Observation of a single-beam gradient force optical trap for dielectric particles*, Opt. Lett. **11**, 288 (1986).

[15] T. Li, S. Kheifets, and M. G. Raizen, *Millikelvin cooling of an optically trapped microsphere in vacuum*, Nat. Phys. **7**, 527 (2011).

[16] D. E. Chang, C. A. Regal, S. B. Papp, D. J. Wilson, J. Ye, O. Painter, H. J. Kimble, and P. Zoller, *Cavity opto-mechanics using an optically levitated nanosphere*, Proc. Natl. Acad. Sci. U.S.A. **107**, 1005 (2010).

[17] O. Romero-Isart, A. C. Pflanzer, M. L. Juan, R. Quidant, N. Kiesel, M. Aspelmeyer, and J. I. Cirac, *Optically levitating dielectrics in the quantum regime: Theory and protocols*, Phys. Rev. A **83**, 013803 (2011).

[18] J. Gieseler, B. Deutsch, R. Quidant, and L. Novotny, *Subkelvin Parametric Feedback Cooling of a Laser-Trapped Nanoparticle*, Phys. Rev. Lett. **109**, 103603 (2012).

[19] Z. Yin, A. A. Geraci, and T. Li, *Optomechanics of levitated dielectric particles*, Int. J. Mod. Phys. B **27**, 1330018 (2013).

[20] B. Rodenburg, L. P. Neukirch, A. N. Vamivakas, and M. Bhattacharya, *Quantum model of cooling and force sensing with an optically trapped nanoparticle*, Optica **3**, 318 (2016).

[21] A. A. Geraci, S. B. Papp, and J. Kitching, *Short-Range Force Detection Using Optically Cooled Levitated Microspheres*, Phys. Rev. Lett. **105**, 101101 (2010).

[22] A. Arvanitaki and A. A. Geraci, *Detecting High-Frequency Gravitational Waves with Optically Levitated Sensors*, Phys. Rev. Lett. **110**, 071105 (2013).

[23] D. C. Moore, A. D. Rider, and G. Gratta, *Search for Millicharged Particles Using Optically Levitated Microspheres*, Phys. Rev. Lett. **113**, 251801 (2014).

[24] A. D. Rider, D. C. Moore, C. P. Blakemore, M. Louis, M. Lu, and G. Gratta, *Search for Screened Interactions Associated with Dark Energy below the* $100\ \mu\mathrm{m}$ *Length Scale*, Phys. Rev. Lett. **117**, 101101 (2016).

[25] O. Romero-Isart, A. C. Pflanzer, F. Blaser, R. Kaltenbaek, N. Kiesel, M. Aspelmeyer, and J. I. Cirac, *Large Quantum Superpositions and Interference of Massive Nanometer-Sized Objects*, Phys. Rev. Lett. **107**, 020405 (2011).

[26] O. Romero-Isart, *Quantum superposition of massive objects and collapse models*, Phys. Rev. A **84**, 052121 (2011).

[27] J. Chan, T. M. Alegre, A. H. Safavi-Naeini, J. T. Hill, A. Krause, S. Gröblacher,

M. Aspelmeyer, and O. Painter, *Laser cooling of a nanomechanical oscillator into its quantum ground state*, Nature (London) **478**, 89 (2011).

[28] J. D. Teufel, T. Donner, D. Li, J. W. Harlow, M. S. Allman, K. Cicak, A. J. Sirois, J. D. Whittaker, K. W. Lehnert, and R. W. Simmonds, *Sideband cooling of micromechanical motion to the quantum ground state*, Nature (London) **475**, 359 (2011).

[29] M. Rossi, D. Mason, J. Chen, Y. Tsaturyan, and A. Schliesser, *Measurement-based quantum control of mechanical motion*, Nature (London) **563**, 53 (2018).

[30] N. Kiesel, F. Blaser, U. Delić, D. Grass, R. Kaltenbaek, and M. Aspelmeyer, *Cavity cooling of an optically levitated submicron particle*, Proc. Natl. Acad. Sci. U.S.A. **110**, 14180 (2013).

[31] J. Millen, P. Z. G. Fonseca, T. Mavrogordatos, T. S. Monteiro, and P. F. Barker, *Cavity Cooling a Single Charged Levitated Nanosphere*, Phys. Rev. Lett. **114**, 123602 (2015).

[32] P. Z. G. Fonseca, E. B. Aranas, J. Millen, T. S. Monteiro, and P. F. Barker, *Nonlinear Dynamics and Strong Cavity Cooling of Levitated Nanoparticles*, Phys. Rev. Lett. **117**, 173602 (2016).

[33] U. Delić, M. Reisenbauer, D. Grass, N. Kiesel, V. Vuletić, and M. Aspelmeyer, *Cavity Cooling of a Levitated Nanosphere by Coherent Scattering*, Phys. Rev. Lett. **122**, 123602 (2019).

[34] D. Windey, C. Gonzalez-Ballestero, P. Maurer, L. Novotny, O. Romero-Isart, and R. Reimann, *Cavity-Based 3D Cooling of a Levitated Nanoparticle via Coherent Scattering*, Phys. Rev. Lett. **122**, 123601 (2019).

[35] N. Meyer, A. d. l. R. Sommer, P. Mestres, J. Gieseler, V. Jain, L. Novotny, and R. Quidant, *Resolved-Sideband Cooling of a Levitated Nanoparticle in the Presence of Laser Phase Noise*, Phys. Rev. Lett. **123**, 153601 (2019).

[36] U. Delić, M. Reisenbauer, K. Dare, D. Grass, V. Vuletić, N. Kiesel, and M. Aspelmeyer, *Cooling of a levitated nanoparticle to the motional quantum ground state*, Science **367**, 892 (2020).

[37] G. Ranjit, D. P. Atherton, J. H. Stutz, M. Cunningham, and A. A. Geraci, *Attonewton force detection using microspheres in a dual-beam optical trap in high vacuum*, Phys. Rev. A **91**, 051805(R) (2015).

[38] G. Ranjit, M. Cunningham, K. Casey, and A. A. Geraci, *Zeptonewton force sensing with nanospheres in an optical lattice*, Phys. Rev. A **93**, 053801 (2016).

[39] J. Vovrosh, M. Rashid, D. Hempston, J. Bateman, M. Paternostro, and H. Ulbricht, *Parametric feedback cooling of levitated optomechanics in a parabolic mirror trap*, J. Opt. Soc. Am. B **34**, 1421 (2017).

[40] A. Setter, M. Toroš, J. F. Ralph, and H. Ulbricht, *Real-time Kalman filter:*

*Cooling of an optically levitated nanoparticle*, Phys. Rev. A **97**, 033822 (2018).

[41] V. Jain, J. Gieseler, C. Moritz, C. Dellago, R. Quidant, and L. Novotny, *Direct Measurement of Photon Recoil from a Levitated Nanoparticle*, Phys. Rev. Lett. **116**, 243601 (2016).

[42] L. Novotny and B. Hecht, *Principles of Nano-Optics* (Cambridge University, Cambridge, England, 2012).

[43] J. Gieseler, *Dynamics of optically levitated nanoparticles in high vacuum*, Ph.D. thesis, ICFO Barcelona (2014).

[44] E. Hebestreit, *Thermal Properties of Levitated Nanoparticles*, Ph.D. thesis, ETH Zürich (2017).

[45] R. Diehl, *Nanoparticle Levitation for the Study of Short-range Interactions*, Ph.D. thesis, ETH Zürich (2018).

[46] V. Jain, *Levitated Optomechanics at the Photon Recoil Limit*, Ph.D. thesis, ETH Zürich (2017).

[47] P. F. Cohadon, A. Heidmann, and M. Pinard, *Cooling of a Mirror by Radiation Pressure*, Phys. Rev. Lett. **83**, 3174 (1999).

[48] M. Poggio, C. L. Degen, H. J. Mamin, and D. Rugar, *Feedback Cooling of a Cantilever's Fundamental Mode below 5 mK*, Phys. Rev. Lett. **99**, 017201 (2007).

[49] D. Wilson, V. Sudhir, N. Piro, R. Schilling, A. Ghadimi, and T. J. Kippenberg, *Measurement-based control of a mechanical oscillator at its thermal decoherence rate*, Nature (London) **524**, 325 (2015).

[50] V. Steixner, P. Rabl, and P. Zoller, *Quantum feedback cooling of a single trapped ion in front of a mirror*, Phys. Rev. A **72**, 043826 (2005).

[51] P. Bushev, D. Rotter, A. Wilson, F. Dubin, C. Becher, J. Eschner, R. Blatt, V. Steixner, P. Rabl, and P. Zoller, *Feedback Cooling of a Single Trapped Ion*, Phys. Rev. Lett. **96**, 043003 (2006).

[52] S. Mancini, D. Vitali, and P. Tombesi, *Optomechanical Cooling of a Macroscopic Oscillator by Homodyne Feedback*, Phys. Rev. Lett. **80**, 688 (1998).

[53] M. Frimmer, K. Luszcz, S. Ferreiro, V. Jain, E. Hebestreit, and L. Novotny, *Controlling the net charge on a nanoparticle optically levitated in vacuum*, Phys. Rev. A **95**, 061801(R) (2017).

[54] M. Iwasaki, T. Yotsuya, T. Naruki, Y. Matsuda, M. Yoneda, and K. Aikawa, *Electric feedback cooling of single charged nanoparticles in an optical trap*, Phys. Rev. A **99**, 051401(R) (2019).

[55] J. Gieseler, M. Spasenović, L. Novotny, and R. Quidant, *Nonlinear Mode Coupling and Synchronization of a Vacuum-Trapped Nanoparticle*, Phys. Rev. Lett. **112**, 103603 (2014).

[56] E. Hebestreit, M. Frimmer, R. Reimann, C. Dellago, F. Ricci, and L. Novotny, *Calibration and energy measurement of optically levitated nanoparticle sensors*, Rev. Sci. Instr. **89**, 033111 (2018).

[57] M. Pinard, P. Cohadon, T. Briant, and A. Heidmann, *Full mechanical characterization of a cold damped mirror*, Phys. Rev. A **63**, 013808 (2000).

[58] F. Tebbenjohanns, M. Frimmer, A. Militaru, V. Jain, and L. Novotny, *Cold Damping of an Optically Levitated Nanoparticle to Microkelvin Temperatures*, Phys. Rev. Lett. **122**, 223601 (2019).

[59] A. A. Clerk, M. H. Devoret, S. M. Girvin, F. Marquardt, and R. J. Schoelkopf, *Introduction to quantum noise, measurement, and amplification*, Rev. Mod. Phys. **82**, 1155 (2010).

[60] C. Genes, D. Vitali, P. Tombesi, S. Gigan, and M. Aspelmeyer, *Ground-state cooling of a micromechanical oscillator: Comparing cold damping and cavity-assisted cooling schemes*, Phys. Rev. A **77**, 033804 (2008).

[61] H. Habibi, E. Zeuthen, M. Ghanaatshoar, and K. Hammerer, *Quantum feedback cooling of a mechanical oscillator using variational measurements: tweaking Heisenberg's microscope*, J. Opt. **18**, 084004 (2016).

[62] S. Kuhn, G. Wachter, F.-F. Wieser, J. Millen, M. Schneider, J. Schalko, U. Schmid, M. Trupke, and M. Arndt, *Nanoparticle detection in an open-access silicon microcavity*, Appl. Phys. Lett. **111**, 253107 (2017).

[63] G. P. Conangla, F. Ricci, M. T. Cuairan, A. W. Schell, N. Meyer, and R. Quidant, *Optimal Feedback Cooling of a Charged Levitated Nanoparticle with Adaptive Control*, Phys. Rev. Lett. **122**, 223602 (2019).

[64] C. M. Caves, *Quantum-Mechanical Radiation-Pressure Fluctuations in an Interferometer*, Phys. Rev. Lett. **45**, 75 (1980).

[65] C. M. Caves and G. J. Milburn, *Quantum-mechanical model for continuous position measurements*, Phys. Rev. A **36**, 5543 (1987).

[66] W. Bowen and G. Milburn, *Quantum Optomechanics* (Taylor & Francis, Milton, England, 2015).

[67] J. D. Teufel, F. Lecocq, and R. W. Simmonds, *Overwhelming Thermomechanical Motion with Microwave Radiation Pressure Shot Noise*, Phys. Rev. Lett. **116**, 013602 (2016).

[68] R. W. Peterson, T. P. Purdy, N. S. Kampel, R. W. Andrews, P.-L. Yu, K. W. Lehnert, and C. A. Regal, *Laser Cooling of a Micromechanical Membrane to the Quantum Backaction Limit*, Phys. Rev. Lett. **116**, 063601 (2016).

[69] F. Gittes and C. F. Schmidt, *Interference model for back-focal-plane displacement detection in optical tweezers*, Opt. Lett. **23**, 7 (1998).

[70] C. Dawson and J. Bateman, *Spectral analysis and parameter estimation in*

*levitated optomechanics*, J. Opt. Soc. Am. B **36**, 1565 (2019).

[71] S. Qamar, S.-Y. Zhu, and M. S. Zubairy, *Atom localization via resonance fluorescence*, Phys. Rev. A **61**, 063806 (2000).

[72] V. Vuletić, H. W. Chan, and A. T. Black, *Three-dimensional cavity Doppler cooling and cavity sideband cooling by coherent scattering*, Phys. Rev. A **64**, 033405 (2001).

[73] K. W. Murch, K. L. Moore, S. Gupta, and D. M. Stamper-Kurn, *Observation of quantum-measurement backaction with an ultracold atomic gas*, Nat. Phys. **4**, 561 (2008).

[74] M. Koch, C. Sames, A. Kubanek, M. Apel, M. Balbach, A. Ourjoumtsev, P. W. H. Pinkse, and G. Rempe, *Feedback Cooling of a Single Neutral Atom*, Phys. Rev. Lett. **105**, 173003 (2010).

[75] W. Schottky, *Über spontane Stromschwankungen in verschiedenen Elektrizitätsleitern*, Ann. Phys. **362**, 541 (1918).

[76] J. P. Gordon and A. Ashkin, *Motion of atoms in a radiation trap*, Phys. Rev. A **21**, 1606 (1980).

[77] T. Strutz, *Data Fitting and Uncertainty: A practical introduction to weighted least squares and beyond* (Vieweg+Teubner, Wiesbaden, Germany, 2010).

[78] M. Planck, *Zur Theorie der Wärmestrahlung*, Ann. Phys. **336**, 758 (1910).

[79] W. Heisenberg, *Über quantentheoretische Umdeutung kinematischer und mechanischer Beziehungen.*, Z. Phys. **33**, 879 (1925).

[80] C. Cohen-Tannoudji, B. Diu, and F. Laloe, *Quantum Mechanics*, Quantum Mechanics Vol. 1 (Wiley, Hoboken, 1991).

[81] B. J. Kip and R. J. Meier, *Determination of the Local Temperature at a Sample during Raman Experiments Using Stokes and Anti-Stokes Raman Bands*, Appl. Spectrosc. **44**, 707 (1990).

[82] J. B. Cui, K. Amtmann, J. Ristein, and L. Ley, *Noncontact temperature measurements of diamond by Raman scattering spectroscopy*, J. Appl. Phys. **83**, 7929 (1998).

[83] A. Ukil, H. Braendle, and P. Krippner, *Distributed Temperature Sensing: Review of Technology and Applications*, IEEE Sens. J. **12**, 885 (2012).

[84] F. Diedrich, J. C. Bergquist, W. M. Itano, and D. J. Wineland, *Laser Cooling to the Zero-Point Energy of Motion*, Phys. Rev. Lett. **62**, 403 (1989).

[85] P. S. Jessen, C. Gerz, P. D. Lett, W. D. Phillips, S. L. Rolston, R. J. C. Spreeuw, and C. I. Westbrook, *Observation of quantized motion of Rb atoms in an optical field*, Phys. Rev. Lett. **69**, 49 (1992).

[86] C. Monroe, D. M. Meekhof, B. E. King, S. R. Jefferts, W. M. Itano, D. J. Wineland, and P. Gould, *Resolved-Sideband Raman Cooling of a Bound Atom*

*to the 3D Zero-Point Energy*, Phys. Rev. Lett. **75**, 4011 (1995).

[87] A. D. O'Connell, M. Hofheinz, M. Ansmann, R. C. Bialczak, M. Lenander, E. Lucero, M. Neeley, D. Sank, H. Wang, M. Weides, J. Wenner, J. M. Martinis, and A. N. Cleland, *Quantum ground state and single-phonon control of a mechanical resonator*, Nature (London) **464**, 697 (2010).

[88] V. B. Braginsky and A. B. Manukin, *Measurement of Weak Forces in Physics Experiments*, edited by D. H. Douglass (University of Chicago Press, Chicago, 1977).

[89] C. M. Caves, K. S. Thorne, R. W. P. Drever, V. D. Sandberg, and M. Zimmermann, *On the measurement of a weak classical force coupled to a quantum-mechanical oscillator. I. Issues of principle*, Rev. Mod. Phys. **52**, 341 (1980).

[90] A. H. Safavi-Naeini, J. Chan, J. T. Hill, T. P. M. Alegre, A. Krause, and O. Painter, *Observation of Quantum Motion of a Nanomechanical Resonator*, Phys. Rev. Lett. **108**, 033602 (2012).

[91] A. J. Weinstein, C. U. Lei, E. E. Wollman, J. Suh, A. Metelmann, A. A. Clerk, and K. C. Schwab, *Observation and Interpretation of Motional Sideband Asymmetry in a Quantum Electromechanical Device*, Phys. Rev. X **4**, 041003 (2014).

[92] T. P. Purdy, P.-L. Yu, N. S. Kampel, R. W. Peterson, K. Cicak, R. W. Simmonds, and C. A. Regal, *Optomechanical Raman-ratio thermometry*, Phys. Rev. A **92**, 031802(R) (2015).

[93] M. Underwood, D. Mason, D. Lee, H. Xu, L. Jiang, A. B. Shkarin, K. Børkje, S. M. Girvin, and J. G. E. Harris, *Measurement of the motional sidebands of a nanogram-scale oscillator in the quantum regime*, Phys. Rev. A **92**, 061801(R) (2015).

[94] V. Sudhir, D. J. Wilson, R. Schilling, H. Schütz, S. A. Fedorov, A. H. Ghadimi, A. Nunnenkamp, and T. J. Kippenberg, *Appearance and Disappearance of Quantum Correlations in Measurement-Based Feedback Control of a Mechanical Oscillator*, Phys. Rev. X **7**, 011001 (2017).

[95] F. Y. Khalili, H. Miao, H. Yang, A. H. Safavi-Naeini, O. Painter, and Y. Chen, *Quantum back-action in measurements of zero-point mechanical oscillations*, Phys. Rev. A **86**, 033840 (2012).

[96] F. Tebbenjohanns, M. Frimmer, and L. Novotny, *Optimal position detection of a dipolar scatterer in a focused field*, Phys. Rev. A **100**, 043821 (2019).

[97] A. M. Jayich, J. C. Sankey, K. Børkje, D. Lee, C. Yang, M. Underwood, L. Childress, A. Petrenko, S. M. Girvin, and J. G. E. Harris, *Cryogenic optomechanics with a Si3N4membrane and classical laser noise*, New J. Phys.

**14**, 115018 (2012).

[98] M. R. Vanner, I. Pikovski, G. D. Cole, M. S. Kim, Č. Brukner, K. Hammerer, G. J. Milburn, and M. Aspelmeyer, *Pulsed quantum optomechanics*, Proc. Natl. Acad. Sci. U.S.A. **108**, 16182 (2011).

[99] M. Aspelmeyer, T. J. Kippenberg, and F. Marquardt, *Cavity Optomechanics: Nano- and Micromechanical Resonators Interacting with Light*, Quantum Science and Technology (Springer-Verlag, Berlin Heidelberg, 2014).

[100] C. W. Gardiner and M. J. Collett, *Input and output in damped quantum systems: Quantum stochastic differential equations and the master equation*, Phys. Rev. A **31**, 3761 (1985).

[101] R. J. Glauber, *The Quantum Theory of Optical Coherence*, Phys. Rev. **130**, 2529 (1963).

[102] K. Børkje, *Heterodyne photodetection measurements on cavity optomechanical systems: Interpretation of sideband asymmetry and limits to a classical explanation*, Phys. Rev. A **94**, 043816 (2016).

[103] P. L. Kelley and W. H. Kleiner, *Theory of Electromagnetic Field Measurement and Photoelectron Counting*, Phys. Rev. **136**, A316 (1964).

[104] H. J. Carmichael, *Spectrum of squeezing and photocurrent shot noise: a normally ordered treatment*, J. Opt. Soc. Am. B **4**, 1588 (1987).

[105] L. Mandel and E. Wolf, *Optical Coherence and Quantum Optics* (Cambridge University, Cambridge, England, 1995).

[106] G. J. Milburn and S. Basiri-Esfahani, *Quantum optics with one or two photons*, Proc. R. Soc. A. **471**, 20150208 (2015).

[107] A. B. Shkarin, A. D. Kashkanova, C. D. Brown, S. Garcia, K. Ott, J. Reichel, and J. G. E. Harris, *Quantum Optomechanics in a Liquid*, Phys. Rev. Lett. **122**, 153601 (2019).

[108] J. D. P. Machado and Y. M. Blanter, *Absence of quantum features in sideband asymmetry*, arXiv:1805.02952 .

[109] T. R. Hart, R. L. Aggarwal, and B. Lax, *Temperature Dependence of Raman Scattering in Silicon*, Phys. Rev. B **1**, 638 (1970).

[110] T. Shiota and F. Wada, *Distributed temperature sensors for single-mode fibers*, Proc. SPIE **1586** (1992), 10.1117/12.56503.

[111] N. Brahms, T. Botter, S. Schreppler, D. W. C. Brooks, and D. M. Stamper-Kurn, *Optical Detection of the Quantization of Collective Atomic Motion*, Phys. Rev. Lett. **108**, 133601 (2012).

[112] E. Schrödinger, *Die gegenwärtige Situation in der Quantenmechanik*, Naturwissenschaften **23**, 807 (1935).

[113] O. Romero-Isart, M. L. Juan, R. Quidant, and J. I. Cirac, *Toward quantum*

*superposition of living organisms*, New J. Phys. **12**, 033015 (2010).

[114] R. Kaltenbaek, G. Hechenblaikner, N. Kiesel, O. Romero-Isart, K. C. Schwab, U. Johann, and M. Aspelmeyer, *Macroscopic quantum resonators (MAQRO): Testing quantum and gravitational physics with massive mechanical resonators*, Exp. Astron. **34**, 123 (2012).

[115] M. Arndt, O. Nairz, J. Vos-Andreae, C. Keller, G. van der Zouw, and A. Zeilinger, *Wave-particle duality of C-60 molecules*, Nature (London) **401**, 680 (1999).

[116] E. Hebestreit, M. Frimmer, R. Reimann, and L. Novotny, *Sensing Static Forces with Free-Falling Nanoparticles*, Phys. Rev. Lett. **121**, 063602 (2018).

[117] T. Delord, L. Nicolas, L. Schwab, and G. Hétet, *Electron spin resonance from NV centers in diamonds levitating in an ion trap*, New J. Phys. **19**, 033031 (2017).

[118] G. P. Conangla, A. W. Schell, R. A. Rica, and R. Quidant, *Motion Control and Optical Interrogation of a Levitating Single Nitrogen Vacancy in Vacuum*, Nano Lett. **18**, 3956 (2018).

[119] D. S. Bykov, P. Mestres, L. Dania, L. Schmöger, and T. E. Northup, *Direct loading of nanoparticles under high vacuum into a Paul trap for levitodynamical experiments*, Appl. Phys. Lett. **115**, 034101 (2019).

[120] T. Delord, P. Huillery, L. Nicolas, and G. Hétet, *Spin-cooling of the motion of a trapped diamond*, Nature (London) **580**, 56 (2020).

[121] M. G. A. Paris, F. Illuminati, A. Serafini, and S. De Siena, *Purity of Gaussian states: Measurement schemes and time evolution in noisy channels*, Phys. Rev. A **68**, 012314 (2003).

[122] F. Tebbenjohanns, M. Frimmer, V. Jain, D. Windey, and L. Novotny, *Motional Sideband Asymmetry of a Nanoparticle Optically Levitated in Free Space*, Phys. Rev. Lett. **124**, 013603 (2020).

[123] H. M. Wiseman and G. J. Milburn, *Quantum theory of optical feedback via homodyne detection*, Phys. Rev. Lett. **70**, 548 (1993).

[124] A. C. Doherty and K. Jacobs, *Feedback control of quantum systems using continuous state estimation*, Phys. Rev. A **60**, 2700 (1999).

[125] A. C. Doherty, S. Habib, K. Jacobs, H. Mabuchi, and S. M. Tan, *Quantum feedback control and classical control theory*, Phys. Rev. A **62**, 012105 (2000).

[126] A. C. Doherty, A. Szorkovszky, G. I. Harris, and W. P. Bowen, *The quantum trajectory approach to quantum feedback control of an oscillator revisited*, Philos. Trans. R. Soc. A **370**, 5338 (2012).

[127] F. M. Gardner, *Phaselock Techniques*, 3rd ed. (Wiley, Hoboken, 2005).

[128] F. Tebbenjohanns, *Shot Noise Limited High Power Photodetector*, Semester

Project Report (Photonics Laboratory, ETH Zürich, 2016).

[129] N. Redmon, *Biquad calculator v2*, online; accessed 1 Sept. 2018.

[130] T. Storey and R. Nelson, *IIR Filter Design in VHDL Targeted for 18-Bit, 48 KHz Audio Signal Use*, online; accessed 1 Sept. 2018.

[131] F. M. Ciurana, G. Colangelo, R. J. Sewell, and M. W. Mitchell, *Real-time shot-noise-limited differential photodetection for atomic quantum control*, Opt. Lett. **41**, 2946 (2016).

# Acknowledgments

*Science is more than ever a teamsport*, John Mather told the ICFO news after his talk in 2016 which I attended during my Master project. Lukas read the news article, marked this line, and pinned it to our wall in the conference room where it has been throughout my whole PhD. Thank you Lukas for making this your mantra and for creating and fostering an amazing team.
Thank you Martin for a countless number of discussions in the lab, on the balcony, in the Alps and the Pyrenees, on bikes, buses, and cars. These discussions were the main source of ideas for my work and I am missing them dearly since Corona banned them to Zoom. I am grateful to Barbara for making the lab feel like home. To Vijay who explained optical levitation to me before anyone! To René for countless tips and tricks both in the laboratory and outside of it. To Dominik for being the best IT support ever. To Andrei for invaluable scientific input. To Ronja (tea) and Alfonso (coffee)! And especially to Klaus for incredible alpine experiences, pre-work skitours, and life pro tips. And to all the other nano-opticians for simply being great colleagues.
Outside the ETH, I am extremely lucky to have such great friends: Thank you David and Beat for being the best flatmates I could imagine. Thank you Johannes, Fabian, Andi, Sara, Nadine, Julia, Caro, Jakob, Franzi, David V., Paul, Fredi, and Vincent for a lot of beverages and good food, for trips, skiing, hiking, walks, games and a fantastic time without lasers and particles!
Finally, my PhD would have been impossible without my family and I even have two: Henry, Myriam, Hala, Ben in Zurich and of course Pauline, Emilia, Laurenz, Mami und Papi in Heinde! Ich bin euch allen sehr sehr dankbar.

# Publications

**This thesis is based in part on the following publications:**

**F. Tebbenjohanns**, M. Frimmer, A. Militaru, V. Jain, and L. Novotny, *Cold Damping of an Optically Levitated Nanoparticle to Microkelvin Temperatures*, Phys. Rev. Lett. **122**, 223601 (2019).

**F. Tebbenjohanns**, M. Frimmer, and L. Novotny, *Optimal position detection of a dipolar scatterer in a focused field*, Phys. Rev. A **100**, 043821 (2019).

**F. Tebbenjohanns**, M. Frimmer, V. Jain, D. Windey, and L. Novotny, *Motional Sideband Asymmetry of a Nanoparticle Optically Levitated in Free Space*, Phys. Rev. Lett. **124**, 013603 (2020).

**Other publications by the author:**

V. Jain, **F. Tebbenjohanns**, and L. Novotny, *Microkelvin Control of an Optically Levitated Nanoparticle*, Frontiers in Optics 2016, OSA, FF5B.2 (2016).

R. Reimann, M. Doderer, E. Hebestreit, R. Diehl, M. Frimmer, D. Windey, **F. Tebbenjohanns**, and L. Novotny, *GHz Rotation of an Optically Trapped Nanoparticle in Vacuum*, Phys. Rev. Lett. **121**, 033602 (2018).

R. Diehl, E. Hebestreit, R. Reimann, **F. Tebbenjohanns**, M. Frimmer, L. Novotny, *Optical levitation and feedback cooling of a nanoparticle at subwavelength distances from a membrane*, Phys. Rev. A **98**, 013851 (2018).

J. Liao , M. Jost, M. Schaffner, M. Magno, M. Korb, L. Benini, **F. Tebbenjohanns**, R. Reimann, V. Jain, M. Gross, A. Militaru, M. Frimmer, and L. Novotny, *FPGA Implementation of a Kalman-Based Motion Estimator for Levitated Nanoparticles*, IEEE Transactions on Instrumentation and Measurement **68**, 2374 (2019).

R. Sibilo, J. M. Pérez, **F. Tebbenjohanns**, C. Hurth, and V. Pruneri, *Surface cytometer for fluorescent detection and growth monitoring of bacteria over a large field-of-view* Biomed. Opt. Express **10**, 2101 (2019).

M. Frimmer, T. L. Heugel, Ž. Nosan, **F. Tebbenjohanns**, D. Hälg, A. Akin, C. L. Degen, L. Novotny, R. Chitra, O. Zilberberg, and A. Eichler, *Rapid Flipping of Parametric Phase States* Phys. Rev. Lett. **123**, 254102 (2019).

F. v. d. Laan, R. Reimann, A. Militaru, **F. Tebbenjohanns**, D. Windey, M. Frimmer, and L. Novotny, *Optically levitated rotor at its thermal limit of frequency stability*, Phys. Rev.A **102**, 013505 (2020).

# Curriculum Vitae

Felix Tebbenjohanns was born in Bonn, Germany in 1991. He graduated from ETH Zürich with a Master of Science in electrical engineering and information technology in 2016 with a stay abroad at Imperial College London and an internship in the software group of Sensirion AG in Stäfa, Switzerland. During his undergraduate studies at ETH, he was a teaching assistant for digital electronics, analog electronics, and complex analysis. He carried out his Master's thesis on fluorescence cytometry in the group of Valerio Pruneri at ICFO, Barcelona. In the same group, he developed an efficient method to process random bits in an FPGA-based Monte Carlo simulation, which led to a patent submission. In 2017, he started his research on levitated optomechanics in Lukas Novotny's group in Zürich.